TECHNISCHE UNIVERSITÄT WIEN

Development and characterisation of Ti-MMCs with high specific stiffness

DIPLOMA THESIS

Conducted for the attainment of the academic degree of a

Diplom-Ingenieur (Dipl.-Ing.)

supervised by

Ao.Univ.Prof. Dipl.-Ing. Dr.techn.
Christian Edtmaier

submitted at the

TU Wien
Faculty of Technical Chemistry
Institute of Chemical Technologies and Analytics

by

Nico Moser
Matriculation number 11704918

Vienna, 2023

Abstract

Titanium alloys are becoming increasingly popular for aerospace structural components, as they offer high specific strength and good corrosion resistance, yet are lightweight. Weight reduction is also driving the development of other alloys to replace other components currently made from aluminium, iron or nickel alloys. To replace these parts, certain mechanical properties such as stiffness, strength or creep behaviour need to be improved. There is also a desire to develop new applications for additive manufacturing using titanium alloys. In particular, wire-arc additive manufacturing has proven to be a good method for 3D printing Ti and Ti-6Al-4V.

This work focuses on the development and characterisation of titanium alloys and titanium metal matrix composites with increased specific Young's modulus using powder hot extrusion. Suitable titanium alloys and pure titanium with and without particle reinforcement are produced. The particle reinforcement is focused on titanium carbide and boron carbide. To obtain a uniform material, the extruded rods are heat-treated at 1000 °C for 90 hours. Both the extruded and heat-treated rods are then characterised in terms of microstructure using optical, scanning electron microscopy and energy dispersive spectroscopy. X-ray diffraction is used to determine the phases. The mechanical properties are determined by Vickers hardness measurements and ultrasound stiffness measurements.

Powder hot extrusion is suitable for the production of dense titanium metal matrix composites (MMCs). The stiffness measurements show that it is possible to increase the specific Young's modulus beyond 30 $\mathrm{GPa/(g\,cm^{-3})}$. Systems reinforced with 3 vol% boron carbide show an increase in specific stiffness of up to 34.6 $\mathrm{GPa/(g\,cm^{-3})}$ after heat treatment. This is explained by the in-situ formation of titanium borides. High stiffness is also obtained when Ti-8Al-1Mo-1V and Ti-4Al-3Cu-2Fe are reinforced with 3 vol% titanium carbide. Remarkably, the Ti-8Al-1Mo-1V matrix shows improved properties after heat treatment with a specific stiffness of 30.7 $\mathrm{GPa/(g\,cm^{-3})}$, making the alloy interesting for subsequent wire manufacturing. The mechanism behind this is suggested to be the formation of the ordered Ti_3Al phase due to the heat treatment.

In order to be commercially viable, the materials require further investigation into strength, ductility and anisotropy. Another challenge is the ability to form the rods into wire, where ductility is an important consideration.

Deutsche Kurzfassung

Titanlegierungen spielen in der Luft- und Raumfahrt eine wichtige Rolle. Sie bieten eine hohe spezifische Festigkeit und eine gute Korrosionsbeständigkeit bei geringem Gewicht. Die Gewichtseinsparung ist auch die treibende Kraft für die Entwicklung weiterer Legierungen, um andere Bauteile zu ersetzen, die derzeit aus Aluminium-, Eisen- oder Nickellegierungen bestehen. Dafür müssen bestimmte mechanische Eigenschaften wie Steifigkeit, Festigkeit oder Kriechverhalten verbessert werden. Darüber hinaus gibt es Bestrebungen, der additiven Fertigung mit Titanlegierungen neue Anwendungsfelder zu erschließen. Insbesondere hat sich die additive Fertigung mittels Lichtbogen als gute Methode für den 3D-Druck von Ti und Ti-6Al-4V erwiesen.

Der Schwerpunkt dieser Arbeit liegt auf der Entwicklung und Charakterisierung von stranggepressten Titanlegierungen und Titan-Metallmatrix-Verbundwerkstoffen (TMC's) mit hohem spezifischem E-Modul. Dazu werden geeignete Titanlegierungen und Reintitan mit und ohne Partikelverstärkung hergestellt. Die Partikelverstärkung konzentriert sich auf Titankarbid und Borkarbid. Um ein homogenes Material zu erhalten, werden die stranggepressten Stränge 90 Stunden bei 1000 °C wärmebehandelt. Sowohl die stranggepressten als auch die wärmebehandelten Stränge werden anschließend mittels Licht- und Rasterelektronenmikroskopie sowie energiedispersiver Spektroskopie hinsichtlich ihrer Mikrostruktur charakterisiert. Zur Phasenbestimmung wird die Röntgendiffraktometrie eingesetzt. Hinsichtlich der mechanischen Eigenschaften werden Vickers-Härtemessungen und Steifigkeitsmessungen mittels Ultraschall durchgeführt.

Das Pulverstrangpressen ist für die Herstellung von dichten TMC's geeignet. Steifigkeitsmessungen zeigen, dass eine Erhöhung des spezifischen Elastizitätsmoduls über $30\,\mathrm{GPa/(g\,cm^{-3})}$ hinaus möglich ist. Mit 3 vol% Borkarbid verstärkte Systeme zeigen nach der Wärmebehandlung eine erhöhte spezifische Steifigkeit von bis zu $34.6\,\mathrm{GPa/(g\,cm^{-3})}$. Dies wird durch die in-situ-Bildung von Titanboriden erklärt. Dies ist bei Matrixsystemen aus Titan, Ti-6Al-4V und Ti-6.5Cu der Fall. Eine hohe Steifigkeit wird auch erreicht, wenn Ti-8Al-1Mo-1V und Ti-4Al-3Cu-2Fe mit 3 vol% Titankarbid verstärkt werden. Bemerkenswert ist, dass die Ti-8Al-1Mo-1V-Matrix nach der Wärmebehandlung verbesserte Eigenschaften mit einer Steigerung der spezifischen Steifigkeit auf $30.7\,\mathrm{GPa/(g\,cm^{-3})}$ zeigt, was diese Legierung für die Drahtherstellung interessant macht. Als Mechanismus wird die Bildung der geordneten Ti_3Al-Phase infolge der Wärmebehandlung vermutet.

Um für den kommerziellen Einsatz geeignet zu sein, müssen die Werkstoffe hinsichtlich Festigkeit, Duktilität und Anisotropie weiter untersucht werden. Eine weitere Herausforderung ist die Verarbeitbarkeit der hergestellten Stränge zu Drähten, wobei insbesondere die Duktilität eine wichtige Rolle spielt.

Contents

1 Introduction

Since commercial production by the DuPont Company in 1942, titanium and its alloys have established themselves as an irreplaceable material for specialised industries such as aerospace, chemical processing, marine and sports [1]. Its main advantages are high specific strength and good corrosion resistance. Another area of application is in medicine as artificial joints. Here the replacement material should have approximately the same Young's modulus as the supporting material (bone). This should prevent osteoporosis and poor integration with the bone. The route for biomedical applications is therefore based on beta-Ti alloys [2]. On the other hand, for applications in the space sector, it is exactly the other way round. The aim is to reach a new level of high-speed aircraft, which requires a high degree of stiffness in an elevated temperature regime. Currently, these parts, the airframe structures, are made of aluminium alloys and polymer composites [3]. However, both the production and the processing of titanium are relatively expensive, which limits the profitable processing to near net shape methods [1]. This leads to a great interest in alternative manufacturing methods that offer more flexibility. Especially in aerospace, additive manufacturing (AM) has become a great asset. It combines the flexibility of 3D printing, near-net-shape structures and a minimisation of scrap rates. With a scrap rate of $< 10\,\%$, it clearly outperforms conventional machining processes with scrap rates of up to $90\,\%$ [4]. There are established AM methods that differ in terms of energy input (laser, electron beam, plasma arc) or material feed (wire, powder) and have their strengths and weaknesses [5].

The focus of this work is to find precursor materials that can later be used for wire-arc additive manufacturing (WAAM). Powder hot extrusion will be used to produce the rods, which, due to the relatively low temperatures and short reaction times, offers new possibilities for alloying and particle improvement. The ultimate goal of this work is to produce a material that can be used as a candidate for additive manufacturing filaments. The designed material should combine the following properties:

- specific stiffness $> 30\,\mathrm{GPa/(g\,cm^{-3})}$
- fracture strain $> 5\ \%$
- specific strength $>$ specific strength of Ti-6Al-4V
- index of anistropy $= 1$

In order to obtain the desired properties, alloying, particle enhancement and heat treatment are used. The so produced rods are then characterised in regard of their microstructure and phase composition as well as their mechanical properties, namely stiffness, hardness and strength.

2 Theoretical Background

2.1 Titanium and Titanium Metal Matrix Composites

Classified as the heaviest of the light metals titanium occupies a special place in the periodic table. Its low density of $4.51\,\mathrm{g/cm^3}$ compared to structural materials such as nickel or iron makes it very attractive for transport applications [1]. In the aerospace sector in particular, weight reduction is so crucial that a tolerance of higher costs of up to 10000 € per kilogram of weight saved is still economically justifiable. In addition to weight reduction, titanium alloys have excellent corrosion resistance and high specific strength [6]. Titanium has two allotropic modifications. One is the hexagonal closed packed α-phase, which is stable up to 882 °C. Above this temperature the body centred closed packed β-phase is stable. Depending on the phases present, different properties (strength, ductility, weldability) are possible. The β-transus temperature can be modified by alloying. So-called α-stabilisers, such as aluminium, oxygen, nitrogen or carbon, increase the β-transus temperature. On the other hand, β-stabilisers, such as molybdenum, vanadium, iron or copper, lower the β-transus temperature. A schematic overview of how the alloying elements affect the phase diagram of titanium alloys can be seen in Figure 1. The β-stabilisers can again be divided into two groups, isomorphic and eutectoid, depending on the solubility of the alloying element.

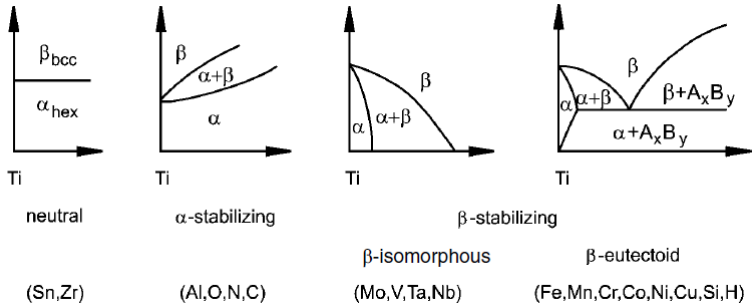

Figure 1: Influence of different alloying elements on the titanium phase diagram [1].

Alloying can be used to achieve a specific microstructure, resulting in three general types of titanium alloys, namely α, $\alpha+\beta$ and β alloys. Pure titanium or titanium-aluminium alloys consist of a single phase α microstructure. The main advantages of α titanium alloys are their low density and excellent corrosion and oxidation resistance. The β titanium alloys have significantly higher strength but lower ductility. The $\alpha+\beta$ titanium alloys combine the properties of both phases. In addition, all mechanical properties depend on grain morphology. Comparing the mechanical properties of different types of titanium alloys, as shown in Table 1, it can be seen that α alloys have less favourable properties in terms of hardness and strength than $\alpha+\beta$ and β alloys. Thus, in aerospace $\alpha+\beta$ and β alloys are mainly used as structural

materials, whereas α alloys are used in the chemical and process industries [1]. However, the scope for improving stiffness by alloying alone is limited.

Table 1: Comparision of mechanical properties of α, $\alpha + \beta$ and β alloys [1]

Composition (w%)	Hardness (HV)	E (GPa)	Tensile Strength (MPa)	ϵ (%)
α titanium alloys				
cp-Ti Grade 4 (0.2Fe-0.4O)	260	100-120	550	15
$\alpha + \beta$ titanium alloys				
Ti-6Al-4V	300-400	110-140	900-1200	13-16
β titanium alloys				
Ti-15V-3Cr-3Al-3Sn	300-450	80-100	800-1100	10-20

Another approach is particle reinforcement. By adding hard and stiff particles, a composite is created. When working with titanium, this is known as titanium metal matrix composites (Ti-MMC). In this system, the softer metal matrix is intended to provide ductility, while the reinforcement phase increases strength and stiffness. The reinforcing phase can vary in morphology. There are particles, short fibres and continuous fibres. If an isotropic material is required, particles are usually the most appropriate choice. These particles are generally of a ceramic or non-metallic nature, for example TiC, TiN, TiB or SiC [7]. One way to estimate a certain mechanical property of a MMC is the Rule of Mixture (ROM). Taking in account the equal strain treatment (Voigt model) and the equal stress treatment (Reuss model) the ROM leads to the following expression for the upper limit Equations 2.1 and lower limit 2.2 of the Young's modulus [8].

$$E_C = (1 - f_p) \cdot E_m + f_p \cdot E_p \tag{2.1}$$

$$\frac{1}{E_C} = \frac{1 - f_p}{E_m} + \frac{f_p}{E_p} \tag{2.2}$$

E_C... Young's modulus of the composite in GPa
E_m... Young's modulus of the matrix in GPa
E_p... Young's modulus of the particle in GPa
f_p... Particle volume fraction

Figure 2 shows the ROM applied to a Ti/TiC and Ti/TiB system. The Ti-matrix is assumed to have an elastic modulus of 100 GPa. The particles have an Young's modulus of 460 GPa for TiC and 550 GPa for TiB [7].

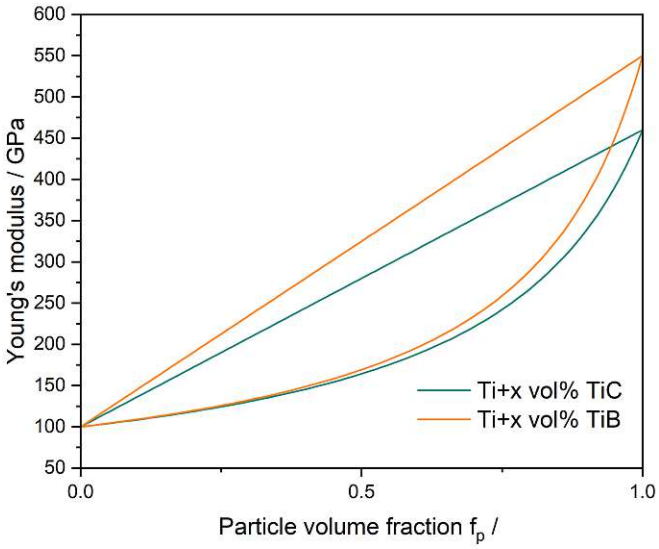

Figure 2: Rule of mixture calculations for Ti/TiC and Ti/TiB systems, showing the upper and lower stiffness limit at a given particle reinforcement

2.2 Mechanical Properties

2.2.1 Young's modulus

The Young's modulus (E) links the relation of stress (σ) and strain (ε). In an ideal isotropic material the Young's modulus is a scalar and can be described by Hooke's Law:

$$\sigma = E \cdot \varepsilon \tag{2.3}$$

Unlike other materials parameters the Young's modulus is purely defined by the characteristics of the material itself. It is directly connected to the bond energy. Thus, there are only two options to optimise the stiffness of a material, namely improvement through or creating a composite, with phases that have an higher intrinsic Young's modulus [9]. On an atomistic scale two forces dominate the potential (U_{bond}), attractive and repulsive ones. Both are a function of the distance (r) and can be described via exponential functions. Combined, the derived potential can be expressed as follows and is referred to as the Lennard-Jones potential (Figure 3) [10]:

$$U_{bond}(r) = \frac{B}{r^m} - \frac{A}{r^n} \tag{2.4}$$

The second derivative of the Lennard-Jones potential is directly connected to the Young's modulus. By doing a Taylor expansion around the equilibrium position r_0 the following term is obtained:

$$E = \frac{1}{r_0} \cdot \frac{\partial^2 U}{\partial r^2} \tag{2.5}$$

Thus, the Young's modulus is directly connected with the bonding energy of a material and determined by the shape of the potential well.

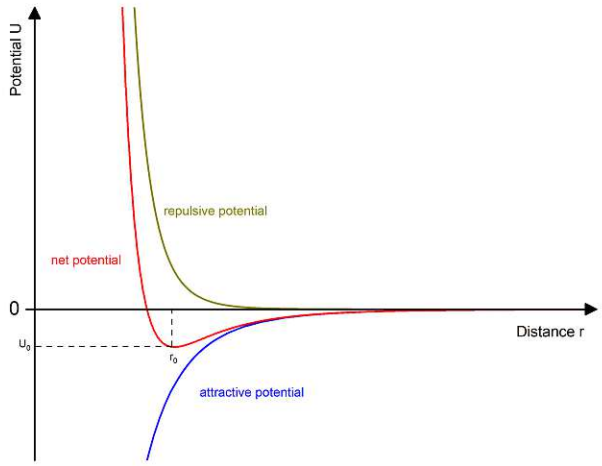

Figure 3: Lennard-Jones Potential

2.2.2 Mechanisms of strength improvement

In general, strength is defined as the maximum stress capacity of a material before it breaks or is plastically deformed [11]. In contrast, to the Young's modulus the strength of a material can be modified through its history. The only way to increase the strength is by blocking the dislocation movement. Possible obstacles are provided through the following strength improvement mechanisms:

- Work hardening
- Solid solution hardening
- Grain refinement
- Particle reinforcement

Work hardening takes place when a material is deformed plastically. Initially, dislocations wander along the most favourable slip planes. The movement leads to internal stresses that block further movement of the dislocations [12]. This leads to an increase in the dislocation density ρ, which is related to the strength increase ΔR by the following term [13]:

$$\Delta R \propto \sqrt{\rho} \tag{2.6}$$

Alloying leads to solid solution hardening. By integrating atoms either into the lattice or in interstitial spaces, they exhibit stresses into their surroundings. Interstitial and larger solute atoms lead to compressive stresses, while smaller solute atoms lead to tensile stresses. The stress fields are generated by parelastic interaction, depending on the alloyed atom size. Another part is the dielastic interaction given by the different shear moduli of the solute and matrix atoms. In addition, there is also a chemical interaction, taking the charging state into account. The summary of all the interactions is described by the Friedel relation, which describes how much the critical shear stress $\Delta\tau_c$ must be increased to overcome the effect of solid solution hardening. The equation includes the Peierls stress τ_0, the shear modulus G, the foreign atom concentration c and a constant, which comes from the lattice parameters and the type of dislocation [14]:

$$\Delta\tau_c \propto \tau_0 \cdot const. \cdot G \cdot \sqrt{c} \tag{2.7}$$

In a polycrystalline material grain boundaries separate neighbouring crystallites. As mentioned before dislocation move along slip planes. Inside one crystallite the orientation is well defined. However, if a dislocation reaches the grain boundary of a neighbouring crystallite the orientation will in most cases be different. Depending on the angle of the orientation the dislocation needs more shear strength, the higher the angle the more shear strength is needed. In a logic conclusion, finer crystallites lead to more grain boundaries, which lead to a higher strength. This phenomenon is described by the Hall-Patch relation. It gives the connection between the yield strength σ, the material specific grain boundary resistance k_y and the average grain size d [15]. Related to the normal stress the Hall-Patch relation is:

$$\sigma = \sigma_0 + \frac{k_y}{\sqrt{d}} \tag{2.8}$$

The presence of particles, be it precipitations or ex-situ added particles, provide a further barrier to the dislocation movement. The strength increase $\Delta\tau$, that adds up with the Peierls stress τ_0 is depended of the particle's volume fraction f_p as well as their size r_p. For small particles the cutting mechanism occurs, whereas with increasing size the Orowan mechanism becomes predominant [16].

$$\Delta\tau = \tau_o \cdot k + \frac{\sqrt{f_p}}{r_p} \tag{2.9}$$

2.3 Extrusion

Extrusion is defined as a massive forming process, where a heated billet is put into a recipient and pressed through a die using a punch. In the process the billet adapts the geometry of the die. There are two types of extruding mechanics - direct and indirect. For the direct extrusion the product is extruded in the same direction as the total extrusion force, whereas it is the opposite direction for the indirect method. Using the direct method results in a higher friction heat and only allows low extrusion velocities. Via extrusion it is possible to fabricate solid profiles as well as hollow profiles and many types of geometries. Extrusion is mainly used for the manufacturing of aluminium, copper and steel materials. For titanium, there are only limited applications so far because of the high reactivity with oxygen, while this is not the case for noble metals and aluminium [17]. Hence, when using titanium powders as starting material, the powder must be encapsulated. The extrusion then has two impacts on the billet. First, it ensures the compaction of the powder and second, the massive forming [18].

2.4 State of the art

In recent years many Ti-MMCs have been developed, most of them focusing on a pure titanium matrix with TiB, SiC and carbon nanotube reinforcements. Throughout the research many fabrication methods have been established. To name a few the most common methods are powder metallurgy (pressing and sintering), spark laser sintering, arc melting and laser melting deposition [19]. In general, the amount of reinforcement phase is kept relatively low to remain in a feasible ductility regime. Tsang et al. [20] showed that in the Ti/TiB systems an increasing amount of TiB leads to a higher stiffness but significantly reduced ductility. They fabricated composites with 0, 5, 10 and 15 vol% TiB via vacuum arc melting and tested them for mechanical properties. Comparing pure titanium and the composite with 15 vol% TiB they found an increase in the stiffness from 109 to 139 GPa at the cost of reduction in ductility from 20.7 to 0.4 % in elongation. However, for some applications, such as high temperature materials, ductility is negligible. Xinghong et al. [21] report the fabrication of Ti/TiB composites via self-propagating high temperature synthesis coupled with pseudo-hot isostatic pressing with TiB reinforcements up to 80 wt% TiB resulting in stiffness up to 391 GPa. Besides, titanium alloys also have been used for MMCs. Gorsse and Miracle [22] produced Ti-6Al-4V/TiB systems by powder metallurgy and reported a stiffness of 145 GPa for 20 wt% TiB but faced the problem of pronounced anisotropy due to the in-situ TiB whisker formation. Therefore, ex-situ reinforcements such as TiC are also worth considering as the fabrication is more controllable. Lagos et al. [23] produced Ti-6Al-4V/TiC composites via spark laser sintering. They report an increase of stiffness from 117 (0 wt% TiC) to 120 (5 wt% TiC) and 135 GPa (10 wt% TiC). The Ti/TiC has also been investigated by Zhang et al. [24]. They produced Ti/TiC composites by laser powder deposition with 0 to 40 vol% TiC. They found an hardness and strength increase with higher TiC addition paired with a loss in ductility. The mechanical properties of the before mentioned systems are shown in Table 2. Aerospace applications of Ti-MMCs are found in structural component of landing gears and experimentally in fan blades. In the automotive sector it can be used as connecting rods and engine valves. Another applications for Ti-MMCs are medical implants, sporting knives, screws and fasteners [19].

Table 2: List of studied Ti-MMCs showing mechanical properties and their fabrication method (LDM: laser deposition melting, VAR: vacuum arc remelting, SHS: self propagating high-temperature synthesis, PHIP: pseudo hot isostatic pressing, SPS: spark laser sintering, HIP: hot isostatic pressing).

Matrix	Reinforcement	Young's Modulus /GPa	UTS /MPa	Hardness	Elongation / %	Fabrication method	Source
Ti	-	-	585	260 HV5	19.0	LDM	[24]
Ti	10 vol% TiC	-	575	301 HV5	2.5	LDM	[24]
Ti	20 vol% TiC	-	590	336 HV5	1.5	LDM	[24]
Ti	40 vol% TiC	-	-	503 HV5	-	LDM	[24]
Ti	-	109	179	-	20.7	VAR	[20]
Ti	5 vol% TiB	121	787	-	12.5	VAR	[20]
Ti	10 vol% TiB	131	902	-	5.6	VAR	[20]
Ti	15 vol% TiB	139	903	-	0.4	VAR	[20]
Ti	40 wt% TiB	192	-	83 HRA	-	SHS/PHIP	[21]
Ti	50 wt% TiB	227	-	-	-	SHS/PHIP	[21]
Ti	60 wt% TiB	271	-	84 HRA	-	SHS/PHIP	[21]
Ti	70 wt% TiB	326	-	88 HRA	-	SHS/PHIP	[21]
Ti	80 wt% TiB	391	-	87 HRA	-	SHS/PHIP	[21]
Ti-6Al-4V	-	117	979	-	11.0	SPS	[23]
Ti-6Al-4V	5 vol% TiC	120	1076	-	3.0	SPS	[23]
Ti-6Al-4V	10 vol% TiC	135	1116	-	3.0	SPS	[23]
Ti-6Al-4V	20 wt% TiB	145	-	-	0.1	HIP	[24]

2.5 Aim of this work

The most studied titanium alloy in terms of additive manufacturing (AM) is Ti-6Al-4V. Various AM routes have been carried out and the as-built parts have been characterized in terms of their microstructure and mechanical properties [25]. One problem to address when using a heat source for the deposition (e.g. laser melting deposition) is the formation of columnar grains which lead to unfavourable anistropy [26]. One way to avoid this columnar growth is to be expected by using grain refiners for example chromium [27], iron [28] or cobalt [29]. Another approach for grain refining is to promote eutectoid decomposition by using elements like copper [30] and nickel [28]. Taking this into account and combining it with the goal of increasing the stiffness the systems in this work focus mainly around the the alloys and inter-metallics shown in Table 3. By adding ceramic particles to the given alloys MMC's are produced. In the frame on this work two particle reinforcements are used, namely titanium carbide TiC and boron carbide B_4C. While TiC will not react with the matrix a in-situ reaction of B_4C is to be expected. Thermodynamically two reactions can take place depending on the excess of titanium [31]:

$$5\,\mathrm{Ti} + \mathrm{B_4C} \longrightarrow 4\,\mathrm{TiB} + \mathrm{TiC}$$
$$3\,\mathrm{Ti} + \mathrm{B_4C} \longrightarrow 2\,\mathrm{TiB_2} + \mathrm{TiC}$$

As the reaction time during extrusion is quite short, no in-situ reaction of B_4C is expected. However, after the heat treatment the reinforcing particles should be TiC and TiB.

Table 3: Young's modulus of alloys, inter-metallics and ceramic particles in this work

	Young's modulus / GPa	Source
Ti	100-120	[1]
Ti-6Al-4V	110-140	[1]
Ti-8Al-1Mo-1V	120	[32]
Ti_2Ni	119	[33]
Ti_2Cu	138	[34]
TiFe	122	[35]
Ti_3Al	163	[36]
TiC	460	[7]
B_4C	460	[37]
TiB	550	[7]
TiB_2	529	[7]

3 Experimental and materials

3.1 Extrusion

Extrusion is based on a powder metallurgical approach. Therefore, powder mixtures were produced by blending the desired compositions in a polyethylene flask. In the manufacturing process there is a difference between just alloy systems and alloys with particle reinforcement. For systems consisting only of metallic components the flask including the powder was mixed together with 50 hardmetal grinding balls for 1 h in a Turbula mixer. After that the powder was separated from the grinding balls by using a sieve (mesh size 710 µm). Next, the powder was transferred into a steel cylinder (ST35, 40 mm outer diameter, 60 mm height, 36 mm inner diameter). For the particle reinforced systems the metallic powders were blended for 1 h, the reinforcing particles were added and mixed again for 1 h. After that the steel cylinders were sealed by welding a lid consisting of the same steel together. The so manufactured capsule and press die were sprayed with boron nitride to ensure lubrication in the extrusion process. The capsule was then put into a chamber furnace (depending on the material system 1000 −1100 °C) for 20 min. The pre-heated capsule was pressed using a compression ratio of 1:11.1 resulting in a rod of 12 mm. The extrusion speed was 10 mm/s. During the extrusion the recipient was held at 350 °C. In the end, a rod as shown in figure 4 is obtained. The used extrusion press (V. Jessernigg and Urban) is shown in Figure 5.

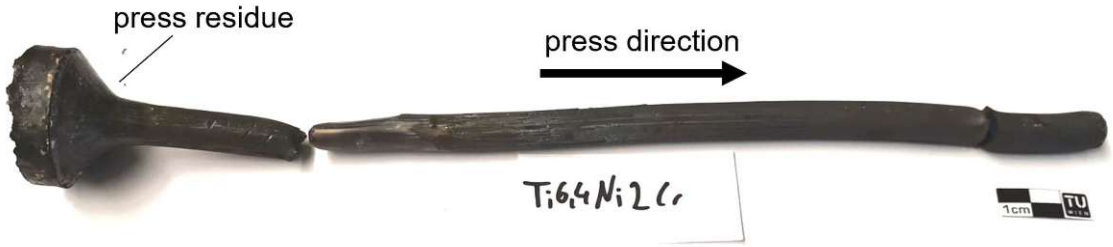

Figure 4: Rod after extrusion

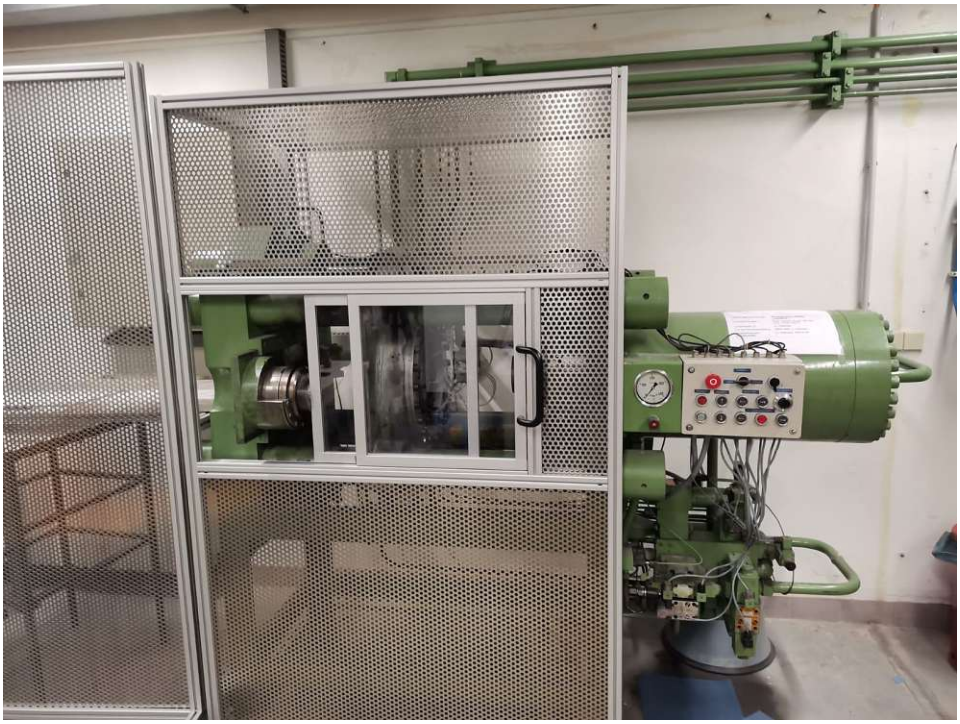

Figure 5: Extrusion press from V. Jessernigg and Urban

3.2 Powders

For the extrusion process pre-alloyed and elementary powders as well as ceramic particles were used. Table 4 shows the powders, their particle size and the manufacturer used for the extrusion experiments. In Figure 6 the SEM images of the powders are shown. The final powder compositions are shown in Table 5. The starting materials vary depending on the desired alloy composition. For the pure titanium systems, Ti-6.5Cu, Ti-4Al-3Cu-2Fe, Ti-6.4Ni-2Fe and Ti-6.4Ni-2Cr alloys elemental powders were used. The Ti-6Al-4V and Ti-5.7Al-5Co-3.8V alloys were based on pre-alloyed Ti-6Al-4V powder and Co powder respectively. For Ti-8Al-1Mo-1V a mixture of elemental Ti powder, pre-alloyed Ti-6Al-4V and Mo powder was used. The Ti-10Al-1.4N-0.8Cr alloy was prepared by mixing pre-alloyed Ti-34.5Al-4.8Nb-2.6Cr powder and Ti powder.

Table 4: Powders used for the extrusion

powder	particle size	manufacturer
Ti Gd 2	< 45 µm	Eckart TLS GmbH
Ti6Al4V	< 45 µm	TLS Technik GmbH & Co
Cu	2.5 - 3 µm	ECKA
Fe	< 100 µm	Höganäs AB
Cr	< 100 µm	?
Co	< 1 µm	Ceratizit
Mo	< 5 µm	Treibacher Industrie AG
Al	< 400 µm	MEPURA
Ni	2.5 - 4 µm	Vale Inco
B_4C	F500 (12.8 ± 1 µm)	3M^{TM}
TiC	< 45 µm	Alfa Products
Ti-34.5Al-4.8Nb-2.6Cr	< 45 µm	GfE

Table 5: Powder composition

	w% g/g											
	Ti	Al	V	Cu	Mo	Fe	Co	Ni	Cr	Nb	TiC	B_4C
Ti	1.000											
Ti+3vol% TiC	0,967										0.033	
Ti+3vol% B_4C F500	0.983											0.017
Ti+3vol% B_4C F2000	0.967											0.033
Ti+6vol% B_4C F500	0.966											0.034
Ti-6Al-4V	0.900	0.060	0.040									
Ti-6Al-4V+3vol% TiC	0.869	0.058	0.039								0.034	
Ti-6Al-4V+3vol%B_4C	0.885	0.059	0.039									0.009
Ti-6.5Cu	0.935			0.065								
Ti-6.5Cu+3vol% TiC	0.902			0.063							0.034	
Ti-6.5Cu+3vol% B_4C	0.920			0.064								0.016
Ti-8Al-1Mo-1V	0.899	0.081	0.010		0.010							
Ti-8Al-1Mo-1V+3vol%TiC	0.869	0.077	0.010		0.010						0.034	
Ti-8Al-1Mo-1V+3vol%B_4C	0.880	0.083	0.010		0.010							0.018
Ti-4Al-3Cu-2Fe	0.910	0.040		0.030		0.020						
Ti-4Al-3Cu-2Fe+3vol%TiC	0.879	0.039		0.029		0.019					0.034	
Ti-4Al-3Cu-2Fe+3vol%B_4C	0.878	0.039		0.029		0.019						0.034
Ti-5.7Al-5Co-3.8V	0.855	0.057	0.038				0.050					
Ti-5.7Al-5Co-3.8V+3vol%TiC	0.827	0.055	0.037				0.048				0.032	
Ti-5.7Al-5Co-3.8V+3vol%B_4C	0.841	0.056	0.037				0.049					0.017
Ti-6.4Ni-2Fe	0.916					0.020		0.064				
Ti-6.4Ni-2Fe presintered	0.916					0.020		0.064				
Ti-6.4Ni-2Fe+3vol%TiC	0.887					0.019		0.062			0.032	
Ti-6.4-Ni-2Fe+3vol%B_4C	0.901					0.020		0.063				0.016
Ti-6.4Ni-2Cr	0.916							0.064	0.020			
Ti-6.4-Ni-2Cr+3vol%TiC	0.887							0.062	0.019		0.032	
Ti-6.4Ni-2Cr+3vol%B_4C	0.901							0.063	0.020			0.016
Ti-10Al-1.4Nb-0.8Cr	0.874	0.104							0.008	0.014		

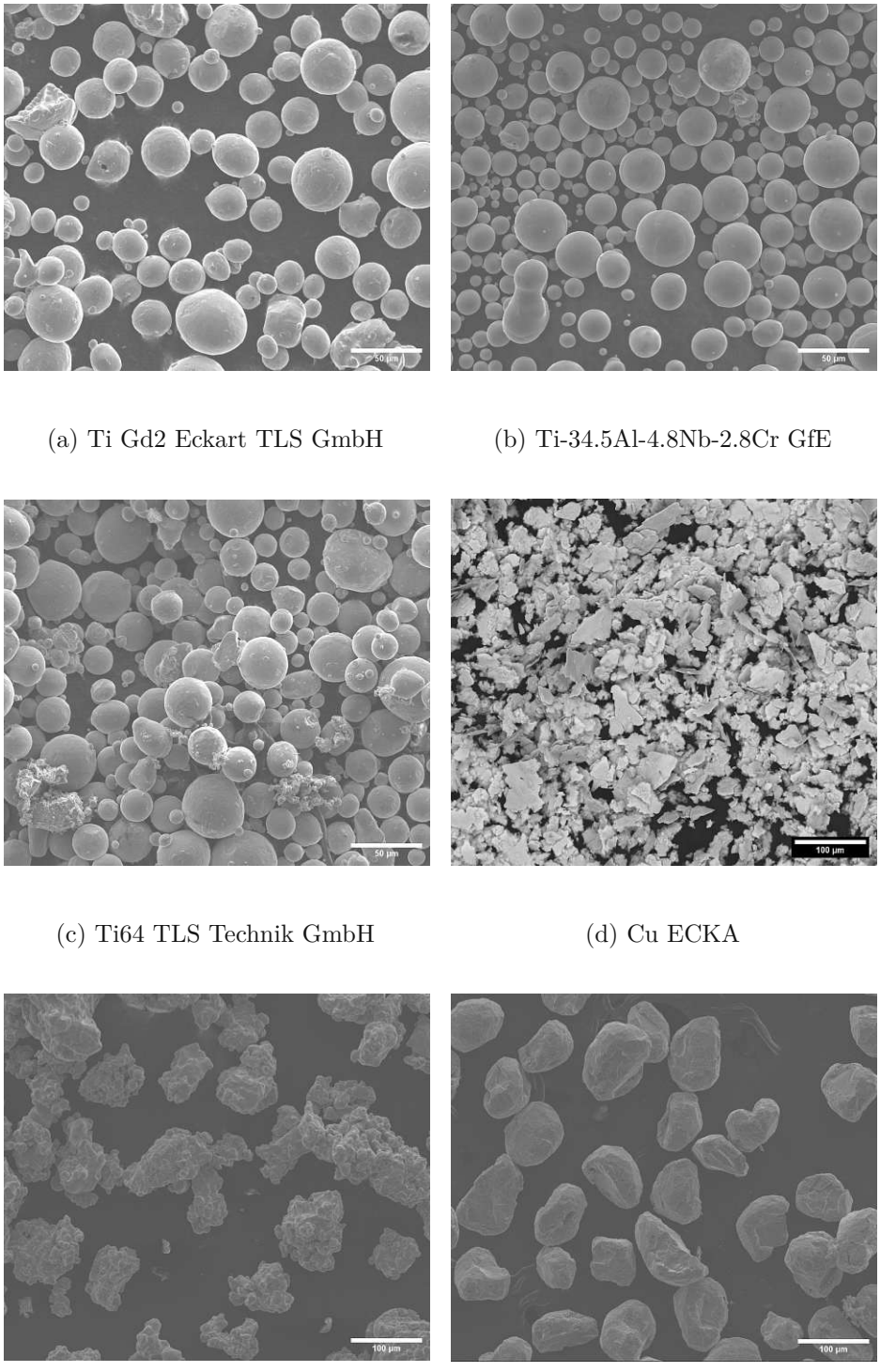

(a) Ti Gd2 Eckart TLS GmbH

(b) Ti-34.5Al-4.8Nb-2.8Cr GfE

(c) Ti64 TLS Technik GmbH

(d) Cu ECKA

(e) Fe Höganäs AB

(f) Cr manufacturer unknown

Figure 6: SEM images of the powders and ceramic particles used for the extrusion

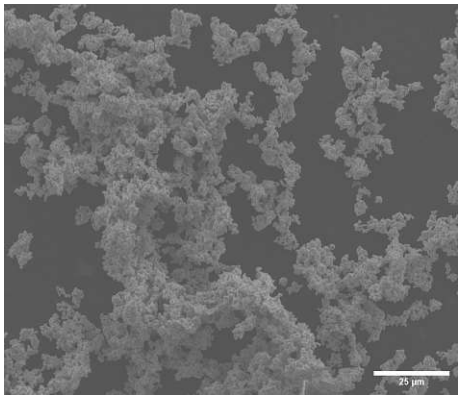

(g) Co Ceratizit

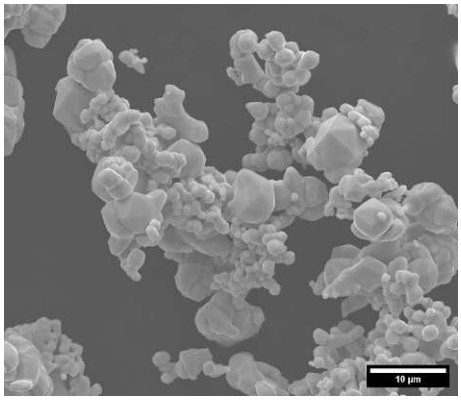

(h) Mo Treibacher Industrie AG

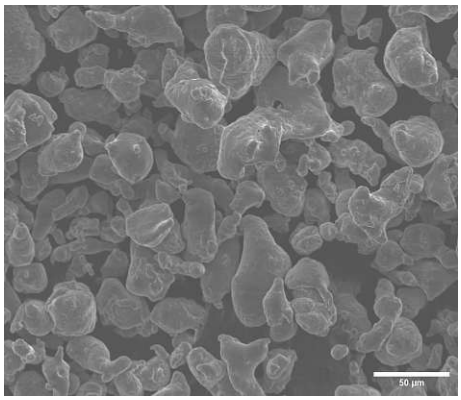

(i) Al MEPURA

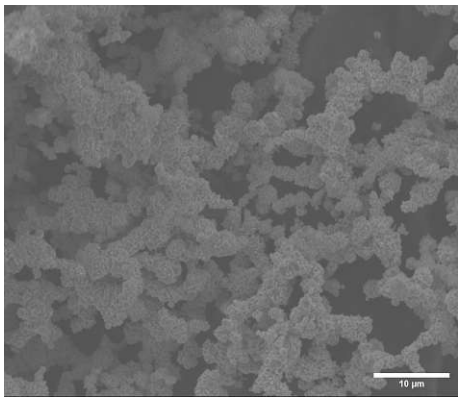

(j) Ni Vale Inco

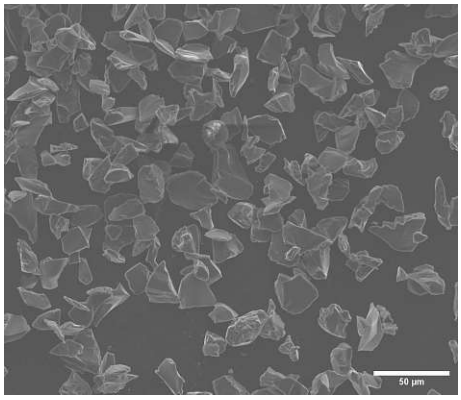

(k) B_4C 3M^{TM}

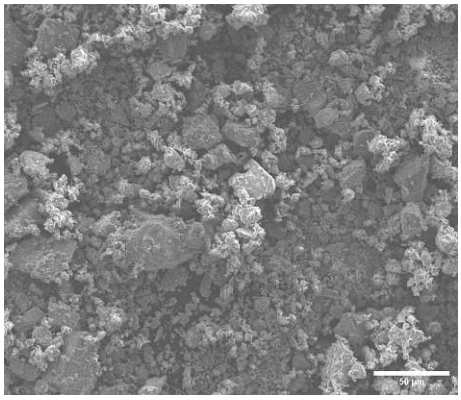

(l) TiC Alfa Products

Figure 6: SEM images of the powders and ceramic particles used for the extrusion (cont.)

3.3 Sample preparation

For the study of the microstructure the extruded rod was cut using a diamond cutting disk, so that two surfaces were obtained, one in the direction of pressing and one perpendicular to it (Figure 7). The annealed samples were only cut in the perpendicular direction. The cut samples were hot embedded using a MultiFast embedding reagent and a CitoPress-1. Next, the embedded samples were ground using an automatic grinding machine TegraPol-31 and SiC sandpaper. The grinding program included steps with sandpaper with the grain size of P500 (1:30 min), P1200 (2 min) and P4000 (3 min). After that, the samples were polished for 15 min with a MD/DP-Nap cloth. As polishing agent a mixture of 60 mL OPS NonDry (0.25 µm SiO_2 suspension, diluted 1:1 with water) and 20 mL H_2O_2 (33 %) was used. The polished samples were then viewed under the microscope before they were etched with hydrofluoric acid (1 %) for another microscopical analysis.

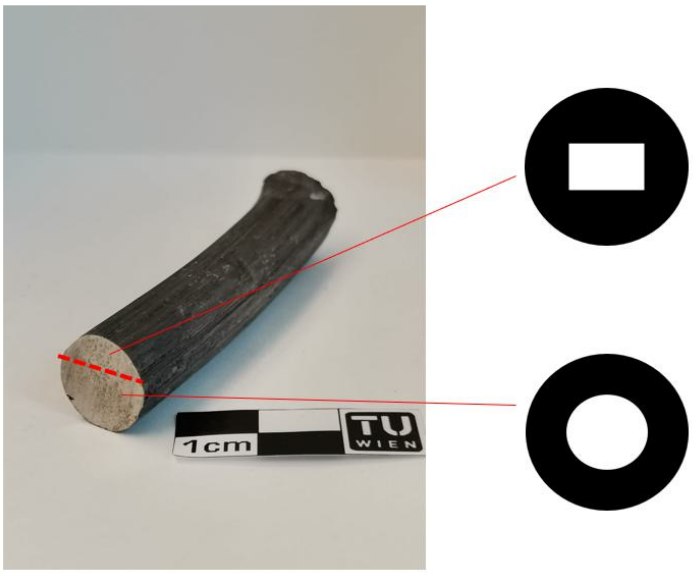

Figure 7: Pre-cut rod with schematics for subsequent embedding

3.4 Optical microscopy

Overview pictures of the etched samples were made with the Keyence VHX-5000. More detailed pictures of the unetched and etched were made with the Olympus GX51. In addition, it was used to measure the Vickers indents.

3.5 Scanning electron microscopy

For more detailed pictures the QUANTA 200 (FEI) was used. It was mainly used in backscatter mode to see the Z-contrast. For some powders secondary electron mode was used. Furthermore,

energy dispersive X-ray spectroscopy (EDS) was used to obtain compositions via point analysis and to conduct mappings. The samples were freed from the steel capsule, cut, stamped and ion-etched.

3.6 Transmission electron microscopy

To get information of the presence of Ti_3Al ordered structures in the Ti-Al systems Transmission Electron Microscopy (TEM) was caried out at the USTEM at TU Wien. The used TEM was the TECNAI F20 in dark field mode. In order to investigate ordered structures, electron diffraction was performed.

3.7 Hardness

For all extruded samples the hardness was measured in press direction and perpendicular to it. The heat treated samples were only measured in the perpendicular direction. For the hardness determination the Vickers method was used. Per sample five indents were generated using a weight of 10 kg and using the machine EMCO-Test M4U-025. The diagonals of the indents were then measured in the optical microscope. The Vickers hardness was calculated using Equation 3.1.

$$\begin{aligned} HV &= 0.1891 \cdot \frac{F}{d^2} \\ d &= \frac{d_1 + d_2}{2} \end{aligned} \tag{3.1}$$

HV... Vickers Hardness
F... Indentation force in N
d... Average of diagonal lengths in mm
d_x... Length of diagonal in mm

3.8 Estimation of strength

The tensile strength was approximated from the hardness values in accordance with the norm ISO 18265:2013, as the technical possibilities for producing tensile specimens were not available [38]. As the norm mainly focuses on steel, two additional datasets were taken into account. Namely, the technical report specifically on titanium alloys and a conversion table from Schütz+Licht Prütechnik GmbH [39, 40]. The measured hardness was fit into the conversion table from Schütz+Licht Prütechnik GmbH (Table 12). As the table only provides discontinuous values, a given experimental hardness was rounded to the next available data point. For example a measured value of 307 HV10 was rounded to the next available hardness in the table 310 HV10 which results in a strength of 995 MPa. The so obtained strengths were then cross-checked with an empirical equation coming from the before mentioned technical report:

$$UTS = 395 \cdot x\ HV + 14000 \tag{3.2}$$

UTS... Ultimate tensile strength in psi
HV... Vickers Hardness

3.9 Density measurements

The extruded samples (d = 12 mm) were turned off to 10 mm on a lathe to get rid of the steel casing. These rods were then cut into three cylinders of 5-10 mm height for each sample. The process was similar for the heat-treated samples, which were turned off from 12 to 10 mm before the heat treatment and from 10 to 8 mm after the heat treatment. The density was determined by using Archimedes' principle. Therefore, the cylinders were weighed in air and in water leading to a density according to Equation 3.3.

$$\rho_{sample} = \frac{m_{in\ air} \cdot \rho_{water}}{m_{in\ air} - m_{in\ water}} \tag{3.3}$$

ρ_{sample}... Density of the sample in $g \cdot cm^{-3}$
ρ_{water}... Density of the water at measuring temperature in $g \cdot cm^{-3}$
$m_{in\ air}$... Mass of the sample in air in g
$m_{in\ water}$... Mass of the sample in water in g

3.10 Measurement of the Young's modulus

For the measurement of the Young's modulus the samples, prepared for the density measurement, were sent to RHP Technology GmbH. There they where tested using a OLYMPUS 38DL Plus ultrasonic thickness gauge. This method relies on the measurement of sound velocities (transverse and longitudinal) in a given material. Together with the materials density the Young's modulus can be calculated.

The velocities were determined by experiment and follow Equation 3.4.

$$v = \frac{d}{\frac{t}{2}} \tag{3.4}$$

v... Sound velocity in $m \cdot s^{-1}$
d... Thickness of the sample in m
t... Round trip transit time in s

The measured velocities are then used to calculate the Poisson's ratio, which represents the ratio of transverse and axial strains on a material stressed along one axis. This results in Equation 3.5.

$$\nu = \frac{1 - 2 \cdot (\frac{v_T}{v_L})^2}{2 - 2 \cdot (\frac{v_T}{v_L})^2} \tag{3.5}$$

ν... Poisson's Ratio

v_T... Transverse velocity in $m \cdot s^{-1}$

v_L... Longitudinal velocity in $m \cdot s^{-1}$

With the Poisson's ratio calculated the Young's modulus can be obtained via Equation 3.6.

$$E = \frac{v_L^2 \cdot \rho \cdot (1 + \nu) \cdot (1 - 2 \cdot \nu)}{1 - \nu} \tag{3.6}$$

3.11 X-ray diffractometry

Diffraction experiments were conducted for all extruded and heat-treated samples. For the measurements, small pieces were cut from the existing rods and measured in a PANalytical X'Pert MPDII in Bragg-Brentano geometry with a rotating sample holder. For the experiments copper K_α radiation was used. The start position was set to 10 $2°\theta$ and ended at 110 $2°\theta$. The measurement time was 54 min.

3.12 Heat treatment

To obtain a homogeneous microstructure and to either dissolve residual metallic particles or to promote a reaction between the reinforcements and the matrix in the extruded samples, diffusion annealing was conducted. Two heat treatments, that varied in the holding time were carried out (Table 6). After first tests, it was decided to only use option 2 throughout the experiments.

Table 6: Heat treatments

Option	atmosphere	flushing time (min)	heat rate / °C/min	holding temperature / °C	holding time / h
1	Argon	15	10	1000	30
2	Argon	15	10	1000	90

4 Results and discussion

4.1 Extruded samples

In sum nine different compositions are studied. For each system a sample without particle reinforcement, one with 3vol% TiC and one with 3vol% B_4C is extruded. The systems marked with a star were produced by A. Zunghammer [41] and are used for comparison. These samples were obtained in the as-extruded state and are heat-treated in addition. Furthermore, in the pure Ti systems there is a difference in the particle size of B_4C (F500/F2000) and an additional sample with 6vol% B_4C F500 is extruded. An overview of the extruded samples is shown in Figure 7.

Table 7: Overview of the extruded samples

	Ti	
Ti*	Ti+3vol% TiC	
Ti+3vol% B_4C F2000*	Ti+3vol% B_4C F500*	Ti+6vol% B_4C F500
	Ti-6Al-4V	
Ti-6Al-4V*	Ti-6Al-4V+3vol% TiC	Ti-6Al-4V+3vol% B_4C*
	Ti-6.5Cu	
Ti-6.5Cu*	Ti-6.5Cu+3vol% TiC	Ti-6.5Cu+3vol% B_4C
	Ti-6.4Ni-2Fe	
Ti-6.4Ni-2Fe	Ti-6.4Ni-2Fe+3vol% TiC	Ti-6.4Ni-2Fe+3vol% B_4C
	Ti-6.4Ni-2Cr	
Ti-6.4Ni-2Cr	Ti-6.4Ni-2Cr+3vol% TiC	Ti-6.4Ni-2Cr+3vol% B_4C
	Ti-8Al-1Mo-1V	
Ti-8Al-1Mo-1V	Ti-8Al-1Mo-1V+3vol% TiC	Ti-8Al-1Mo-1V+3vol% B_4C
	Ti-5.7Al-5Co-3.8V	
Ti-5.7Al-5Co-3.8V	Ti-5.7Al-5Co-3.8V+3vol% TiC	Ti-5.7Al-5Co-3.8V+3vol% B_4C
	Ti-4Al-3Cu-2Fe	
Ti-4Al-3Cu-2Fe	Ti-4Al-3Cu-2Fe+3vol% TiC	Ti-4Al-3Cu-2Fe+3vol% B_4C
	Ti-10Al-1.4Nb-0.8Cr	
Ti-10Al-1.4Nb-0.8Cr		

*Extruded by A. Zunghammer

4.1.1 Ti

Figures 8 a-b and 9 a-b show the microstructure of the as-extruded Ti sample. A optically dense and homogeneous microstructure is obtained. There is no visible difference in the observed extrusion direction. Heat treatment results in grain growth (Figure 8 c-d and 9 c-d). The phase present is α-Ti. The addition of 3 vol% TiC results in a finer microstructure (Figure 10 a-b and 11 a-b). Again a optically dense and homogeneous material is obtained and no structural anisotropy is observed. After heat treatment, grain growth was observed and the TiC particles remained (Figure 10 c-d and 11 c-d). The addition of 3vol% B_4C F2000 leads to a much finer microstructure (Figure 12 a-b and 13 a-b). However, a texture is observed in the extrusion direction. The heat-treated sample shows grain growth and the formation of needle shaped titanium borides (Figure 12 c-d and 13 c-d). The addition of the coarser 3vol% B_4C F500 also results in a finer microstructure, but not as refined as with the F2000 grain size (Figure 14 a-b and 15 a-b). There is no difference in the observed direction. Heat treatment also leads to grain growth and the formation of titanium borides. With the addition of 6vol% B_4C F500 an analogous microstructure is observed, only with more B_4C present (Figure 16 and 17).

For all B_4C-MMCs no boron could be identified with EDS due to the low sensitivity for boron. However, when one compares the SEM images in the as-extruded and heat-treated state a clear difference in the contrast can be seen, indicating a conversion from low Z" contrast particles as it is known for B_4C to more greyish ones because of a reaction with the titanium matrix. In addition, both the XRD measurements (Chapter 4.7) and comparison with literature confirm the presence of B_4C and its reaction to titanium carbide and titanium boride. The characteristic shape of accicular titanium borides and/or the whisker formation from globular titanium borides found throughout all B_4C-MMCs are in good agreement with the literature [42–44].

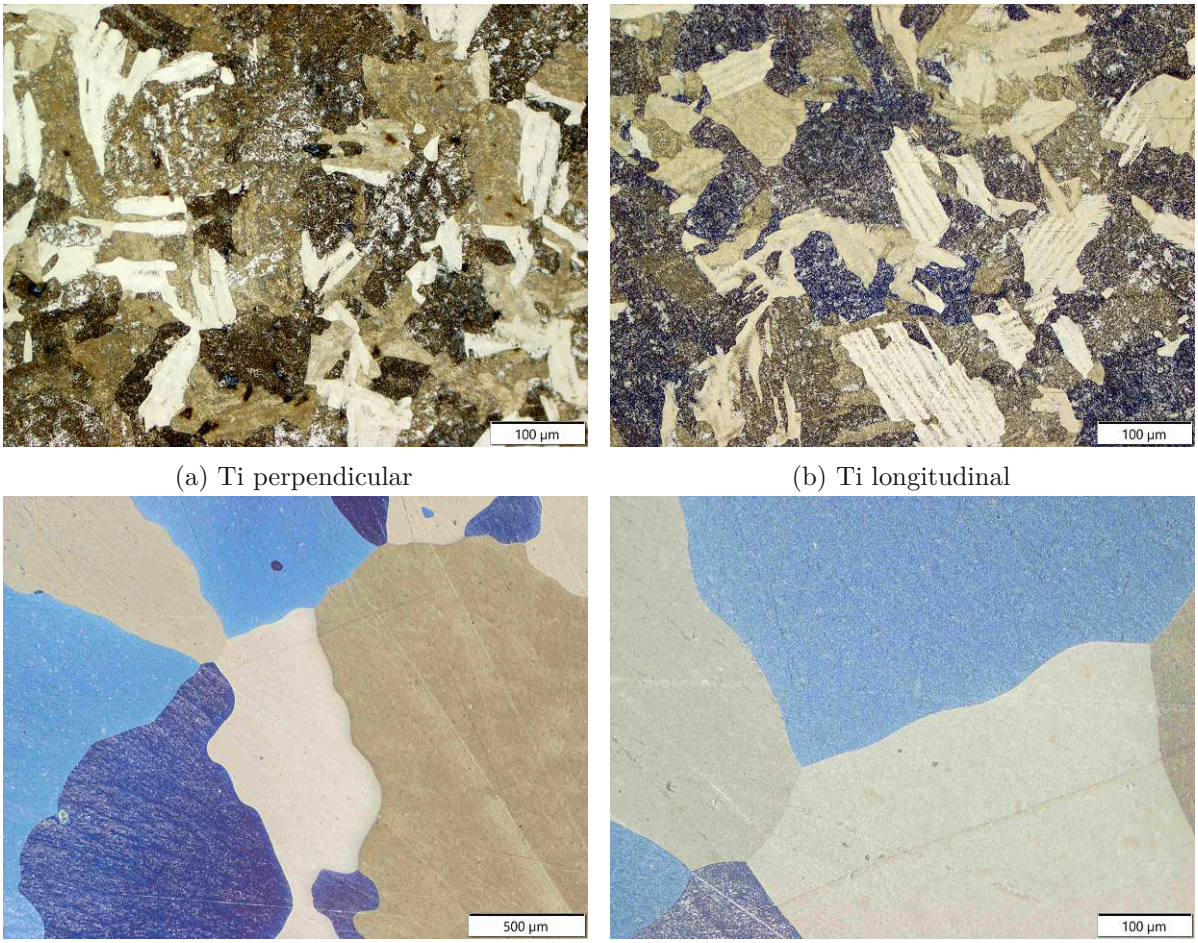

(a) Ti perpendicular

(b) Ti longitudinal

(c) Ti 1000 °C/90h perpendicular

(d) Ti 1000 °C/90h perpendicular

Figure 8: Optical microscopy of the etched Ti as-extruded samples (a-b) and the heat-treated samples (c-d)

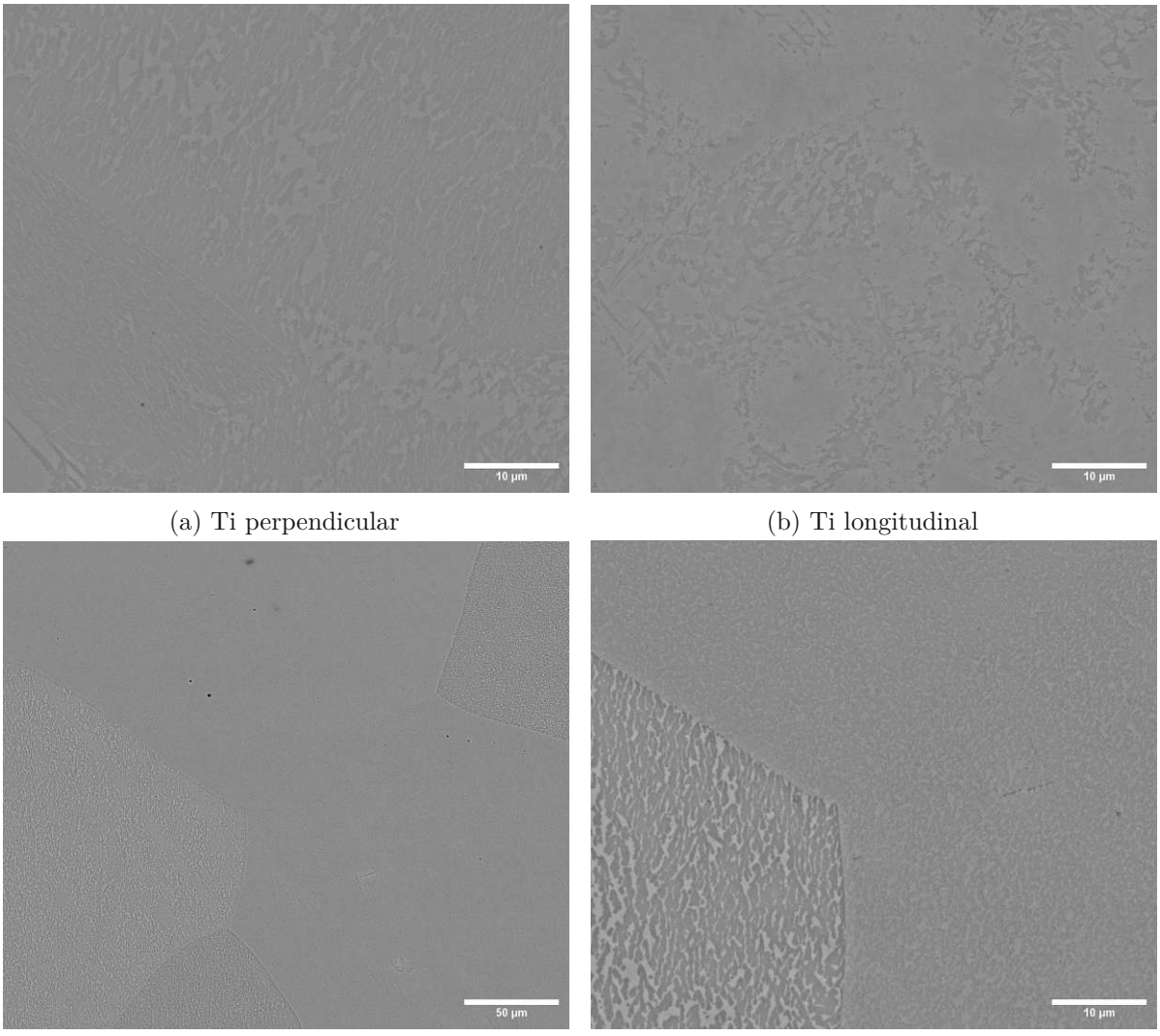

(a) Ti perpendicular

(b) Ti longitudinal

(c) Ti 1000 °C/90h perpendicular

(d) Ti 1000 °C/90h perpendicular

Figure 9: SEM images of the etched Ti as-extruded samples (a-b), and the heat-treated samples (c-d)

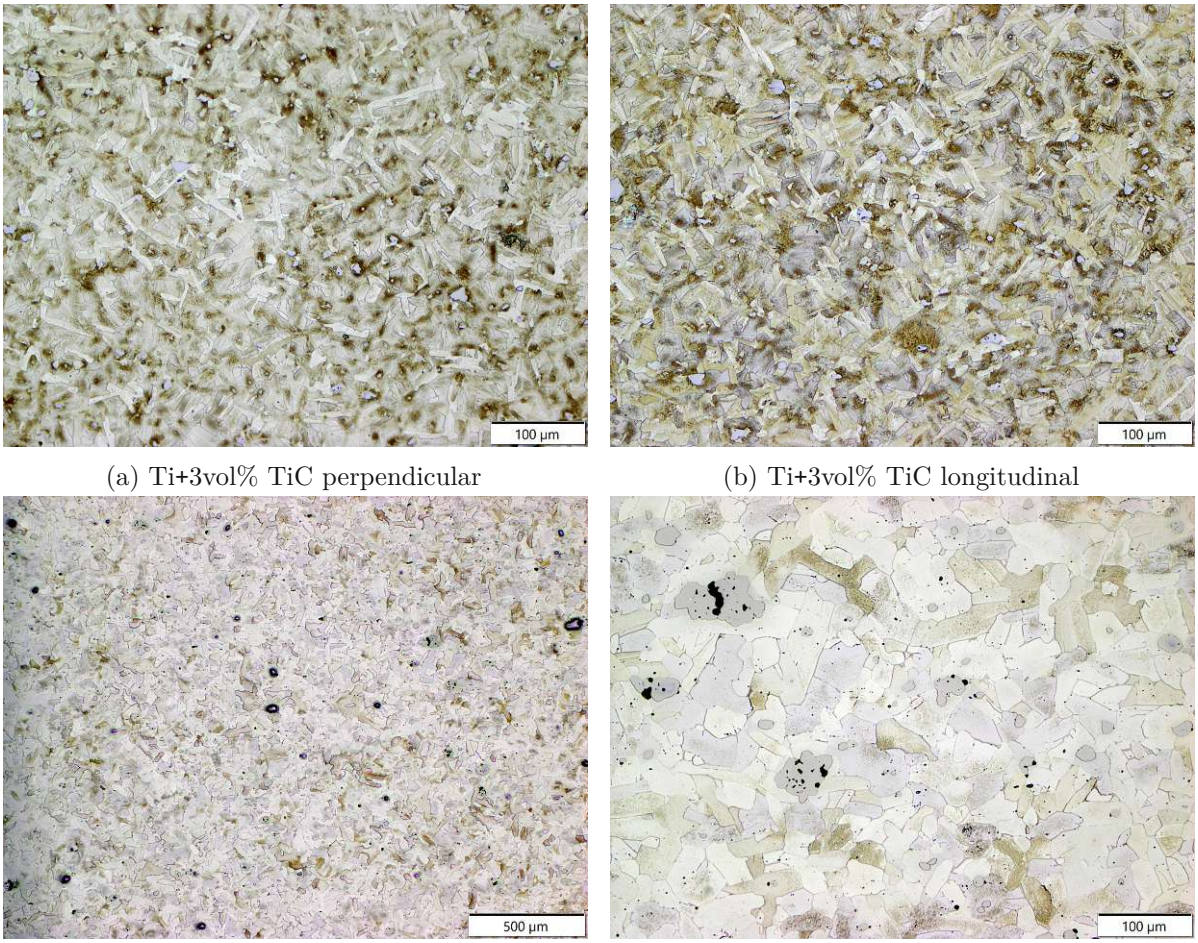

(a) Ti+3vol% TiC perpendicular

(b) Ti+3vol% TiC longitudinal

(c) Ti+3vol% TiC 1000 °C/90h perpendicular

(d) Ti+3vol% TiC 1000 °C/90h perpendicular

Figure 10: Optical microscopy of the etched Ti+3vol% TiC as-extruded samples (a-b) and the heat-treated samples (c-d)

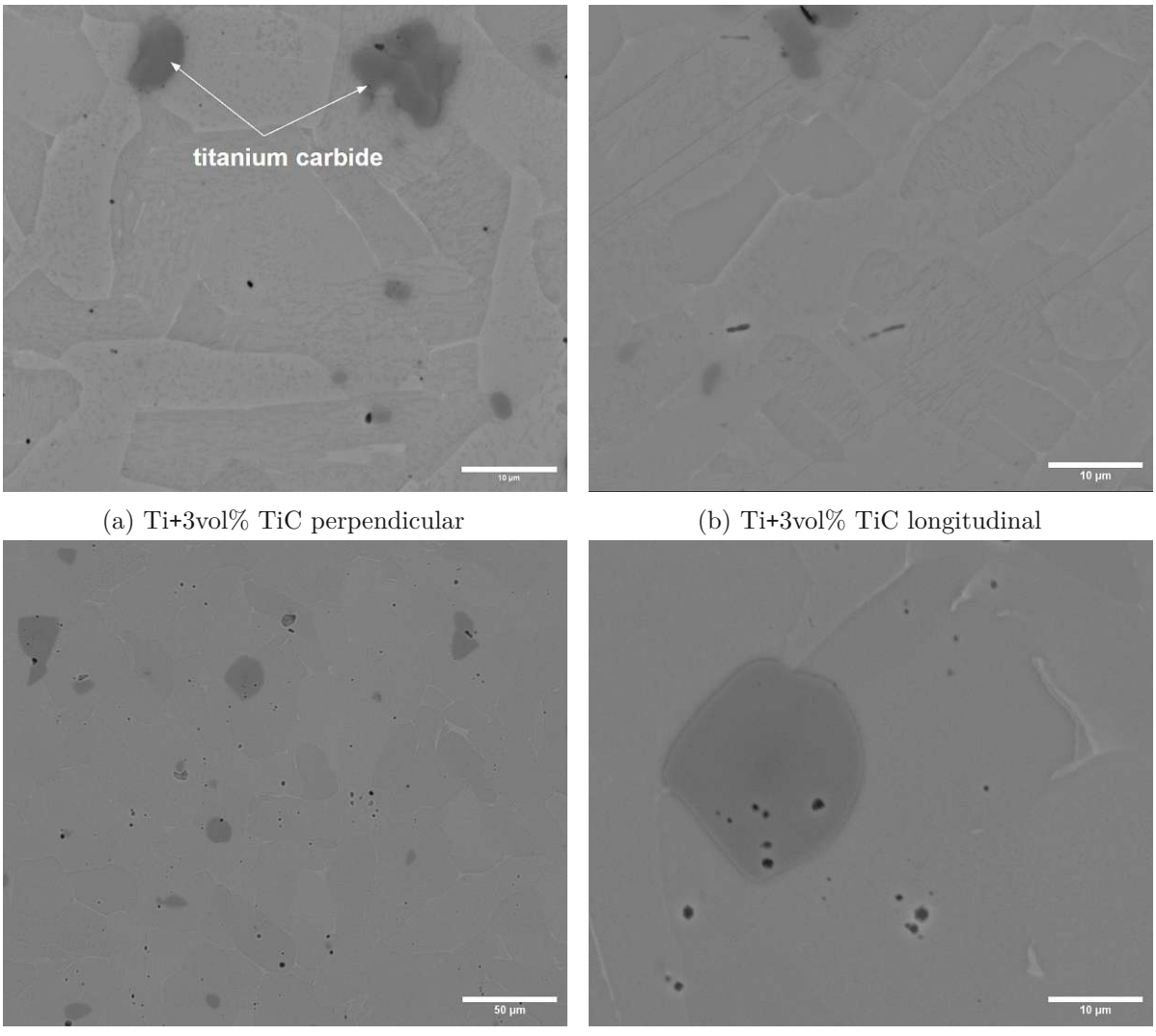

(a) Ti+3vol% TiC perpendicular

(b) Ti+3vol% TiC longitudinal

(c) Ti+3vol% TiC 1000 °C/90h perpendicular

(d) Ti+3vol% TiC 1000 °C/90h perpendicular

Figure 11: SEM images of the etched Ti+3vol% TiC as-extruded samples (a-b), and the heat-treated samples (c-d)

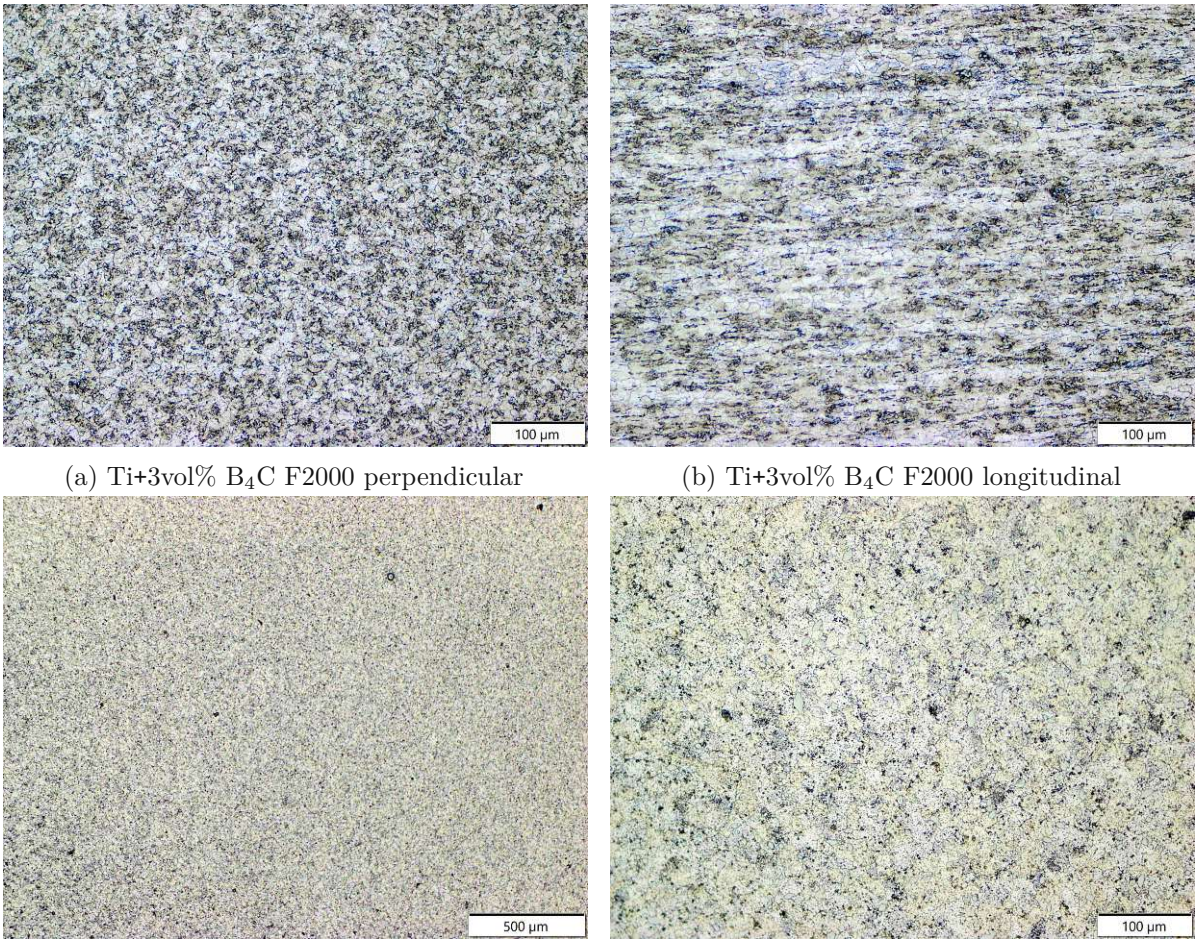

(a) Ti+3vol% B_4C F2000 perpendicular

(b) Ti+3vol% B_4C F2000 longitudinal

(c) Ti+3vol% B_4C F2000 1000 °C/90h perpendicular

(d) Ti+3vol% B_4C F2000 1000 °C/90h perpendicular

Figure 12: Optical microscopy of the etched Ti +3vol% B_4C F2000 as-extruded samples (a-b) and the heat-treated samples (c-d)

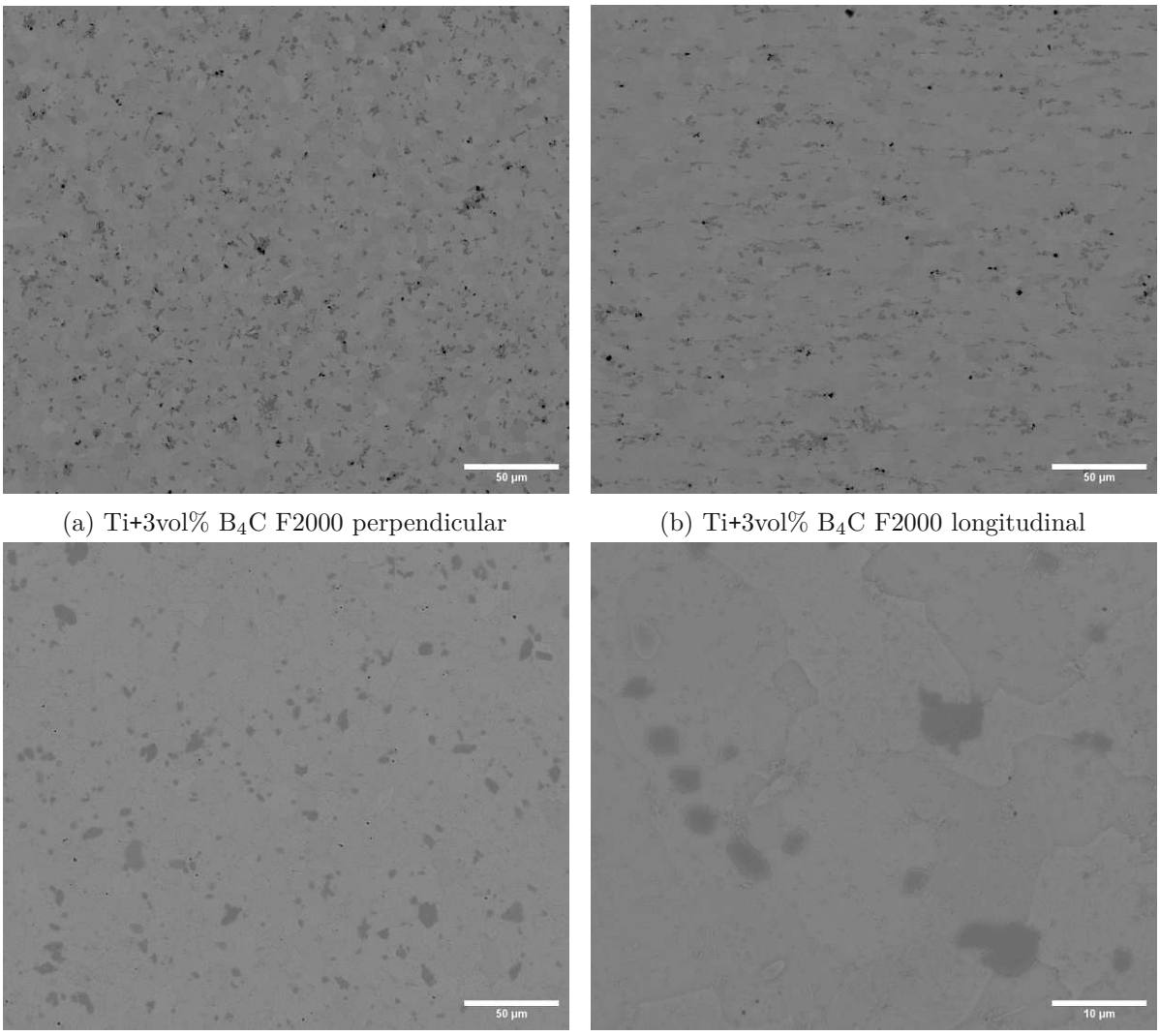

(a) Ti+3vol% B_4C F2000 perpendicular

(b) Ti+3vol% B_4C F2000 longitudinal

(c) Ti+3vol% B_4C F2000 1000 °C/90h perpendicular

(d) Ti+3vol% B_4C F2000 1000 °C/90h perpendicular

Figure 13: SEM images of the etched Ti +3vol% B_4C F2000 as-extruded samples (a-b), and the heat-treated samples (c-d)

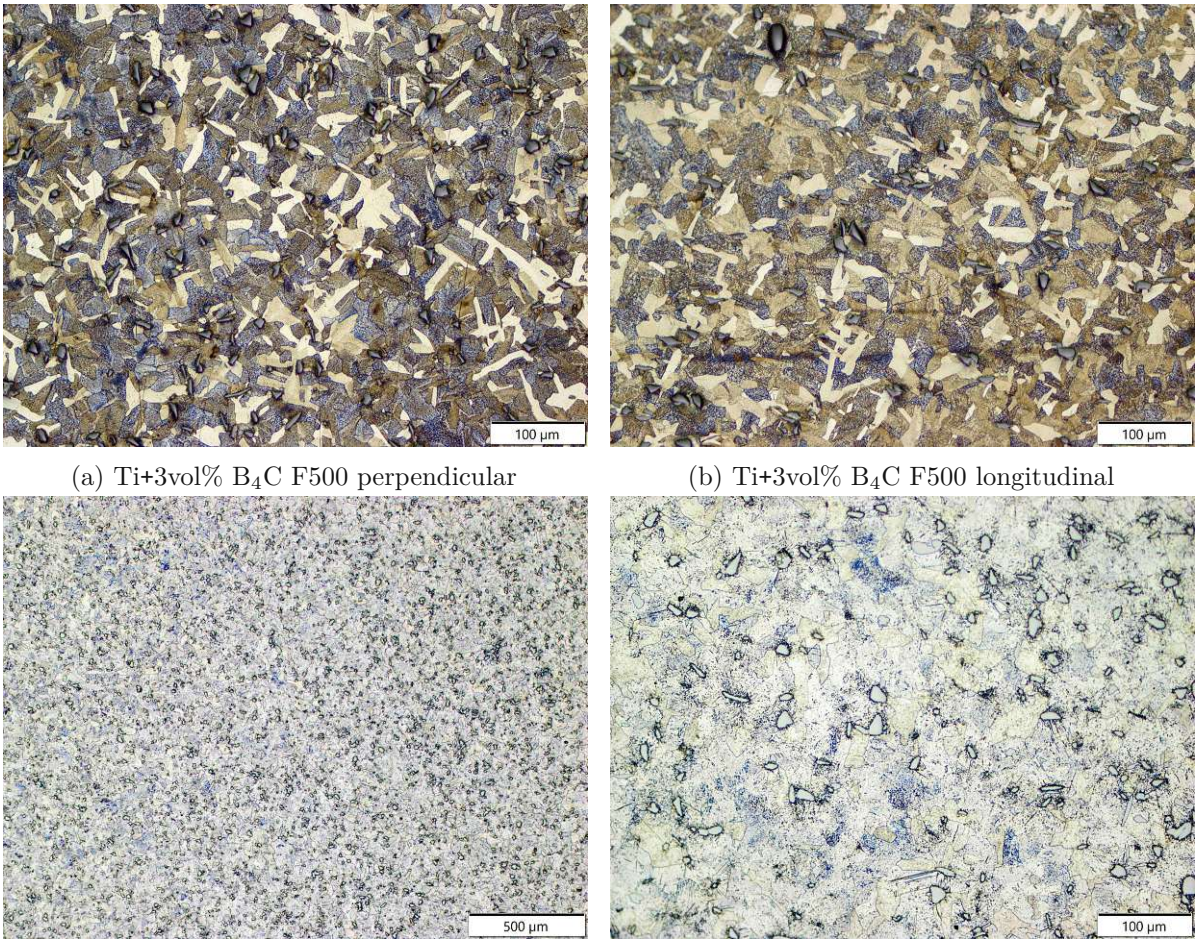

(a) Ti+3vol% B_4C F500 perpendicular

(b) Ti+3vol% B_4C F500 longitudinal

(c) Ti+3vol% B_4C F500 1000 °C/90h perpendicular

(d) Ti+3vol% B_4C F500 1000 °C/90h perpendicular

Figure 14: Optical microscopy of the etched Ti +3vol% B_4C F500 as-extruded samples (a-b) and the heat-treated samples (c-d)

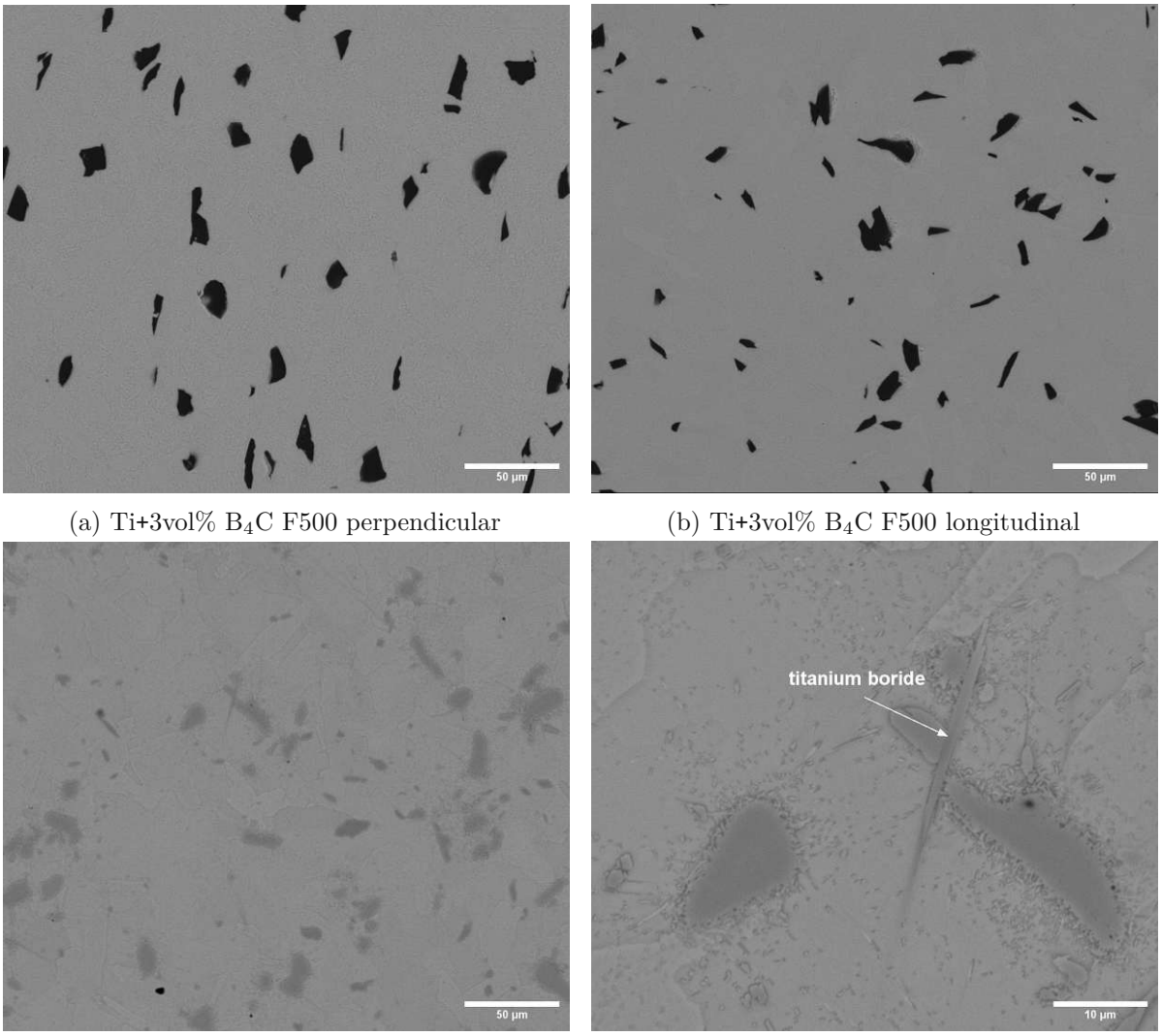

(a) Ti+3vol% B_4C F500 perpendicular

(b) Ti+3vol% B_4C F500 longitudinal

(c) Ti+3vol% B_4C F500 1000 °C/90h perpendicular

(d) Ti+3vol% B_4C F500 1000 °C/90h perpendicular

Figure 15: SEM images of the etched Ti+3vol% B_4C F500 as-extruded samples (a-b), and the heat-treated samples (c-d)

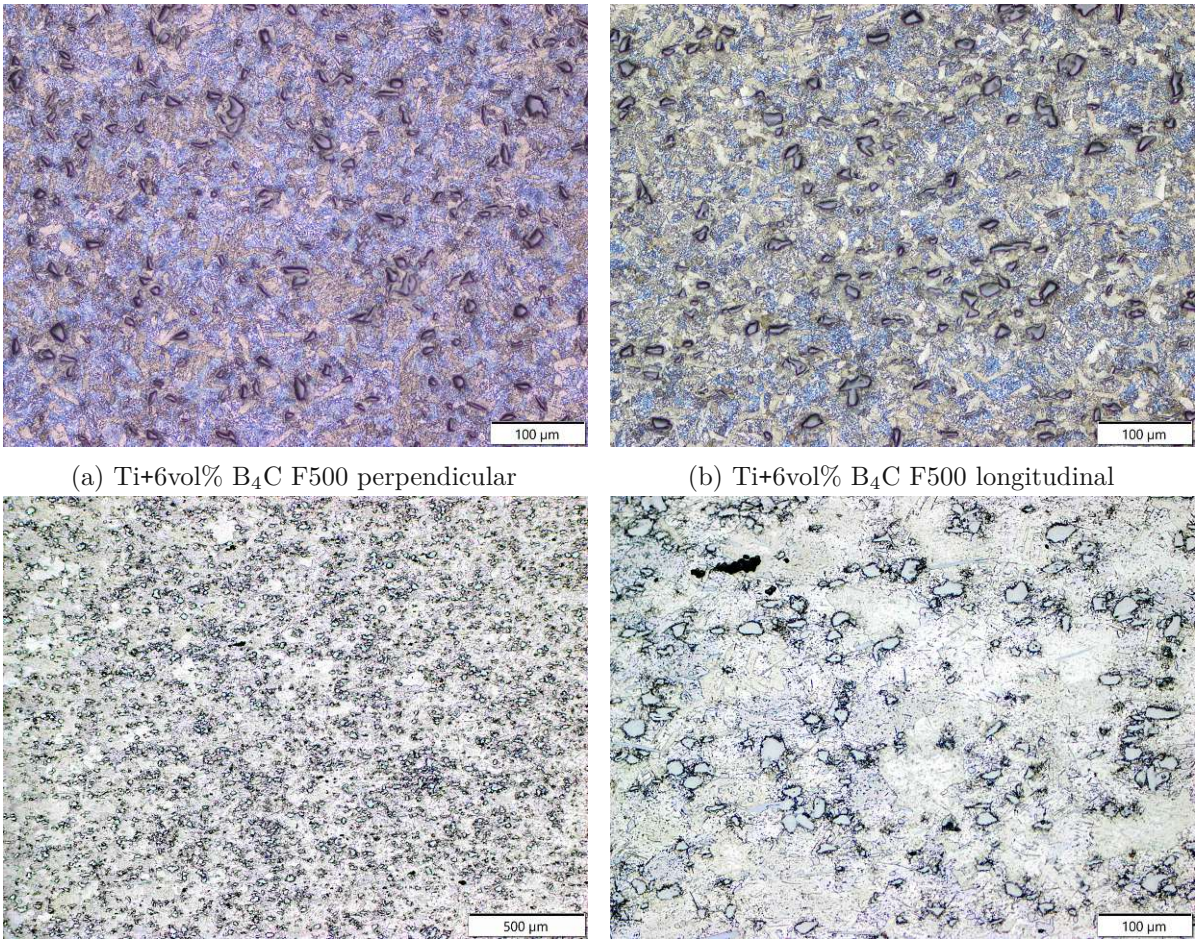

(a) Ti+6vol% B_4C F500 perpendicular

(b) Ti+6vol% B_4C F500 longitudinal

(c) Ti+6vol% B_4C F500 1000 °C/90h perpendicular

(d) Ti+6vol% B_4C F500 1000 °C/90h perpendicular

Figure 16: Optical microscopy of the etched Ti+6vol% B_4C F500 as-extruded samples (a-b) and the heat-treated samples (c-d)

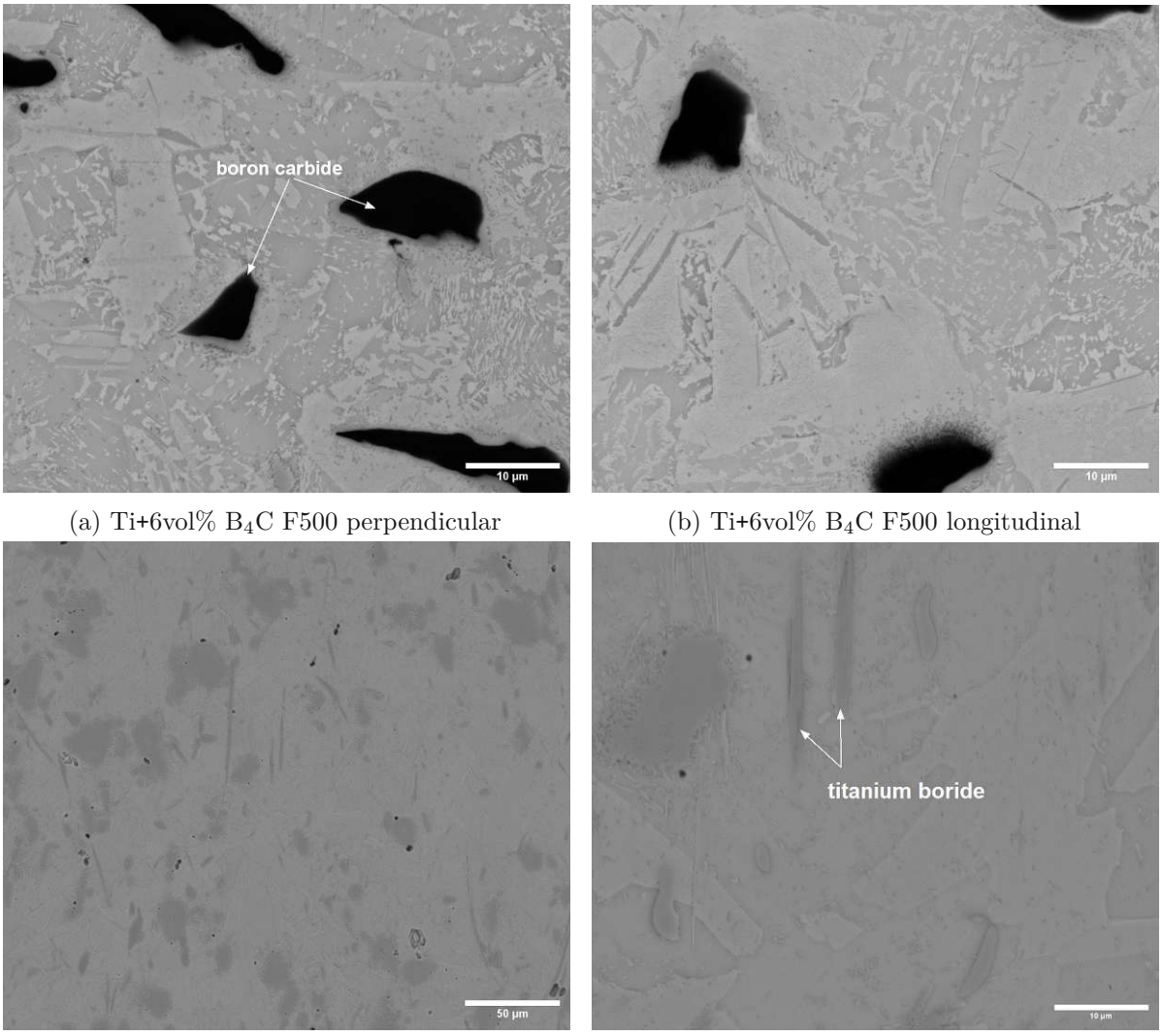

(a) Ti+6vol% B_4C F500 perpendicular

(b) Ti+6vol% B_4C F500 longitudinal

(c) Ti+6vol% B_4C F500 1000 °C/90h perpendicular

(d) Ti+6vol% B_4C F500 1000 °C/90h perpendicular

Figure 17: SEM images of the etched Ti+6vol% B_4C F500 as-extruded samples (a-b), and the heat-treated samples (c-d)

4.1.2 Ti-6Al-4V systems

As the Ti-6Al-4V alloy is the most established, particle reinforced systems are produced. Figures 18 a-b and 19 a-b show the microstructure of the as-extruded Ti-6Al-4V sample. A homogeneous and optically dense material is obtained and no structural difference in the examined directions can be detected. A lamellar two-phase structure is identified, consisting of α-Ti grains surrounded by β-Ti at the grain boundaries. After heat treatment, significant grain growth is observed (Figure 18 c-d and 19 c-d). The addition of 3vol% TiC resulted in a finer microstructure as shown in Figure 20 a-b and 21 a-b. The optical micrograph shows a texture in the longitudinal direction, which is not visible in the electron microscope. The heat treatment results in a noticeable structural transformation leading to a bimodal microstructure (Figure 20 c-d and 21 c-d). The TiC particles remain. The addition of 3vol% B_4C has a similar refining effect as TiC (Figure 22 a-b and 23 a-b). In addition, a bimodal microstructure and the formation of needle-shaped titanium borides occur after heat treatment (Figure 22 c-d and 23 c-d).

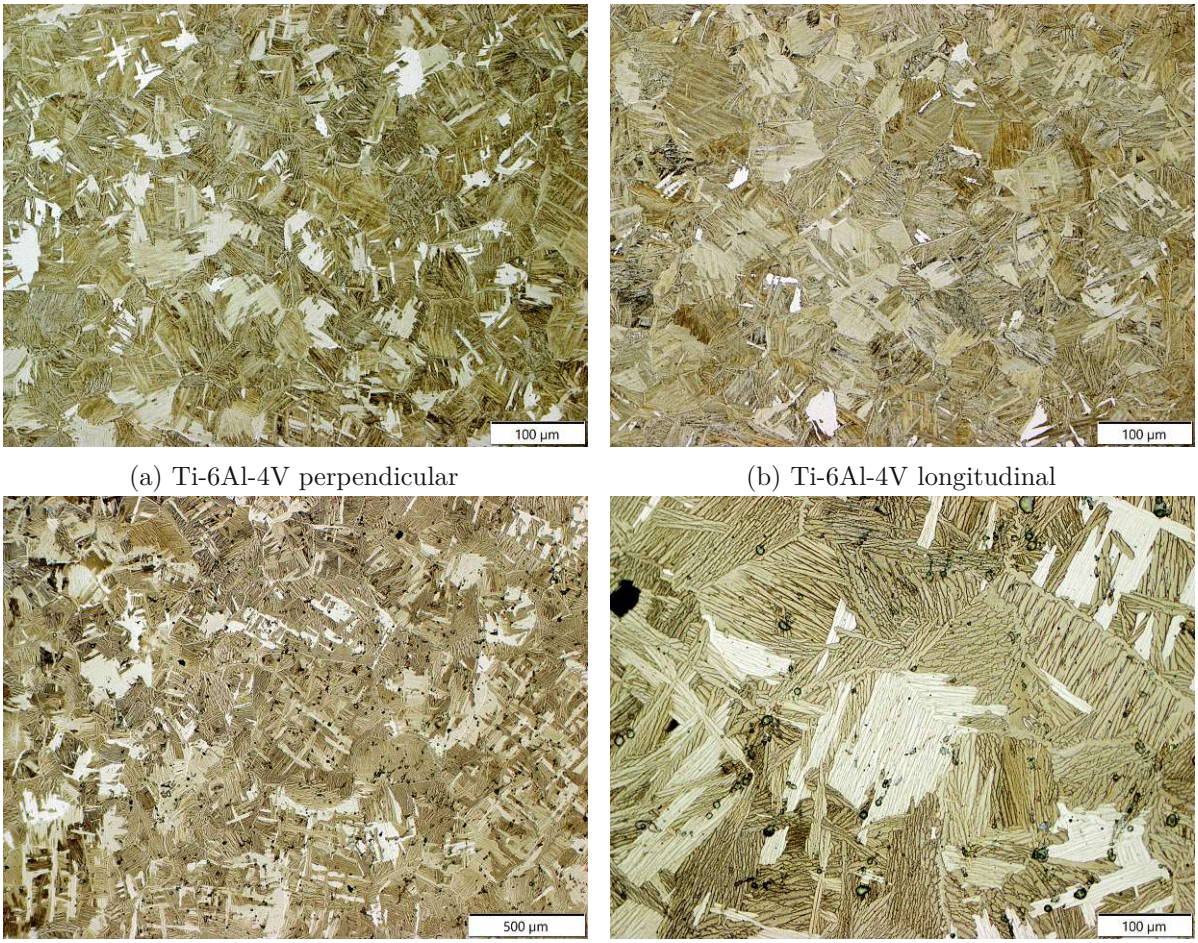

(a) Ti-6Al-4V perpendicular

(b) Ti-6Al-4V longitudinal

(c) Ti-6Al-4V 1000 °C/90h perpendicular

(d) Ti 1000 °C/90h perpendicular

Figure 18: Optical microscopy of the etched Ti-6Al-4V as-extruded samples (a-b) and the heat-treated samples (c-d)

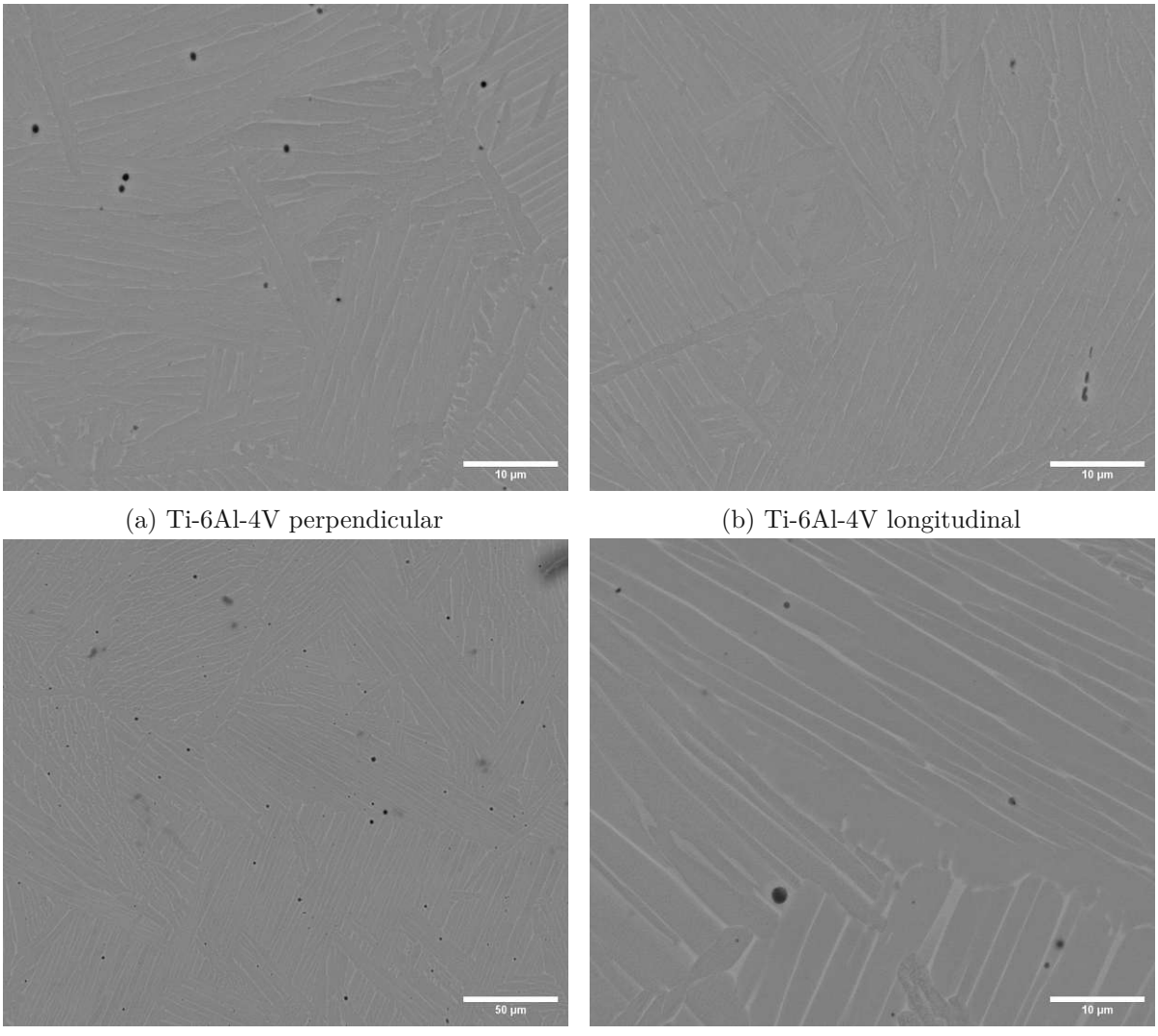

(a) Ti-6Al-4V perpendicular

(b) Ti-6Al-4V longitudinal

(c) Ti-6Al-4V 1000 °C/90h perpendicular

(d) Ti-6Al-4V 1000 °C/90h perpendicular

Figure 19: SEM images of the etched Ti-6Al-4V as-extruded samples (a-b), and the heat-treated samples (c-d)

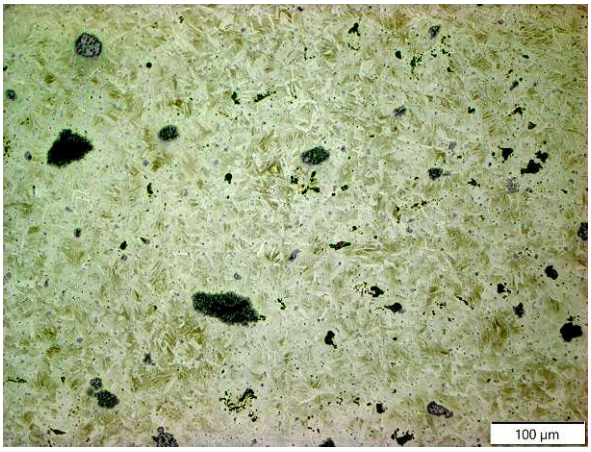

(a) Ti-6Al-4V+3vol% TiC perpendicular

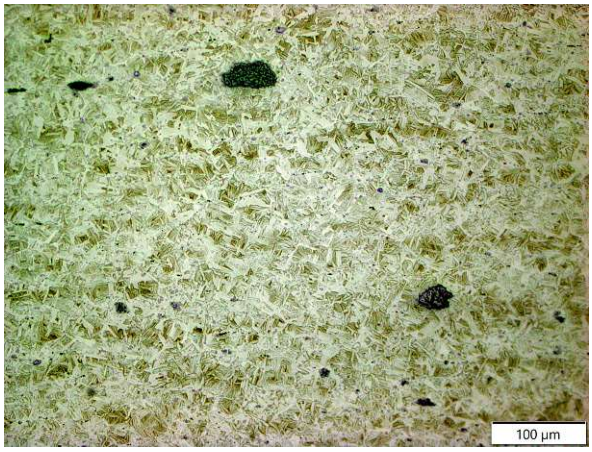

(b) Ti-6Al-4V+3vol% TiC longitudinal

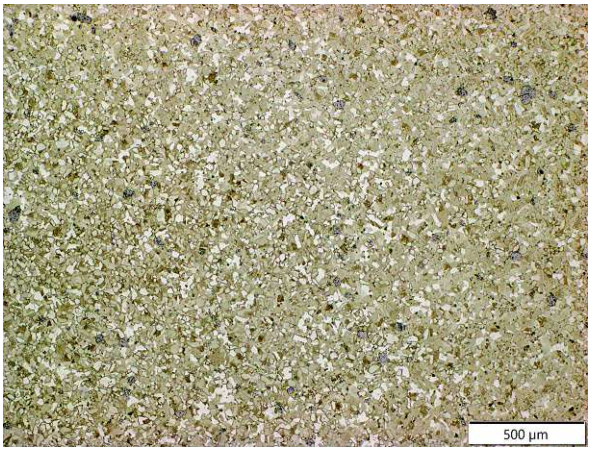

(c) Ti-6Al-4V+3vol% TiC 1000 °C/90h perpendicular

(d) Ti-6Al-4V+3vol% TiC 1000 °C/90h perpendicular

Figure 20: Optical microscopy of the etched Ti-6Al-4V+3vol%TiC as-extruded samples (a-b) and the heat-treated samples (c-d)

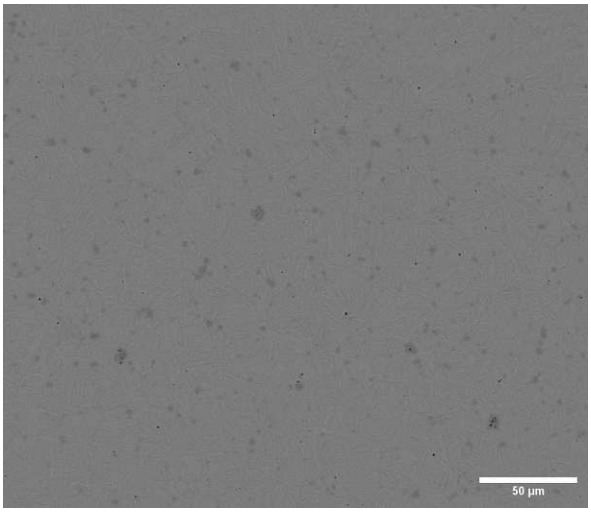

(a) Ti-6Al-4V+3vol% TiC perpendicular

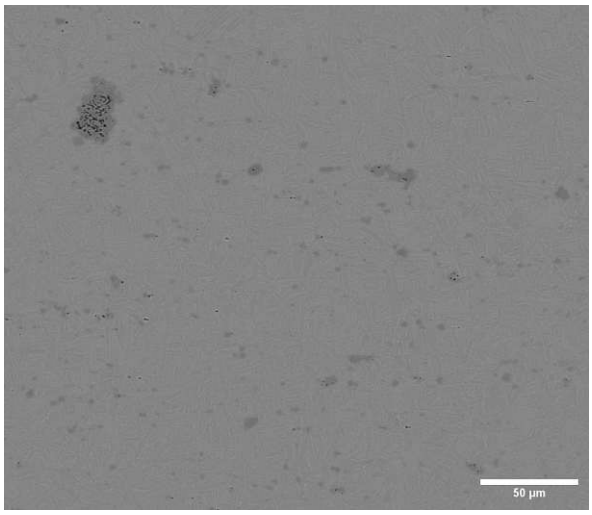

(b) Ti-6Al-4V+3vol% TiC longitudinal

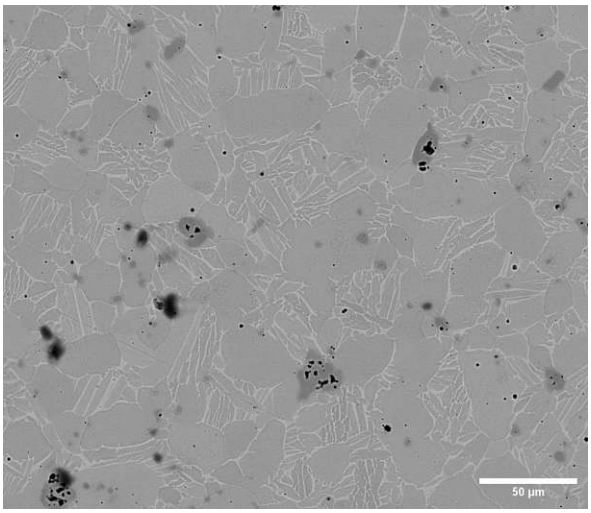

(c) Ti-6Al-4V+3vol% TiC 1000 °C/90h perpendicular

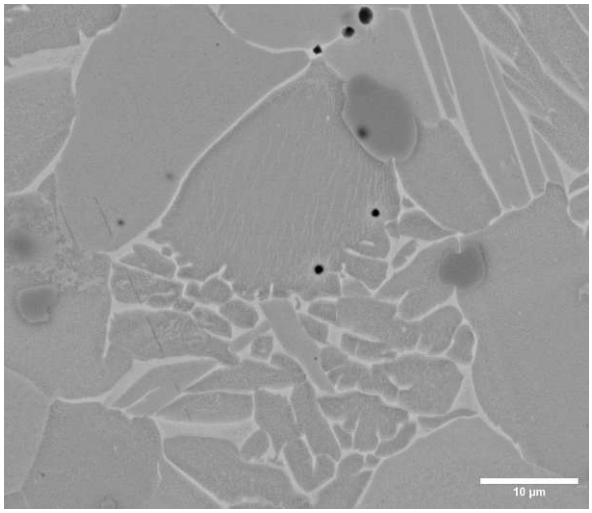

(d) Ti-6Al-4V+3vol% TiC 1000 °C/90h perpendicular

Figure 21: SEM images of the etched Ti-6Al-4V+3vol% TiC as-extruded samples (a-b), and the heat-treated samples (c-d)

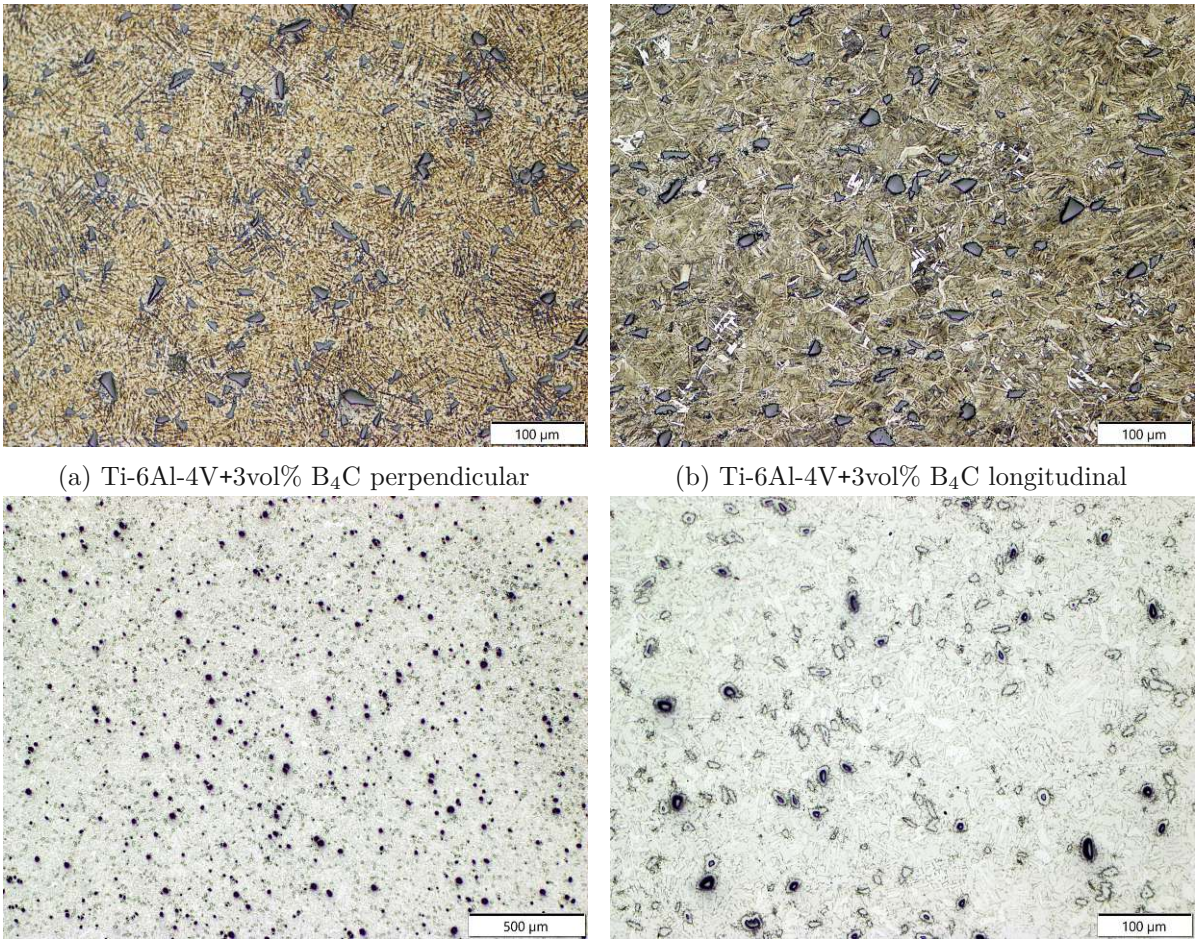

(a) Ti-6Al-4V+3vol% B_4C perpendicular

(b) Ti-6Al-4V+3vol% B_4C longitudinal

(c) Ti-6Al-4V+3vol% B_4C 1000 °C/90h perpendicular

(d) Ti-6Al-4V+3vol% B_4C 1000 °C/90h perpendicular

Figure 22: Optical microscopy of the etched Ti-6Al-4V+3vol% B_4C as-extruded samples (a-b) and the heat-treated samples (c-d)

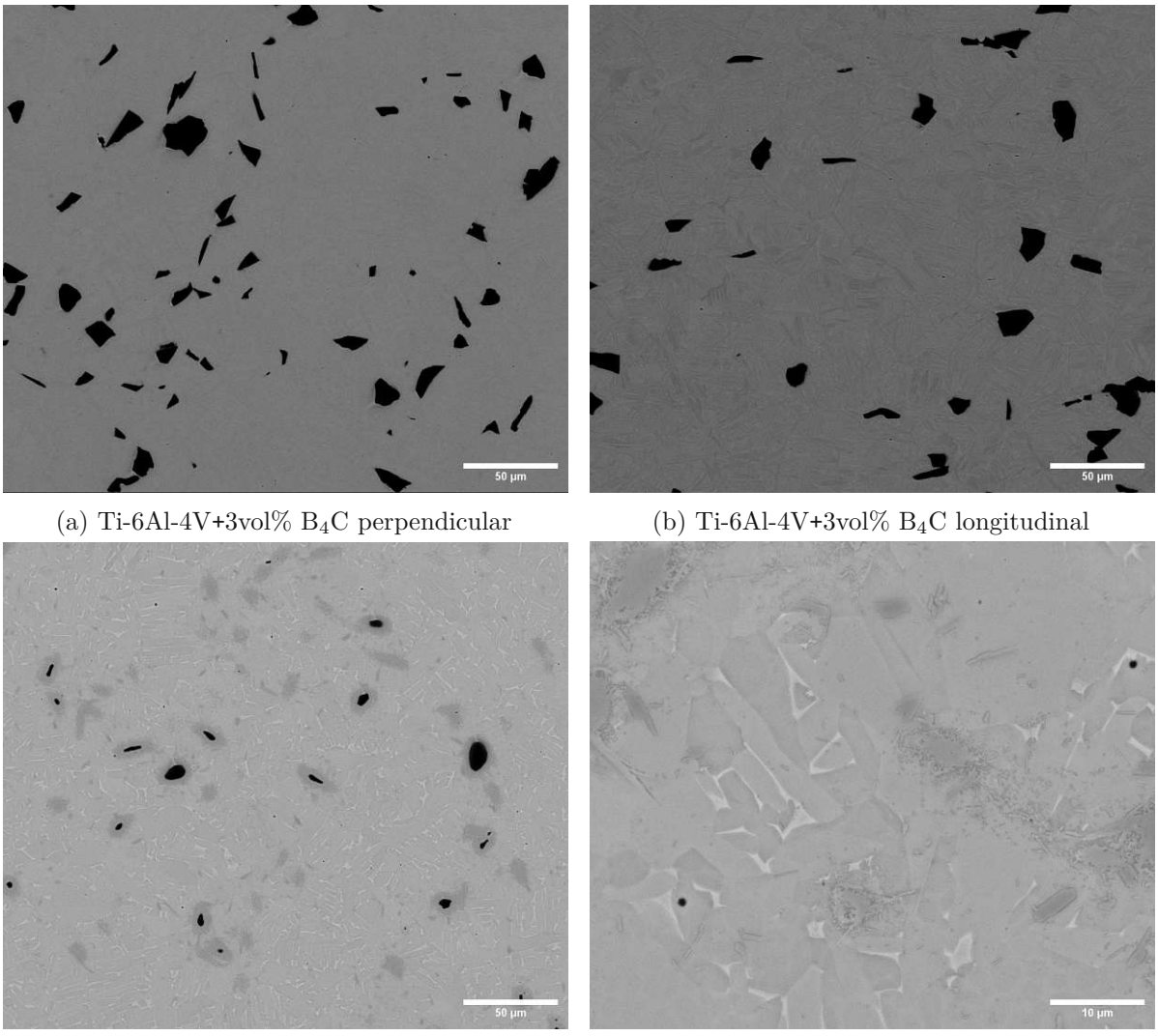

(a) Ti-6Al-4V+3vol% B_4C perpendicular

(b) Ti-6Al-4V+3vol% B_4C longitudinal

(c) Ti-6Al-4V+3vol% B_4C 1000 °C/90h perpendicular

(d) Ti-6Al-4V+3vol% B_4C 1000 °C/90h perpendicular

Figure 23: SEM images of the etched Ti-6Al-4V+3vol% B_4C as-extruded samples (a-b), and the heat-treated samples (c-d)

4.1.3 Ti-6.5Cu systems

The idea behind the Ti-6.5Cu system is to improve the strength and inhibit stem crystal growth due to the eutectoid reaction of β-Ti to α-Ti and Ti_2Cu. The addition of Cu leads to an increase in the hardness [30]. Figures 24 a-b and 25 a-b show the microstructure of the as-extruded Ti-6.5Cu sample. The optical micrographs show no difference in the microstructure with respect to the observed direction. It consists of macro-grains formed by previous β-Ti in which the primary α-Ti starts growing. In the space between the α-Ti grains the secondary α-Ti and Ti_2Cu phase develops. It can be seen that the Cu is already completely dissolved after the extrusion. After heat treatment (Figure 24 c-d and 25 c-d) a significant grain growth is visible and the eutectoid structure is also improved. The microstructure of the as-extruded Ti-6.5Cu+3vol% TiC is shown in Figure 26 a-b and 27 a-b. Again, there is no difference in the perpendicular and longitudinal directions. However, compared to the unreinforced Ti-6.5Cu, the microstructure is much finer and the macro-grains appear to be suppressed. In addition, the eutectoid structure is more developed. The heat treatment results in grain growth and the TiC particles remain (26 a-b 27 a-b). An analogous microstructure is observed with the addition of 3vol% B_4C, with the difference that the B_4C particles react after heat treatment to form TiC and acicular TiB (Figure 28 and 29).

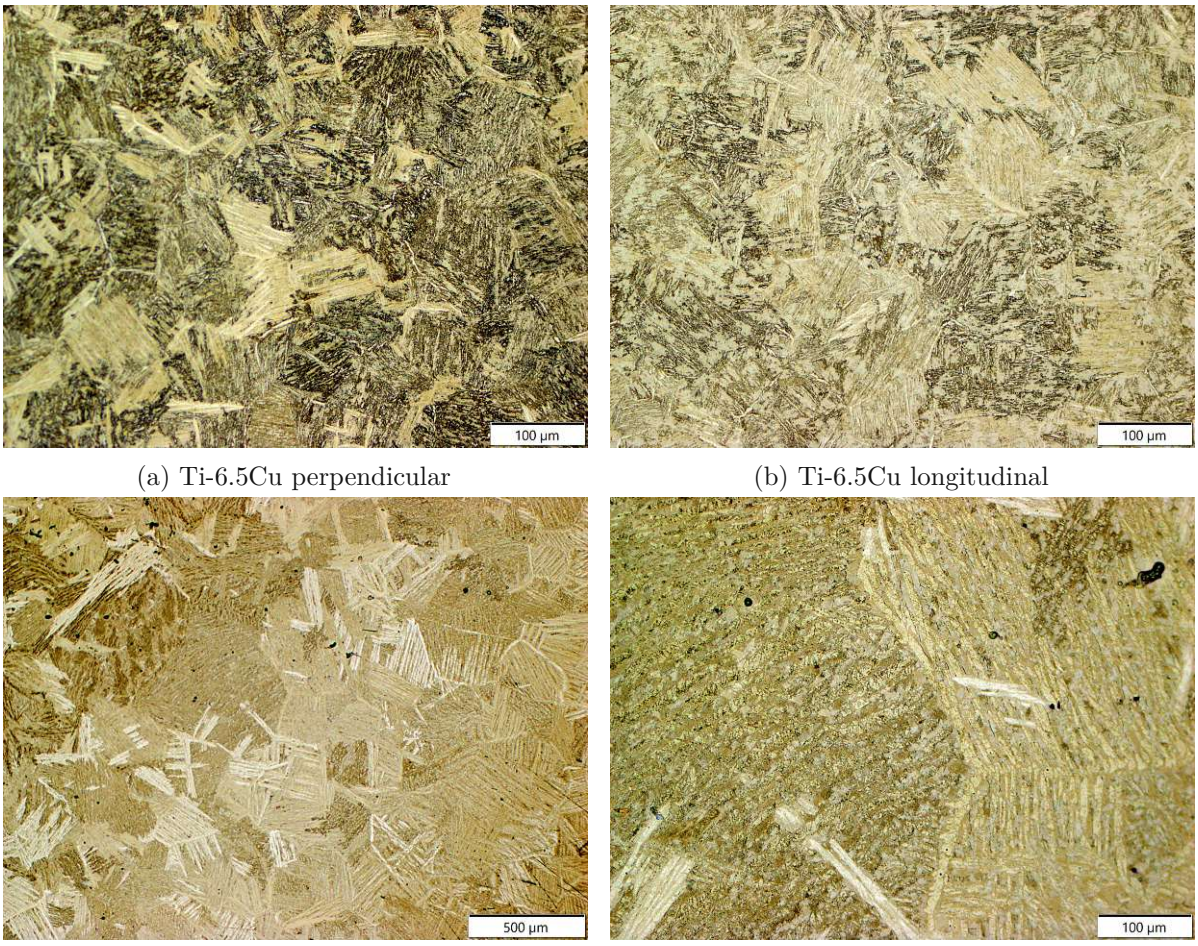

(a) Ti-6.5Cu perpendicular

(b) Ti-6.5Cu longitudinal

(c) Ti-6.5Cu 1000 °C/90h perpendicular

(d) Ti-6.5Cu 1000 °C/90h perpendicular

Figure 24: Optical microscopy of the etched Ti-6.5Cu as-extruded samples (a-b) and the heat-treated samples (c-d)

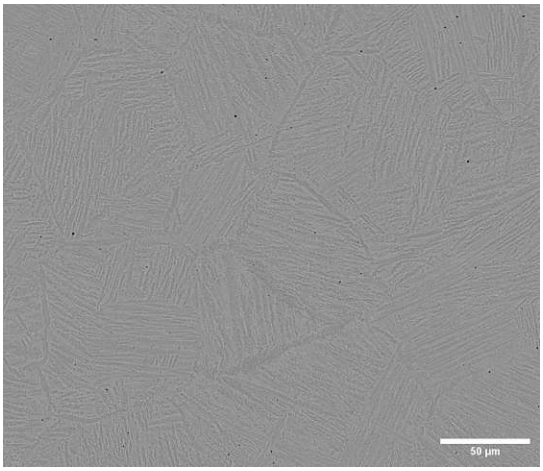

(a) Ti-6.5Cu perpendicular

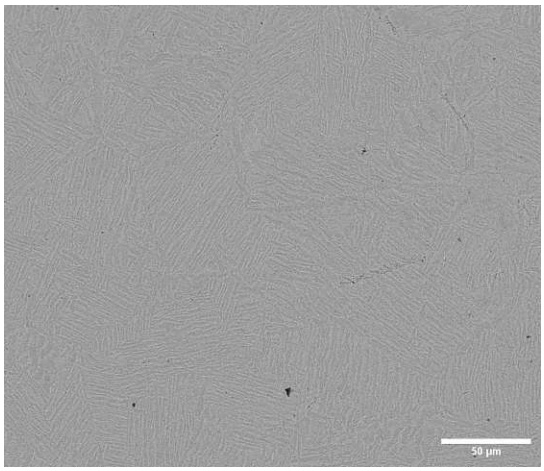

(b) Ti-6.5Cu longitudinal

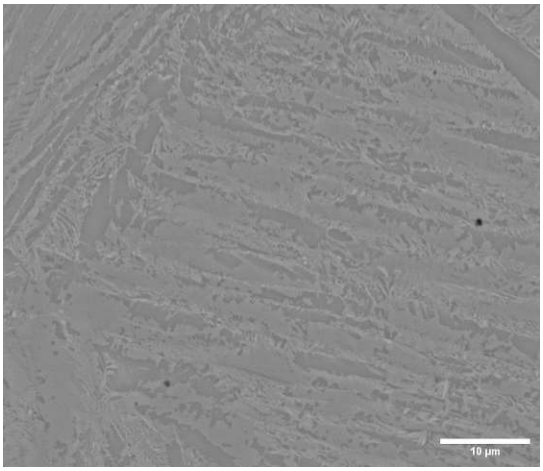

(c) Ti-6.5Cu perpendicular

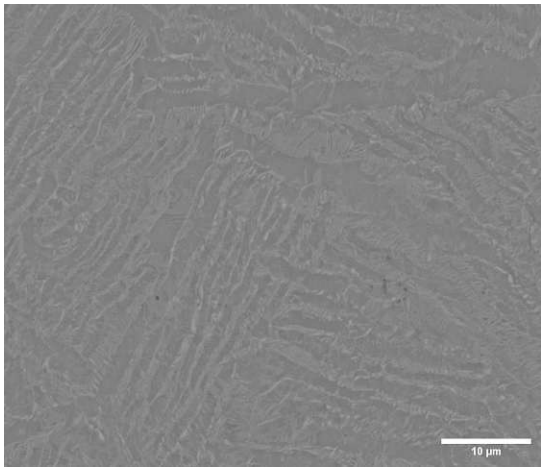

(d) Ti-6.5Cu longitudinal

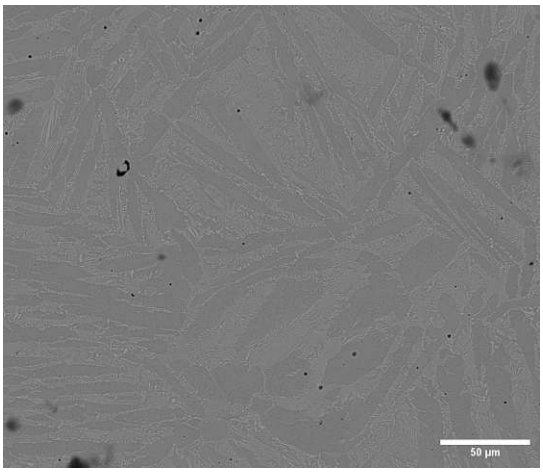

(e) Ti-6.5Cu 1000 °C/90h perpendicular

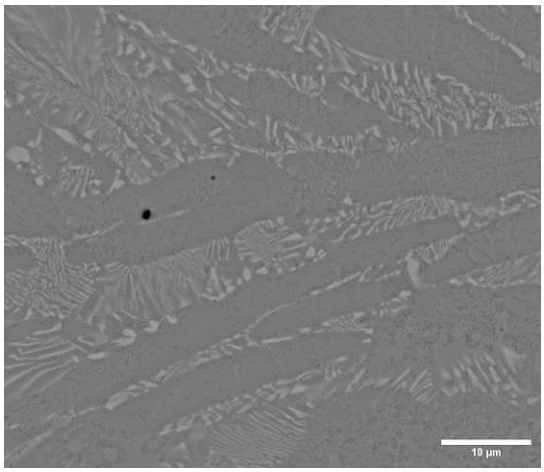

(f) Ti-6.5Cu 1000 °C/90h perpendicular

Figure 25: SEM images of the etched Ti-6.5Cu as-extruded samples (a-d) and the heat-treated samples (e-f)

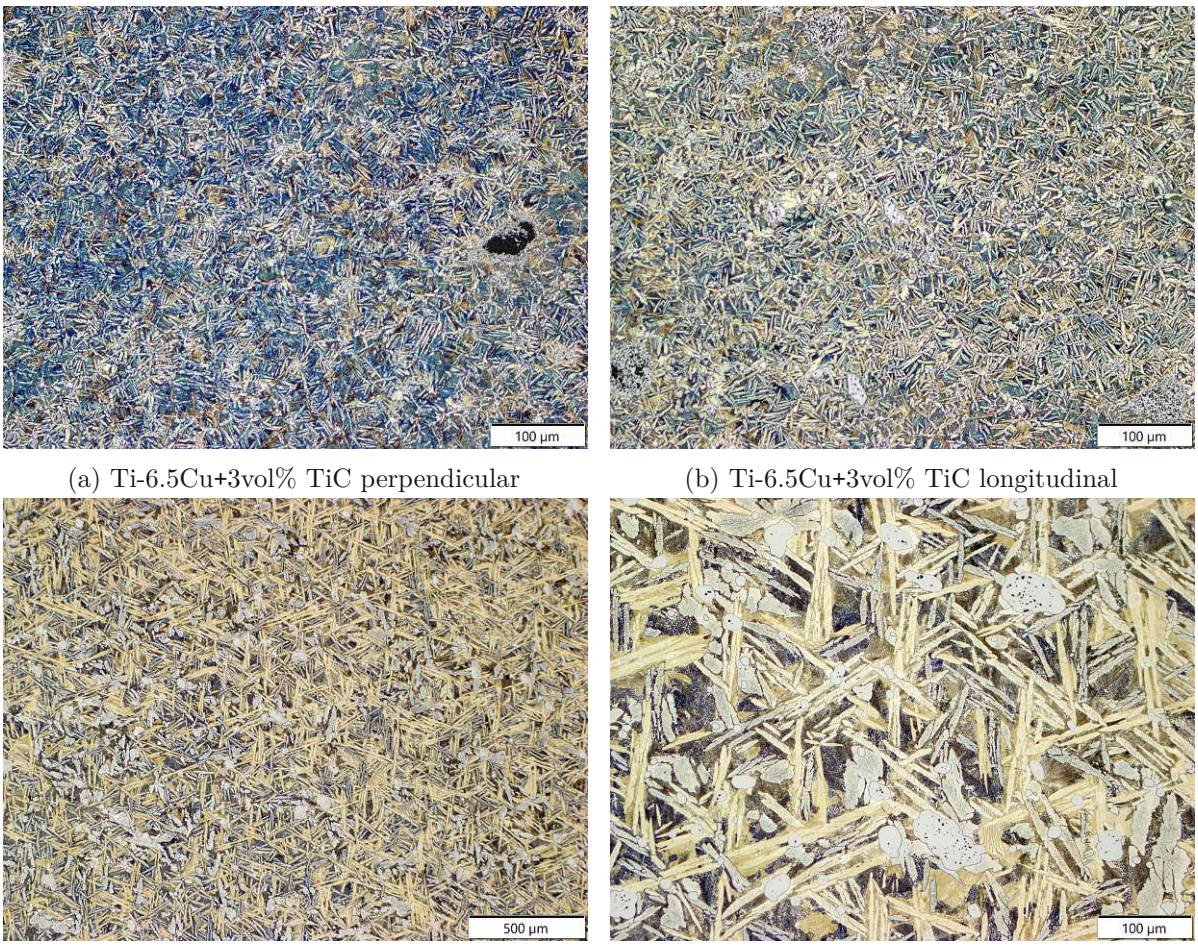

(a) Ti-6.5Cu+3vol% TiC perpendicular

(b) Ti-6.5Cu+3vol% TiC longitudinal

(c) Ti-6.5Cu+3vol% TiC 1000 °C/90h perpendicular

(d) Ti-6.5Cu+3vol% TiC 1000 °C/90h perpendicular

Figure 26: Optical microscopy of the etched Ti-6.5Cu+3vol% TiC as-extruded samples (a-b) and the heat-treated samples (c-d)

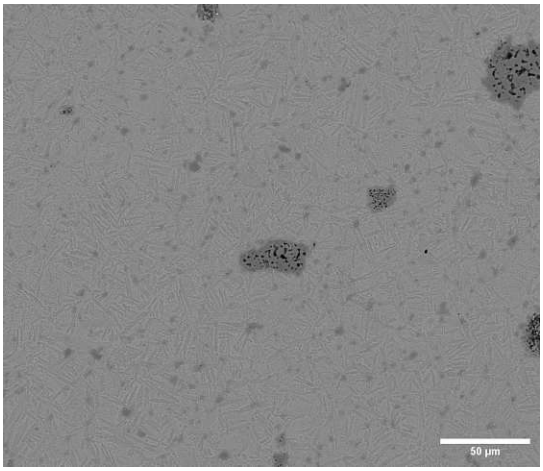

(a) Ti-6.5Cu+3vol% TiC perpendicular

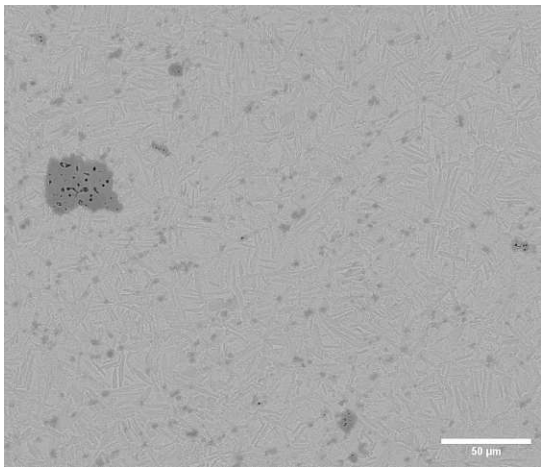

(b) Ti-6.5Cu+3vol% TiC longitudinal

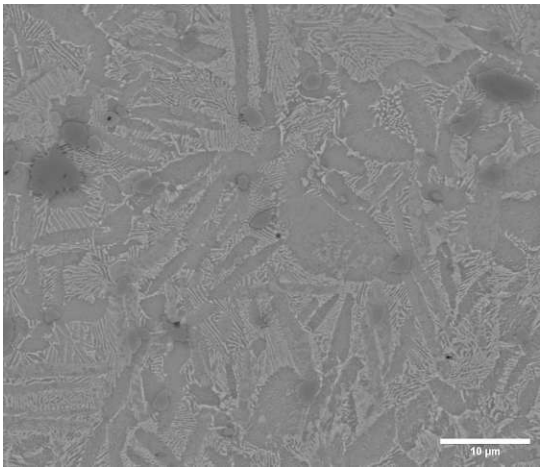

(c) Ti-6.5Cu+3vol% TiC perpendicular

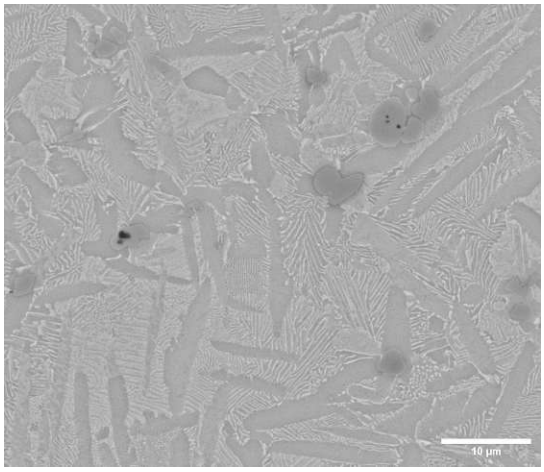

(d) Ti-6.5Cu+3vol% TiC longitudinal

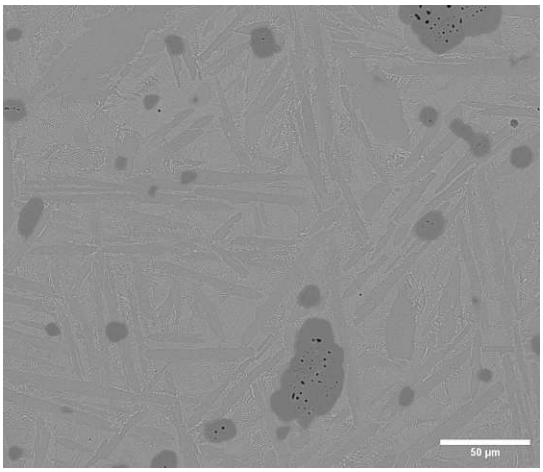

(e) Ti-6.5Cu+3vol% TiC 1000 °C/90h perpendicular

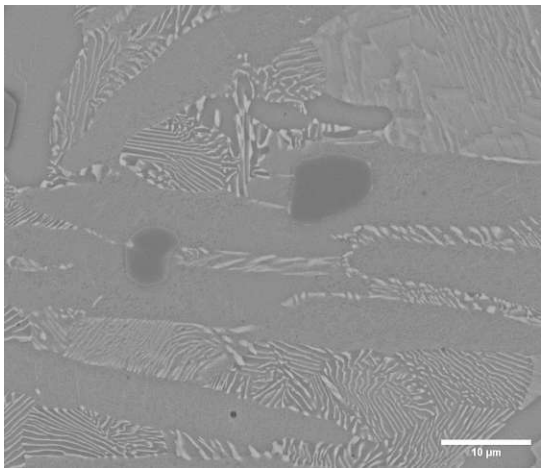

(f) Ti-6.5Cu+3vol% TiC 1000 °C/90h perpendicular

Figure 27: SEM images of the etched Ti-6.5Cu+3vol% TiC as-extruded samples (a-d) and the heat-treated samples (e-f)

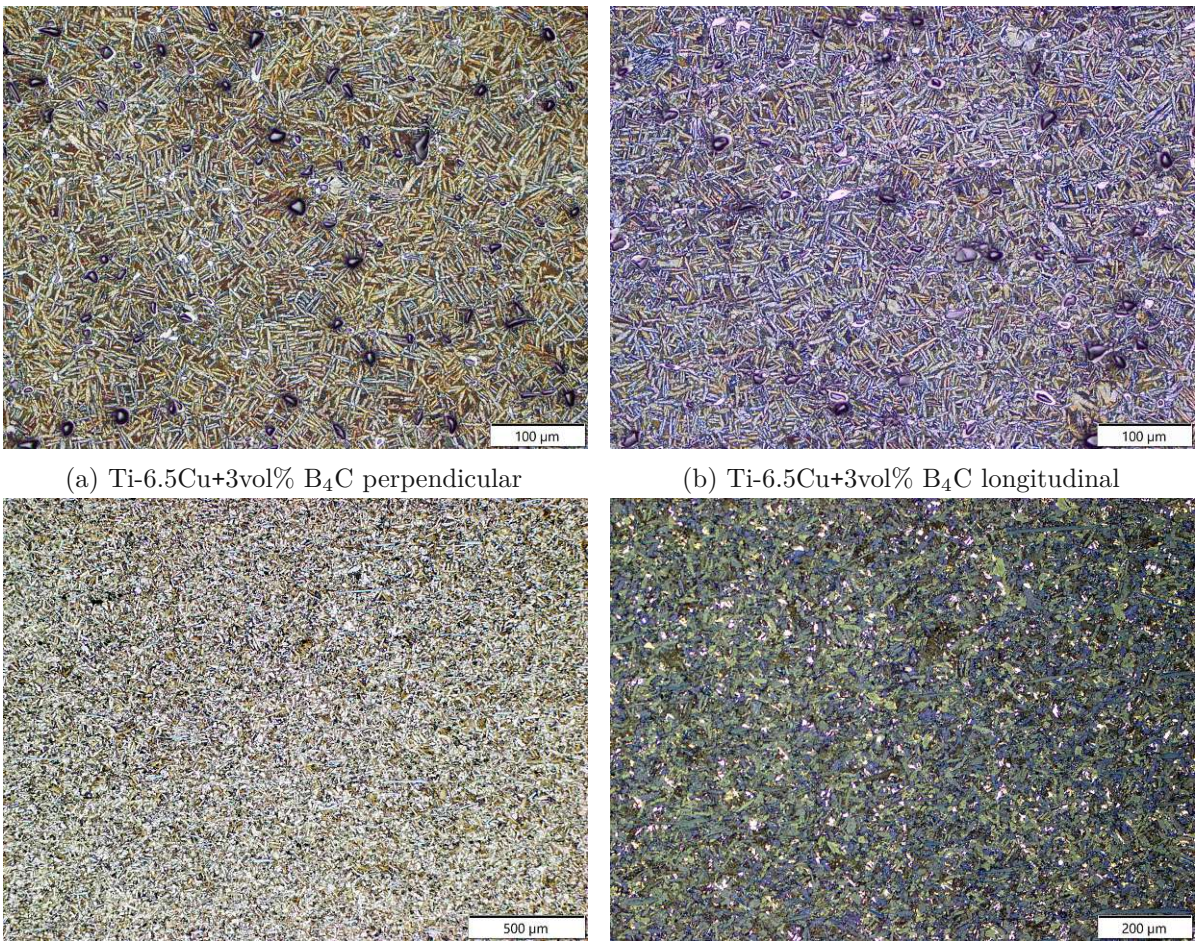

(a) Ti-6.5Cu+3vol% B_4C perpendicular

(b) Ti-6.5Cu+3vol% B_4C longitudinal

(c) Ti-6.5Cu+3vol% B_4C 1000 °C/90h perpendicular

(d) Ti-6.5Cu+3vol% B_4C 1000 °C/90h perpendicular

Figure 28: Optical microscopy of the etched Ti-6.5Cu+3vol% B_4C as-extruded samples (a-b) and the heat-treated samples (c-d)

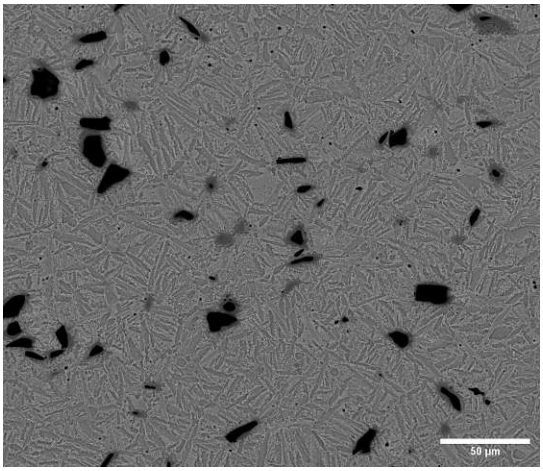

(a) Ti-6.5Cu+3vol% B_4C perpendicular

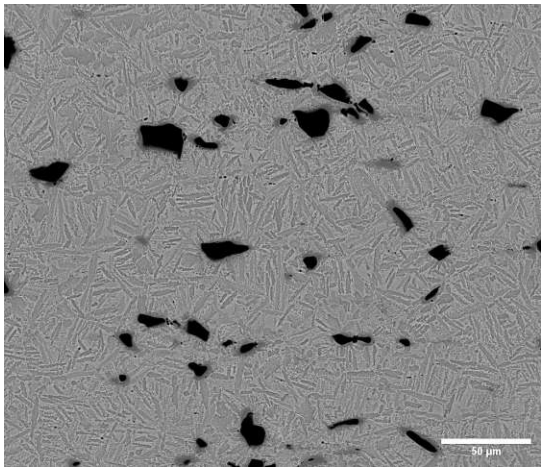

(b) Ti-6.5Cu+3vol% B_4C longitudinal

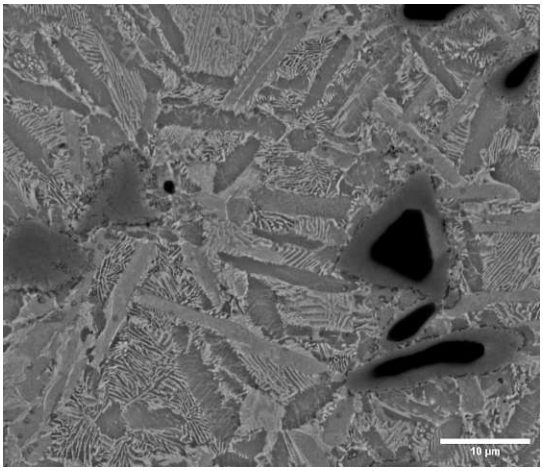

(c) Ti-6.5Cu+3vol% B_4C perpendicular

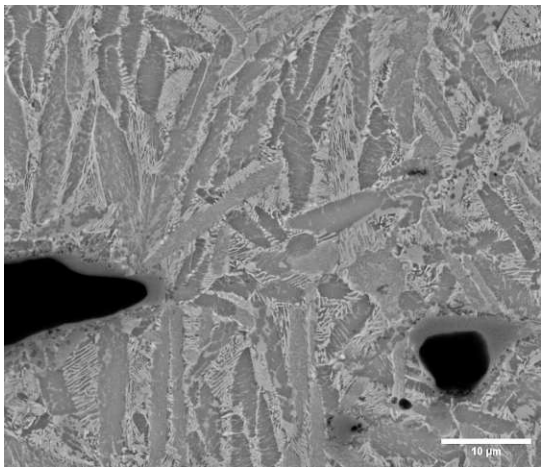

(d) Ti-6.5Cu+3vol% B_4C longitudinal

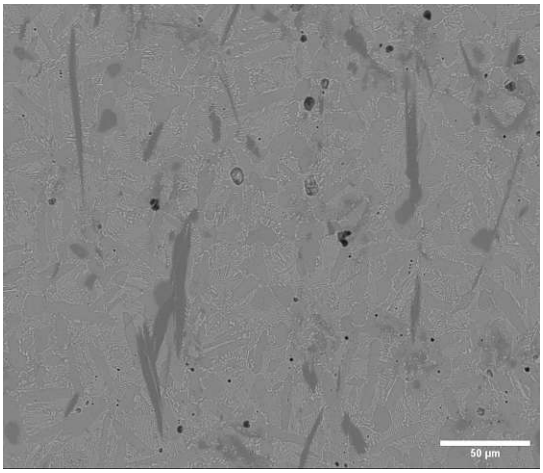

(e) Ti-6.5Cu+3vol% B_4C 1000 °C/90h perpendicular

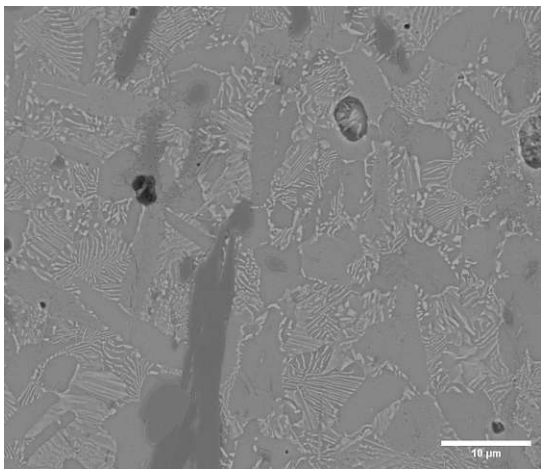

(f) Ti-6.5Cu+3vol% B_4C 1000 °C/90h perpendicular

Figure 29: SEM images of the etched Ti-6.5Cu+3vol% B_4C as-extruded samples (a-d) and the heat-treated samples (e-f)

4.1.4 Ti-6.4Ni-2Fe systems

The binary Ti-Ni system promises good strength and grain refinement due to the addition of Ni. By adding Fe, more grain refinement is to be expected as the redistribution of Fe-atoms seem to be the rate-gouverning process regarding the α-precipitation [28, 45]. However, extrusion results in a non-ideal fractured rod (Figure 30). Figures 31 a-b and 32 c-d show the as-extruded Ti-6.4Ni-2Fe systems. The microstructure can be divided into two regions. Firstly, α-Ti with interstitial α-Ti/Ti_2Ni eutecoid, secondly, undissolved Fe particles. After heat treatment, no residual Fe particles are found and grain growth is visible (Figure 31 c-d and 32 e-f). Due to the non-ideal rod, an alternative approach was chosen. Ti-6.4Ni-2Fe powder was pressed and sintered. The sintered material is then cut and transferred into the steel capsule, the remaining spaces is filled with powder. The aim is to achieve a higher filling density and to extrude more material. However, the result is a similarly cracked and tapered rod (Figure 33). Looking at the microstructure of the presintered and as-extruded Ti-6.4Ni-2Fe system in Figure 34 a-b and 35 a-d, there is no visible difference to the pure powder extruded system. The addition of the elemental powder, namely Fe and Ni, again results in undissolved Fe particles. These particles are not completely dissolved after heat treatment, as the powder may be localised in the interstitial spaces of the sintered material, leading to a higher local iron concentration which prevents further diffusion (Figure 34 c-d and 35 e-f). Figure 36 shows some additional undissolved Fe particles. The EDS line analysis shows an enrichment of nickel around the iron particle. Surprisingly, heat treatment of the pre-sintered sample results in a change in microstructure towards globular grains, whereas this is not the case for the pure powder based samples. The addition of 3vol% TiC results in a finer microstructure, but the Fe particles remain undissolved after extrusion (Figure 37 a-b and 38 c-d). The heat treatment results in grain growth and development of the eutectoid structure, leaving the TiC particles (Figure 37 c-d and 38 e-f). An analogous microstructure is obtained by the addition of 3vol% B_4C (Figure 39 and 40). The main difference is the formation of TiC and TiB due to the heat treatment.

Figure 30: Ti-6.4Ni-2Fe rod with ruptured areas

(a) Ti-6.4Ni-2Fe perpendicular

(b) Ti-6.4Ni-2Fe longitudinal

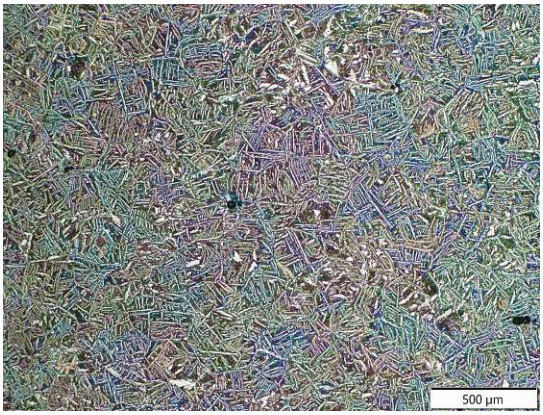

(c) Ti-6.4Ni-2Fe 1000 °C/90h perpendicular

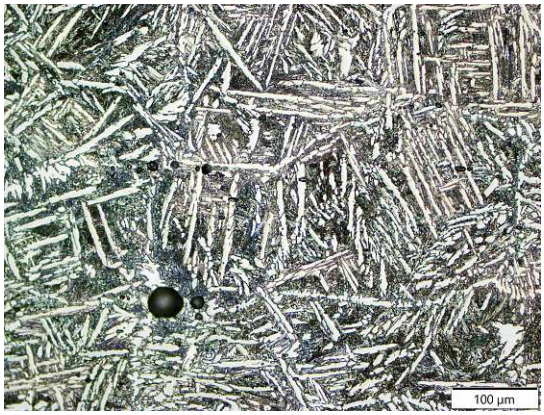

(d) Ti-6.4Ni-2Fe 1000 °C/90h perpendicular

Figure 31: Optical microscopy of the etched Ti-6.4Ni-2Fe as-extruded samples (a-b) and the heat-treated samples (c-d)

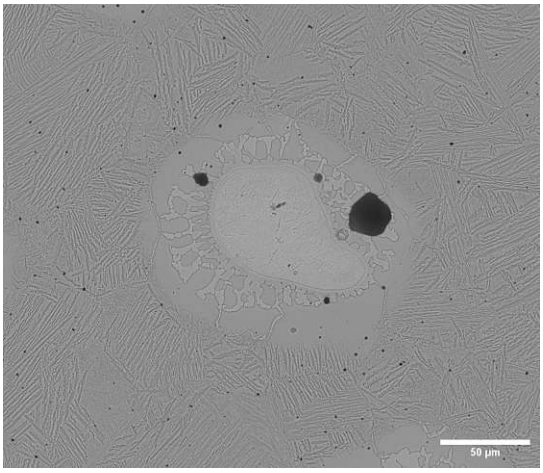

(a) Ti-6.4Ni-2Fe Fe-particle perpendicular

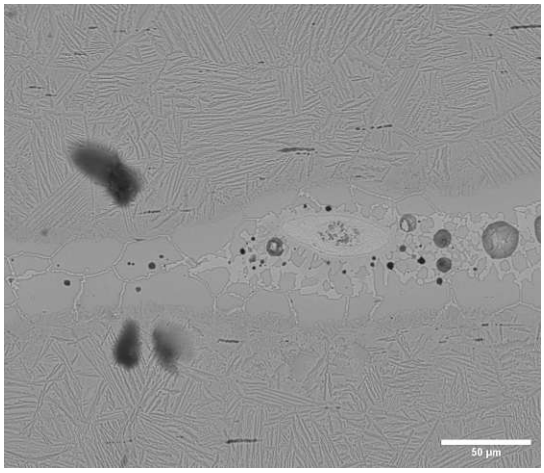

(b) Ti-6.4Ni-2Fe Fe-particle longitudinal

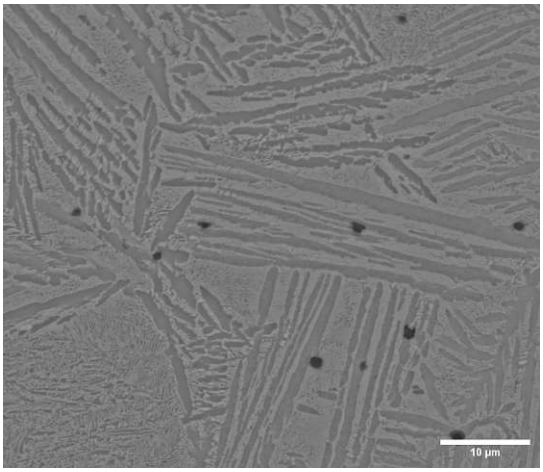

(c) Ti-6.4Ni-2Fe perpendicular

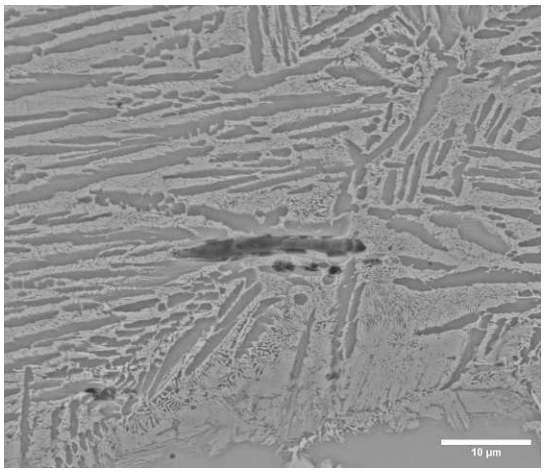

(d) Ti-6.4Ni-2Fe longitudinal

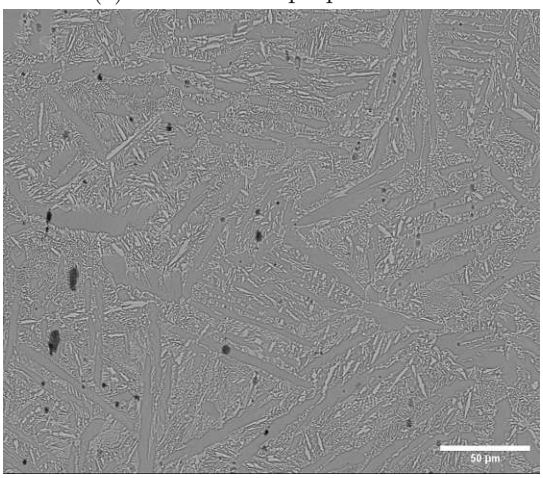

(e) Ti-6.4Ni-2Fe 1000 °C/90h perpendicular

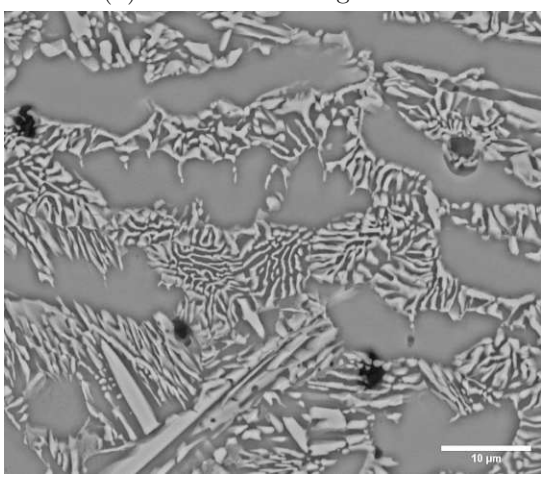

(f) Ti-6.4Ni-2Fe 1000 °C/90h perpendicular

Figure 32: SEM images of the etched Ti-6.4Ni-2Fe as-extruded samples (a-d), and the heat-treated samples (e-f)

Figure 33: Presintered Ti-6.4Ni-2Fe rod with ruptured areas

(a) Ti-6.4Ni-2Fe presintered perpendicular

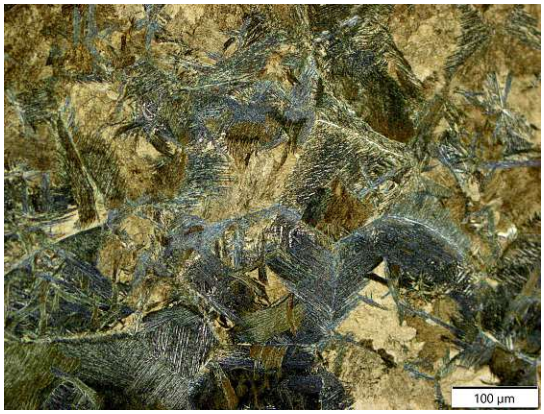

(b) Ti-6.4Ni-2Fe presintered longitudinal

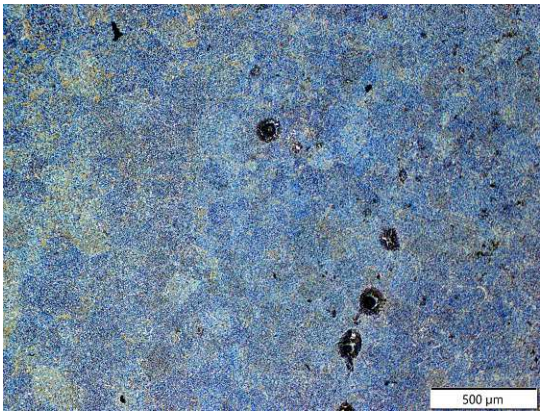

(c) Ti-6.4Ni-2Fe presintered 1000 °C/90h perpendicular

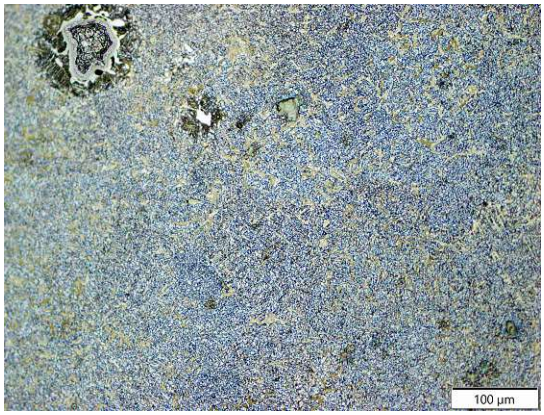

(d) Ti-6.4Ni-2Fe presintered 1000 °C/90h perpendicular

Figure 34: Optical microscopy of the etched presintered Ti-6.4Ni-2Fe as-extruded samples (a-b) and the heat-treated samples (c-d)

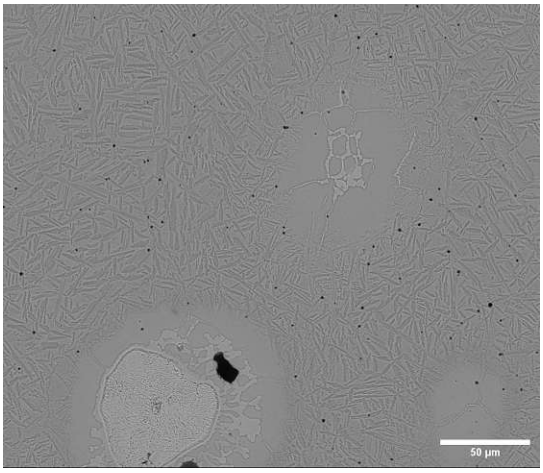

(a) Ti-6.4Ni-2Fe presintered Fe particle perpendicular

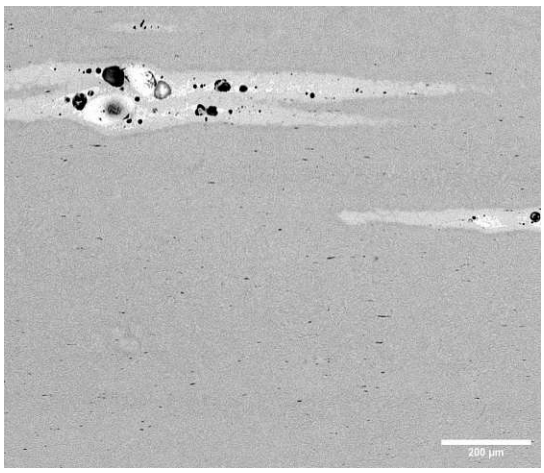

(b) Ti-6.4Ni-2Fe presintered Fe particle longitudinal

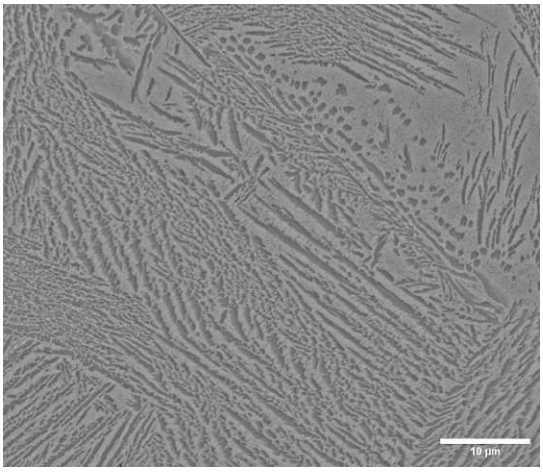

(c) Ti-6.4Ni-2Fe presintered perpendicular

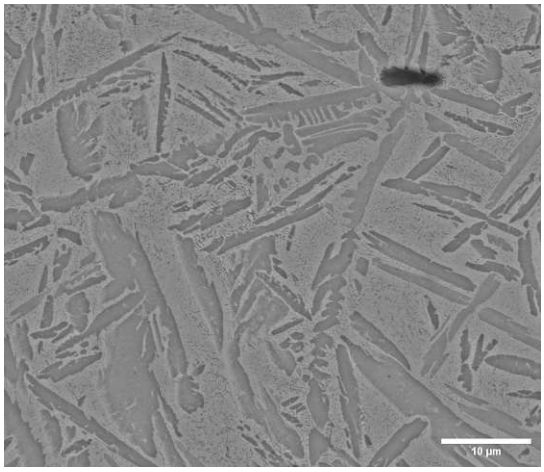

(d) Ti-6.4Ni-2Fe presintered longitudinal

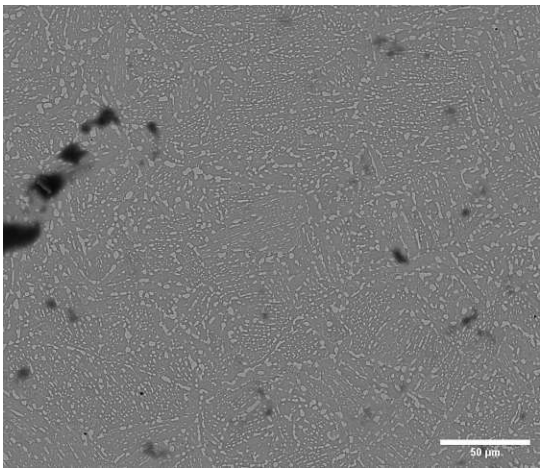

(e) Ti-6.4Ni-2Fe presintered 1000 °C/90h perpendicular

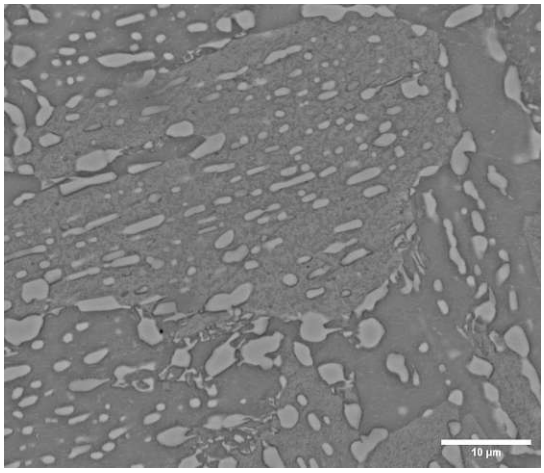

(f) Ti-6.4Ni-2Fe presintered 1000 °C/90h perpendicular

Figure 35: SEM images of the etched presintered Ti-6.4Ni-2Fe as-extruded samples (a-d), and the heat-treated samples (e-f)

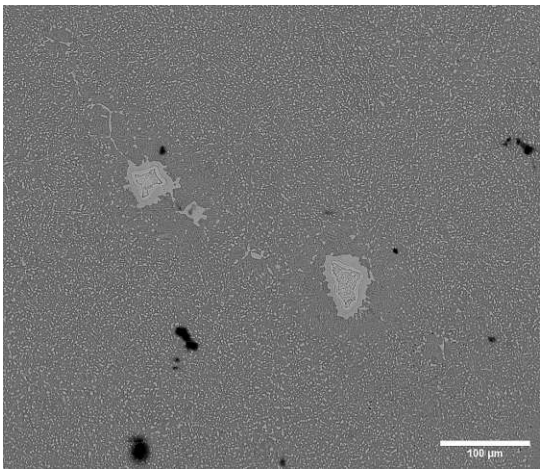

(a) Ti-6.4Ni-2Fe presintered 1000 °C/90h

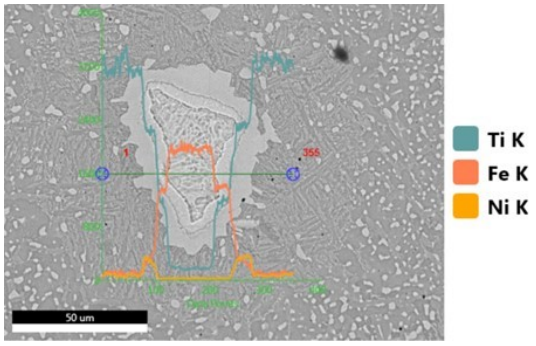

(b) Ti-6.4Ni-2Fe presintered EDS line profile

Figure 36: SEM images of the heat-treated presintered Ti-6.4Ni-2Fe and EDS line profile of a Fe-particle

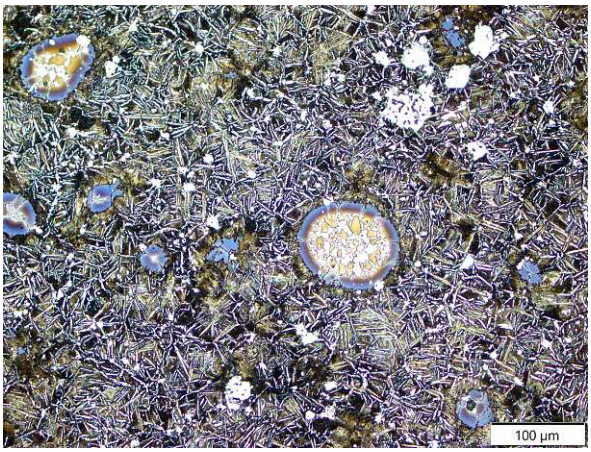

(a) Ti-6.4Ni-2Fe+3vol% TiC perpendicular

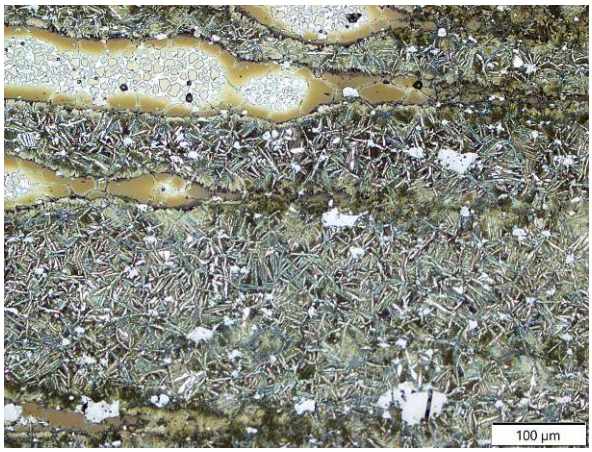

(b) Ti-6.4Ni-2Fe+3vol% TiC longitudinal

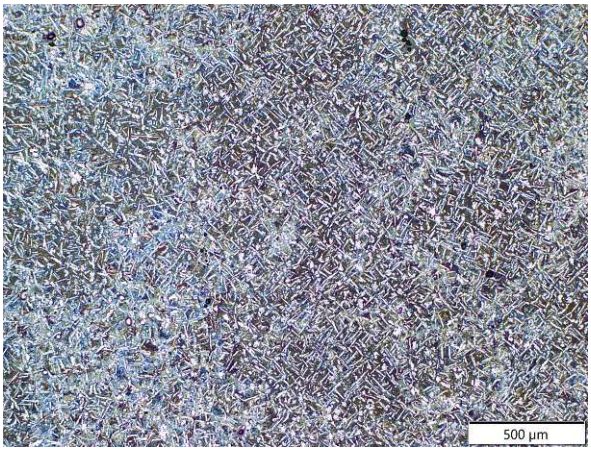

(c) Ti-6.4Ni-2Fe+3vol% TiC 1000 °C/90h perpendicular

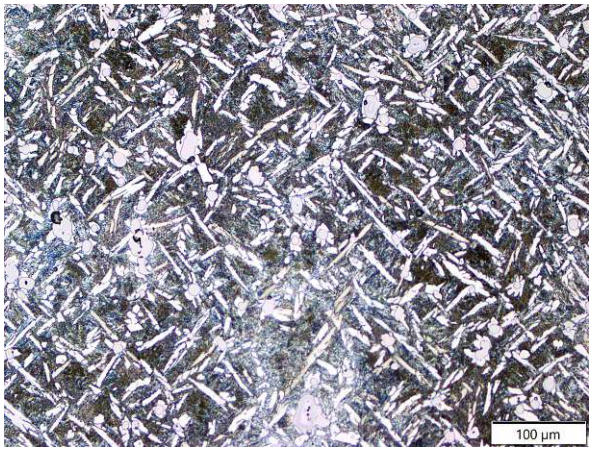

(d) Ti-6.4Ni-2Fe+3vol% TiC 1000 °C/90h perpendicular

Figure 37: Optical microscopy of the etched Ti-6.4Ni-2Fe+3vol% TiC as-extruded samples (a-b) and the heat-treated samples (c-d)

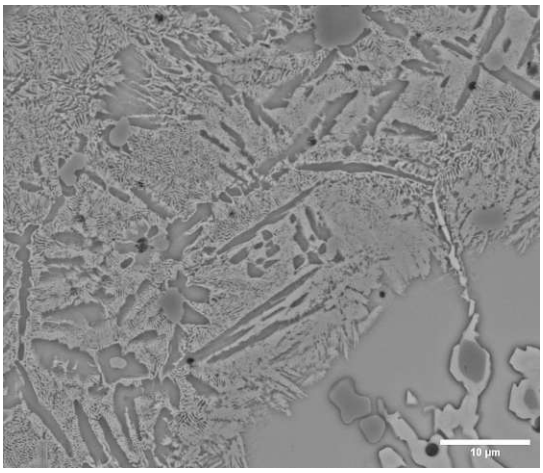

(a) Ti-6.4Ni-2Fe+3vol% TiC perpendicular

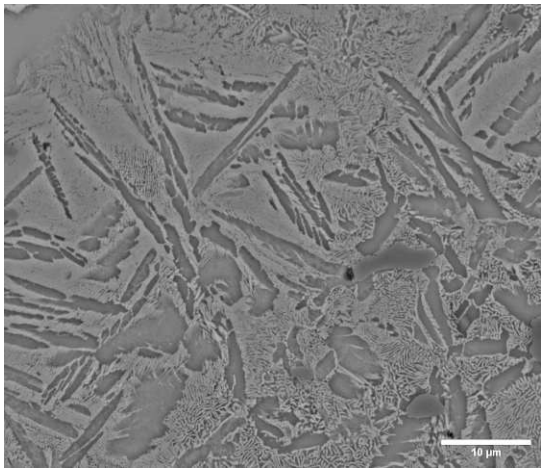

(b) Ti-6.4Ni-2Fe+3vol% TiC longitudinal

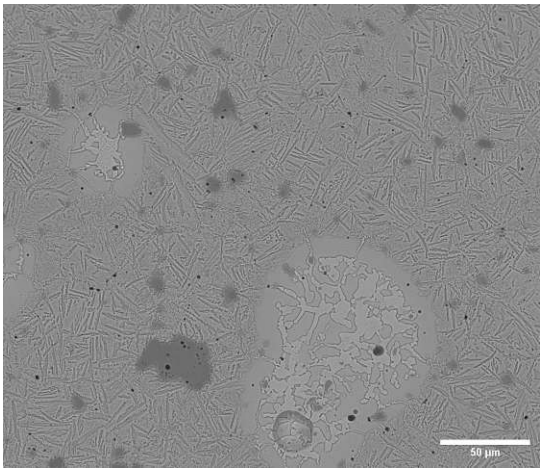

(c) Ti-6.4Ni-2Fe+3vol% TiC Fe particle perpendicular

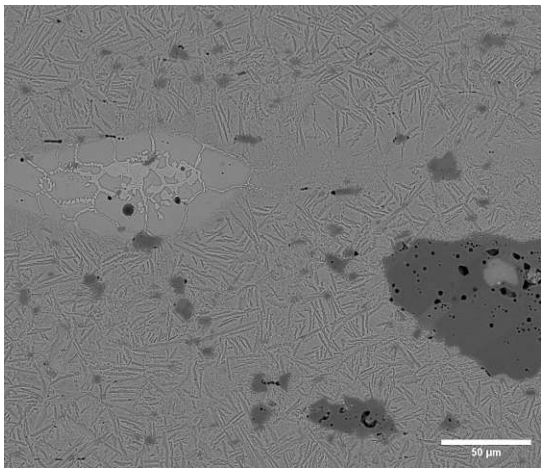

(d) Ti-6.4Ni-2Fe+3vol% TiC Fe particle longitudinal

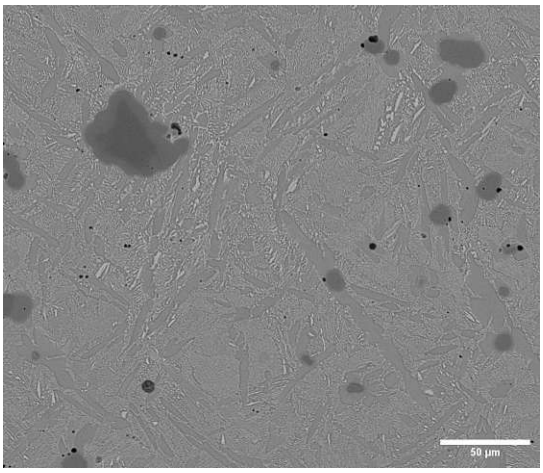

(e) Ti-6.4Ni-2Fe+3vol% TiC 1000 °C/90h perpendicular

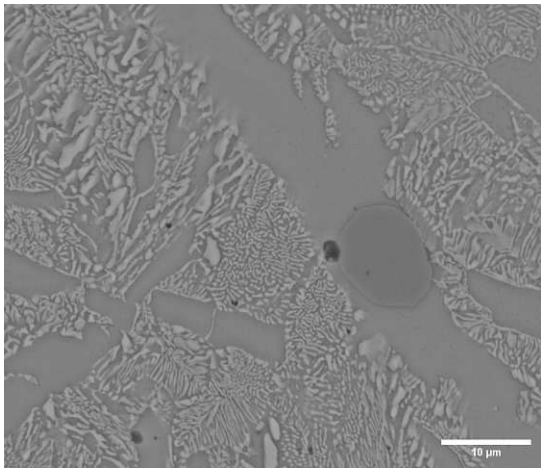

(f) Ti-6.4Ni-2Fe+3vol% TiC 1000 °C/90h perpendicular

Figure 38: SEM images of the etched Ti-6.4Ni-2Fe+3vol% TiC as-extruded samples (a-d), and the heat-treated samples (e-f)

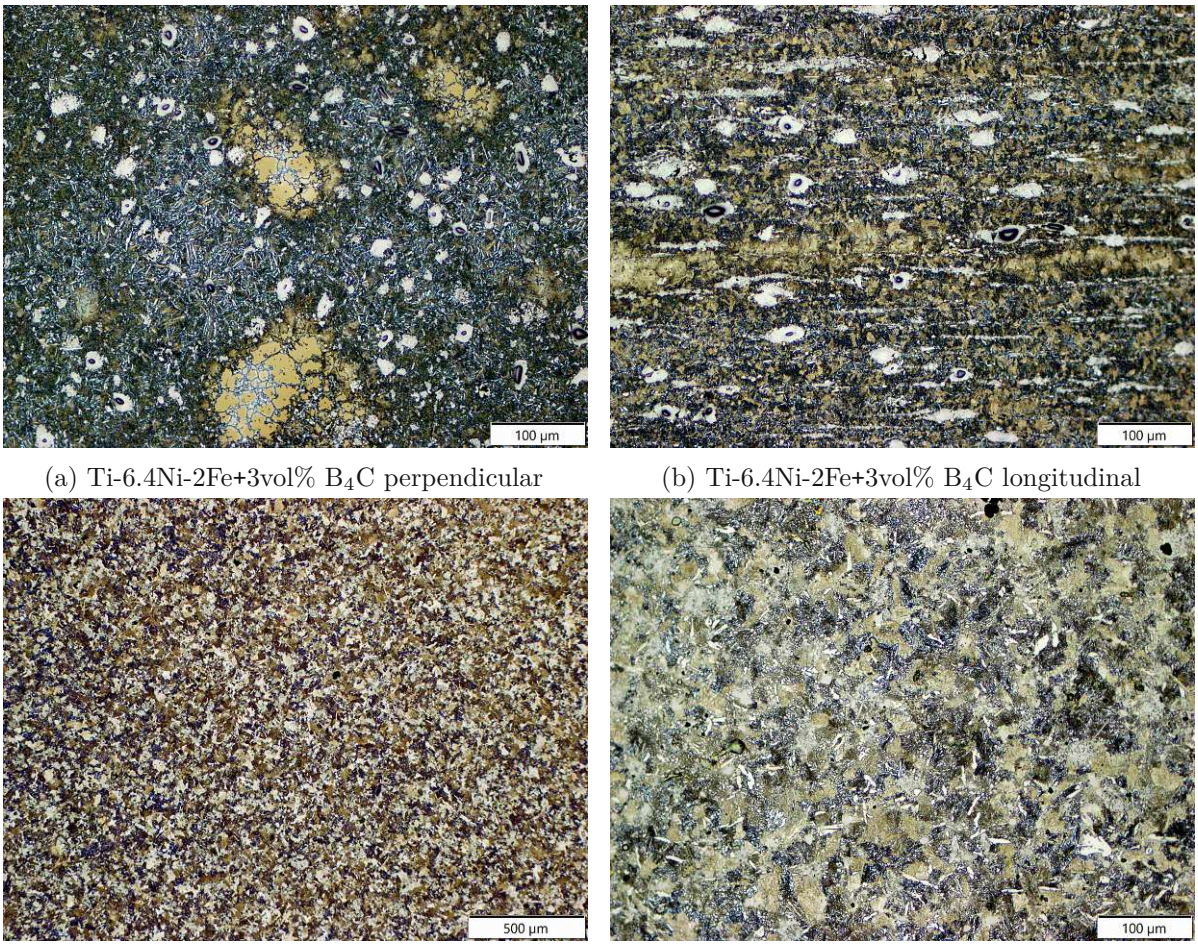

(a) Ti-6.4Ni-2Fe+3vol% B_4C perpendicular

(b) Ti-6.4Ni-2Fe+3vol% B_4C longitudinal

(c) Ti-6.4Ni-2Fe+3vol% B_4C 1000 °C/90h perpendicular

(d) Ti-6.4Ni-2Fe+3vol% B_4C 1000 °C/90h perpendicular

Figure 39: Optical microscopy of the etched Ti-6.4Ni-2Fe+3vol% B_4C as-extruded samples (a-b) and the heat-treated samples (c-d)

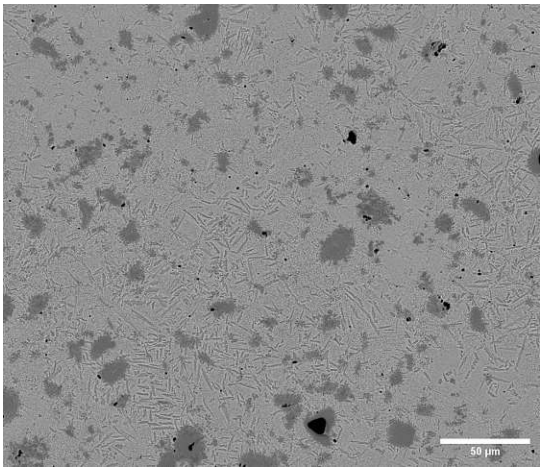

(a) Ti-6.4Ni-2Fe+3vol% B_4C perpendicular

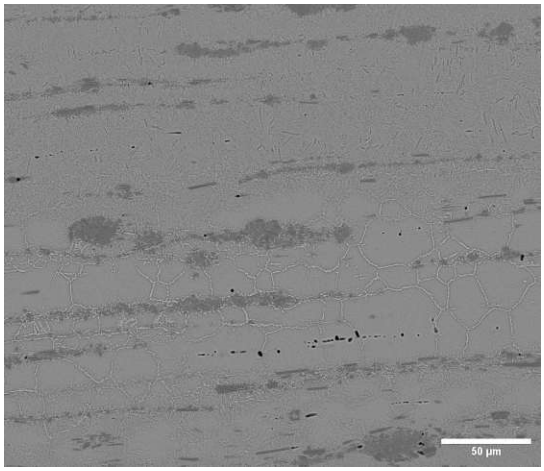

(b) Ti-6.4Ni-2Fe+3vol% B_4C longitudinal

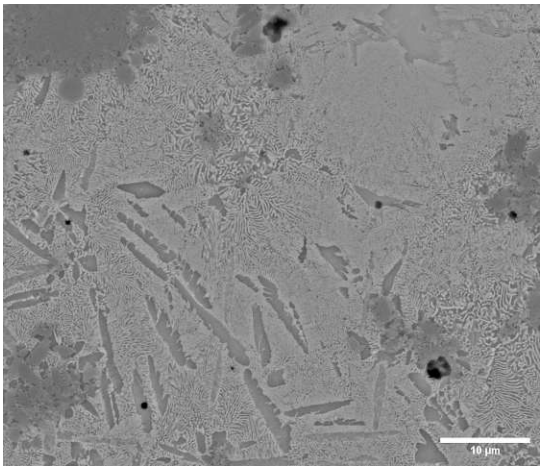

(c) Ti-6.4Ni-2Fe+3vol% B_4C perpendicular

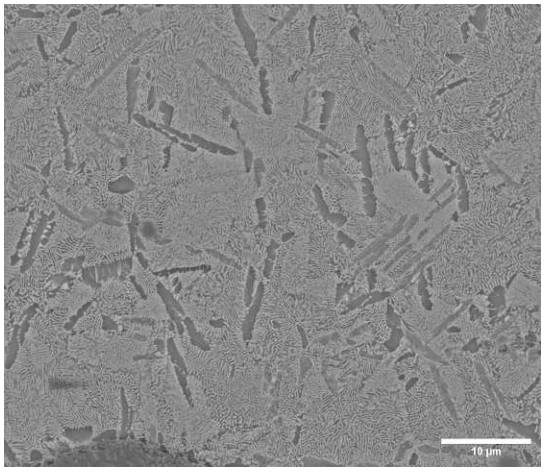

(d) Ti-6.4Ni-2Fe+3vol% B_4C longitudinal

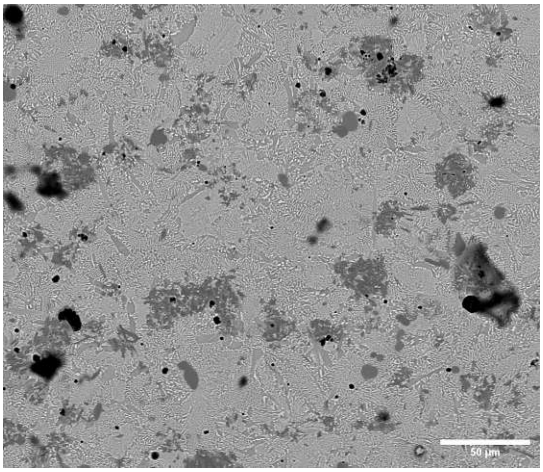

(e) Ti-6.4Ni-2Fe+3vol% B_4C 1000 °C/90h perpendicular

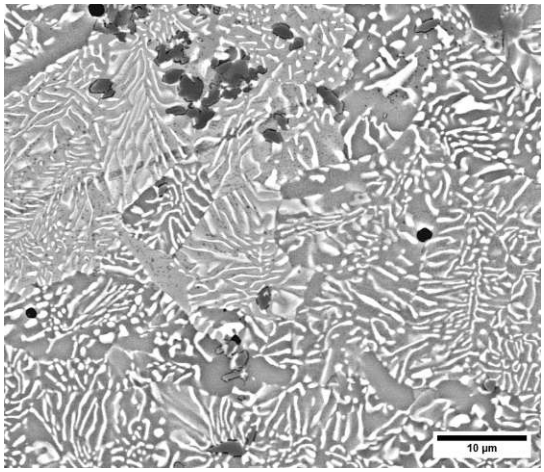

(f) Ti-6.4Ni-2Fe+3vol% B_4C 1000 °C/90h perpendicular

Figure 40: SEM images of the etched Ti-6.4Ni-2Fe+3vol% B_4C as-extruded samples (a-d), and the heat-treated samples (e-f)

4.1.5 Ti-6.4Ni-2Cr systems

In the Ti-6.4Ni-2Cr ternary the Cr should act as an additional grain refiner [27]. Theoretically, a three-phase system consisting of α-Ti, Ti_2Ni and Ti_2Cr should be obtained. The microstructure of the as-extruded Ti-6.4Ni-2Cr sample is shown in Figure 41 a-b and 42 a-d. Similar to the Ti-6.4Ni-2Fe alloy, a basket weave structure is obtained. Only two phases are distinguishable in the SEM images, the darker α-Ti phase and the brighter one consisting of Ti, Ni and Cr. In addition, the Cr particles are not dissolved in the extrusion process. After heat treatment, no residual Cr particles are found and grain growth has taken place (Figure 41 c-d and 42 e-f). With the addition of 3vol% TiC a grain refinement is observed. As before, undissolved Cr particles are found (Figure 43 a-b and 44 a-d). The heat-treated sample shows some grain growth and no residual Cr particles. The TiC particles remain (Figure 43 c-d and 44 e-f). The addition of 3 vol% B_4C results in an even finer microstructure (Figure 45 a-b and 46 a-d). In the longitudinal direction there are smudged B_4C particles. Undissolved Cr particles remain. The heat treatment causes a structural transformation resulting in equiaxed α-Ti and almost globular intermetallic phases. No needle-like titanium borides are observed, but a fraying of the B_4C particles (Figure 45 c-d and 46 e-f).

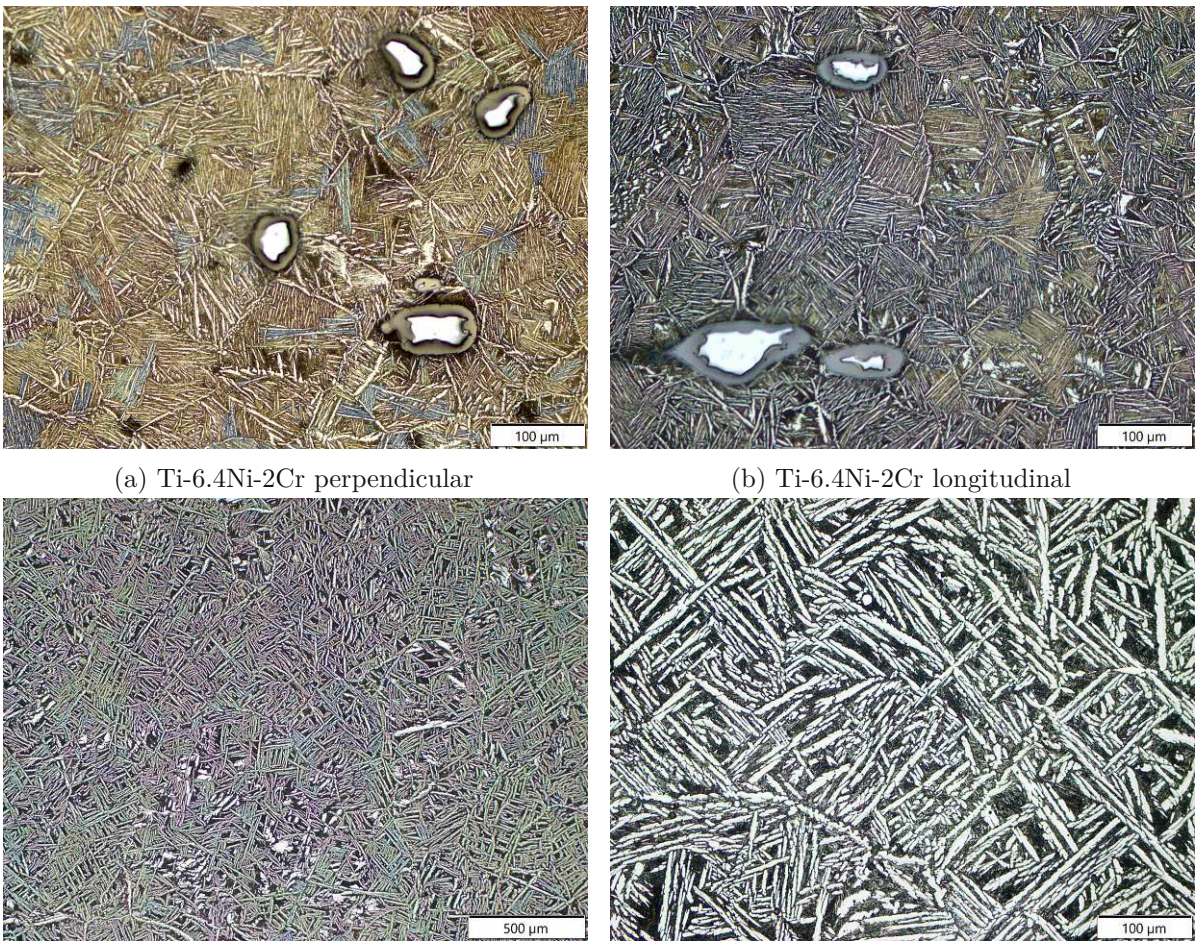

(a) Ti-6.4Ni-2Cr perpendicular

(b) Ti-6.4Ni-2Cr longitudinal

(c) Ti-6.4Ni-2Cr 1000 °C/90h perpendicular

(d) Ti-6.4Ni-2Cr 1000 °C/90h perpendicular

Figure 41: Optical microscopy of the etched Ti-6.4Ni-2Cr as-extruded samples (a-b) and the heat-treated samples (c-d)

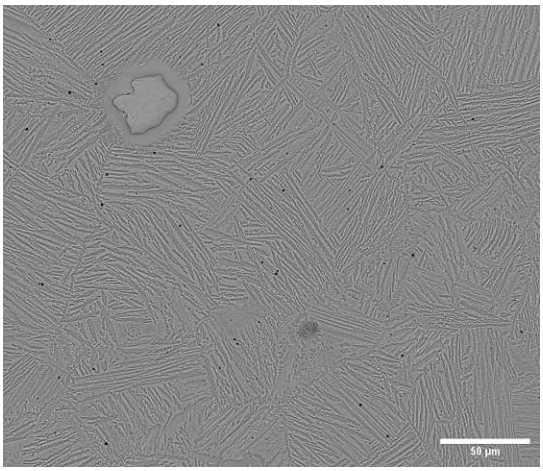

(a) Ti-6.4Ni-2Cr with Cr-particle perpendicular

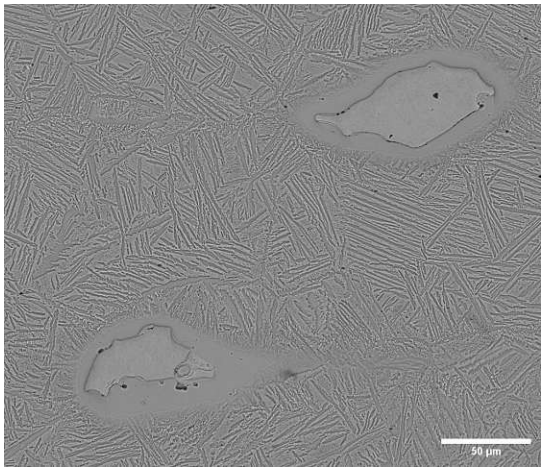

(b) Ti-6.4Ni-2Cr with Cr-particles longitudinal

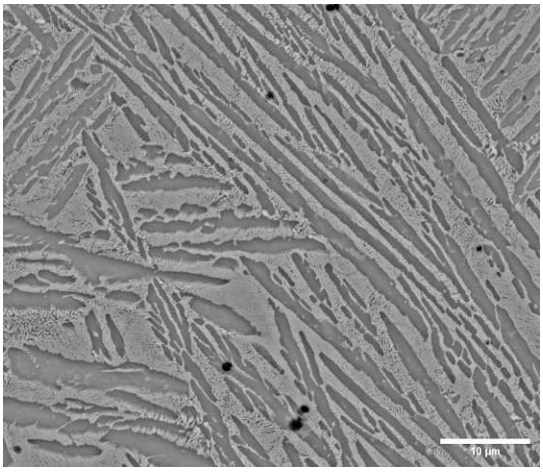

(c) Ti-6.4Ni-2Cr perpendicular

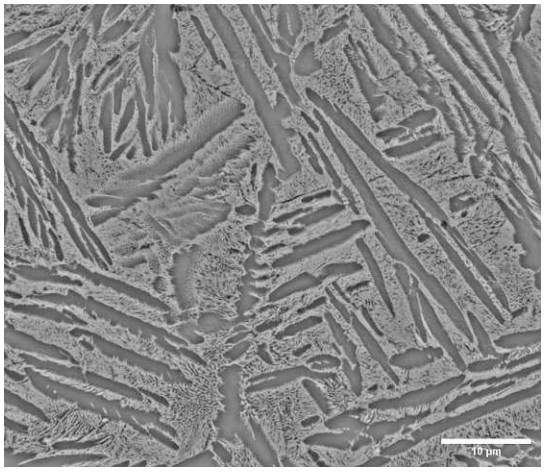

(d) Ti-6.4Ni-2Cr longitudinal

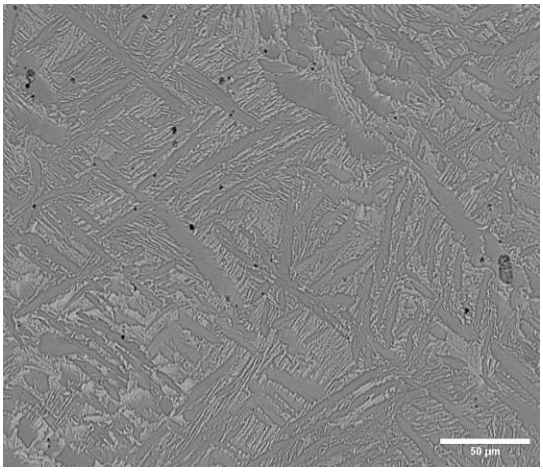

(e) Ti-6.4Ni-2Cr 1000 °C/90h perpendicular

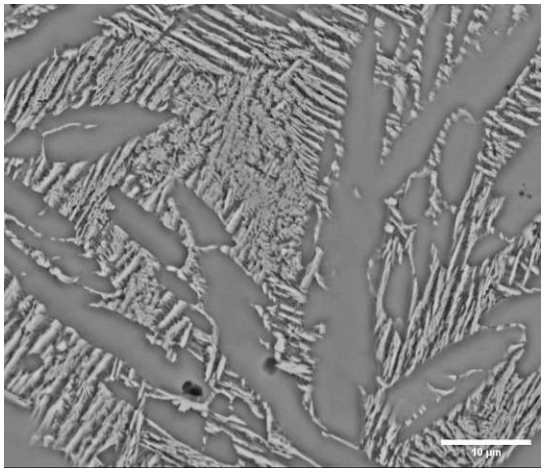

(f) Ti-6.4Ni-2Cr 1000 °C/90h perpendicular

Figure 42: SEM images of the etched Ti-6.4Ni-2Cr as-extruded samples (a-d), and the heat-treated samples (e-f)

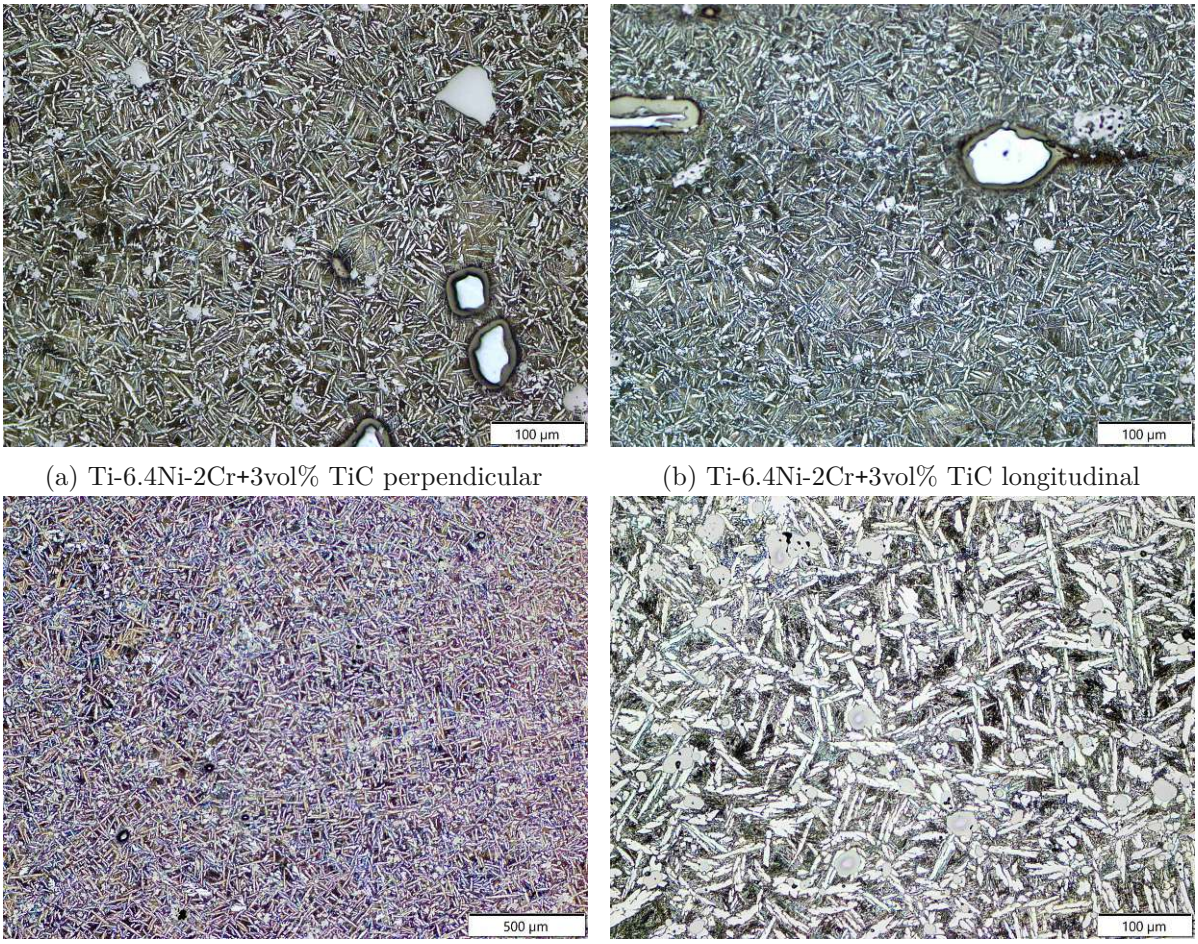

(a) Ti-6.4Ni-2Cr+3vol% TiC perpendicular

(b) Ti-6.4Ni-2Cr+3vol% TiC longitudinal

(c) Ti-6.4Ni-2Cr+3vol% TiC 1000 °C/90h perpendicular

(d) Ti-6.4Ni-2Cr+3vol% TiC 1000 °C/90h perpendicular

Figure 43: Optical microscopy of the etched Ti-6.4Ni-2Cr+3vol% TiC as-extruded samples (a-b) and the heat-treated samples (c-d)

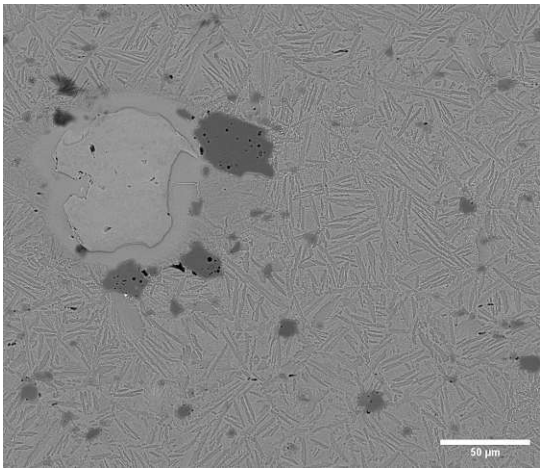

(a) Ti-6.4Ni-2Cr+3vol% TiC with Cr-particle perpendicular

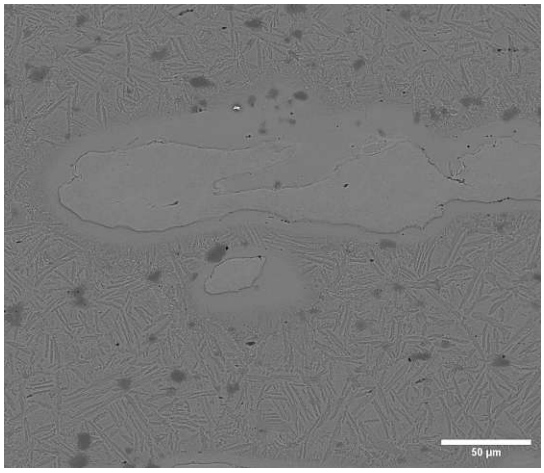

(b) Ti-6.4Ni-2Cr+3vol% TiC with Cr-particle longitudinal

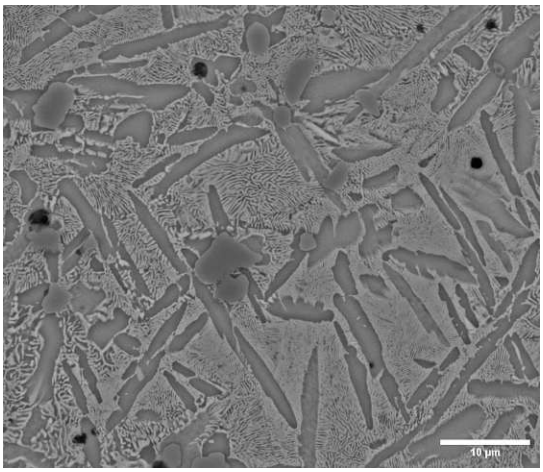

(c) Ti-6.4Ni-2Cr+3vol% TiC perpendicular

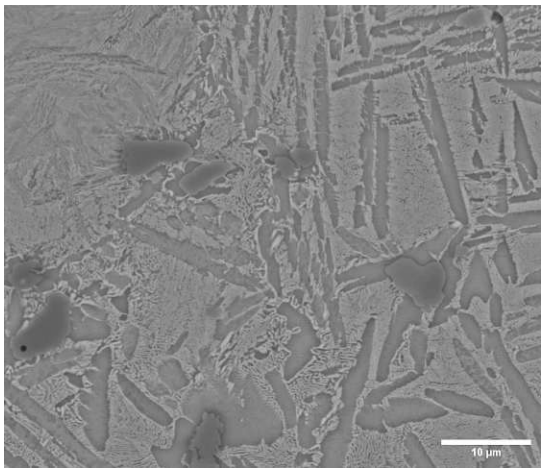

(d) Ti-6.4Ni-2Cr+3vol% TiC longitudinal

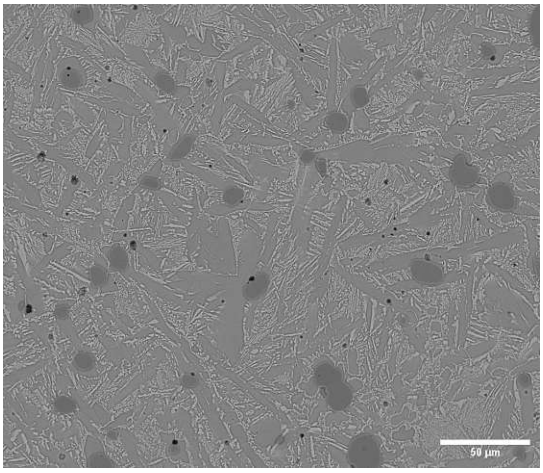

(e) Ti-6.4Ni-2Cr+3vol% TiC 1000 °C/90h perpendicular

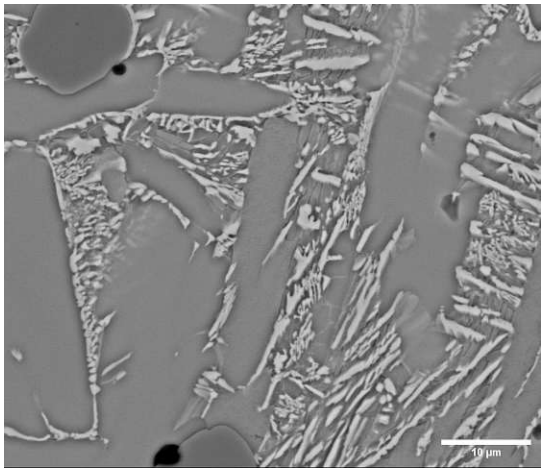

(f) Ti-6.4Ni-2Cr+3vol% TiC 1000 °C/90h perpendicular

Figure 44: SEM images of the etched Ti-6.4Ni-2Cr+3vol% TiC as-extruded samples (a-b), and the heat-treated samples (c-d)

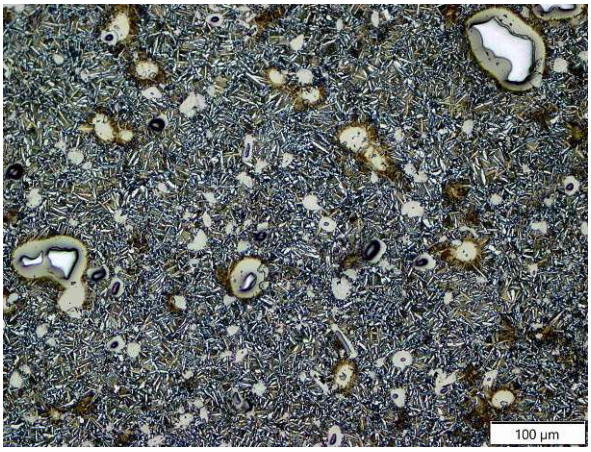

(a) Ti-6.4Ni-2Cr+3vol% B_4C perpendicular

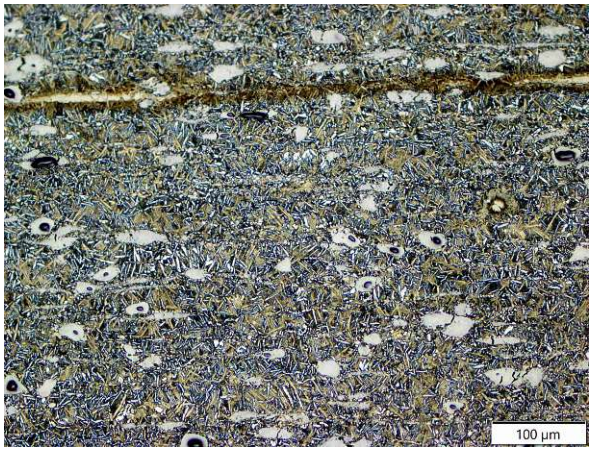

(b) Ti-6.4Ni-2Cr+3vol% B_4C longitudinal

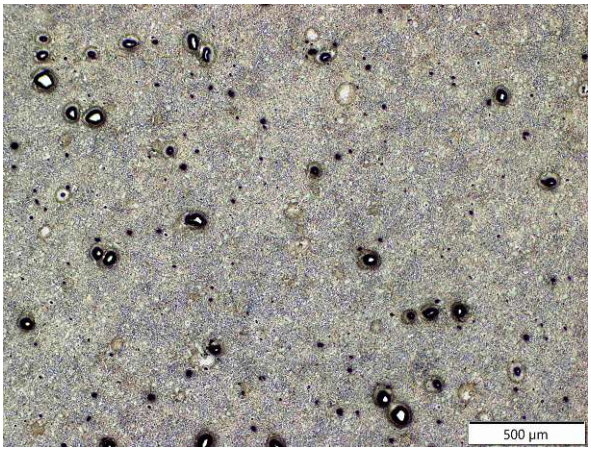

(c) Ti-6.4Ni-2Cr+3vol% B_4C 1000 °C/90h perpendicular

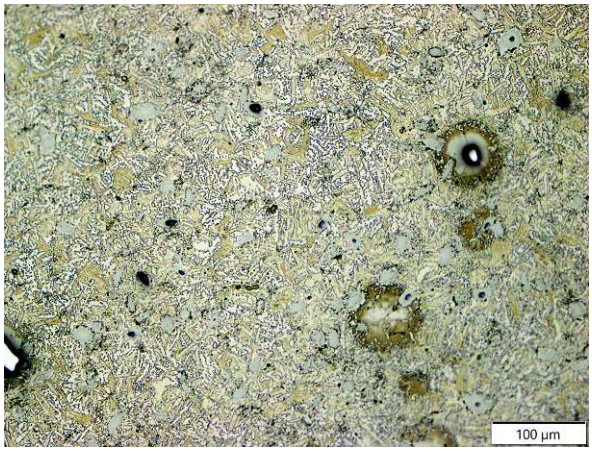

(d) Ti-6.4Ni-2Cr+3vol% B_4C 1000 °C/90h perpendicular

Figure 45: Optical microscopy of the etched Ti-6.4Ni-2Cr+3vol% B_4C as-extruded samples (a-b) and the heat-treated samples (c-d)

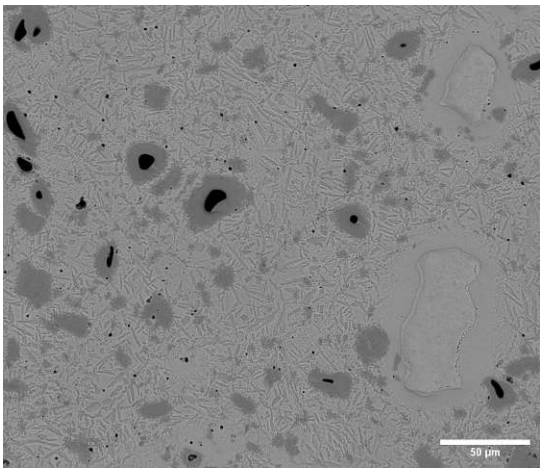

(a) Ti-6.4Ni-2Cr+3vol% B_4C perpendicular

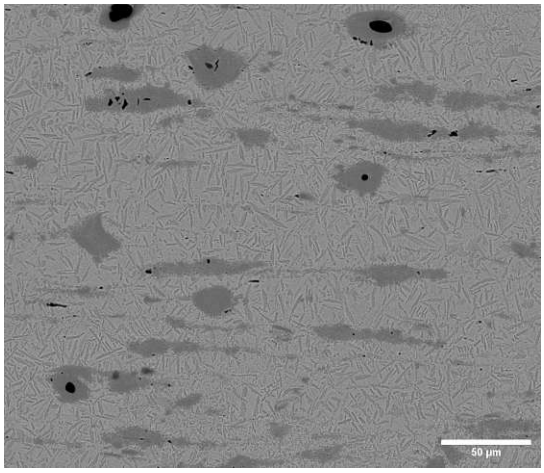

(b) Ti-6.4Ni-2Cr+3vol% B_4C longitudinal

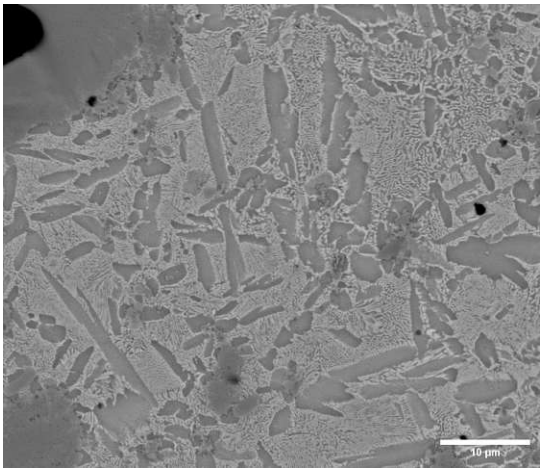

(c) Ti-6.4Ni-2Cr+3vol% B_4C perpendicular

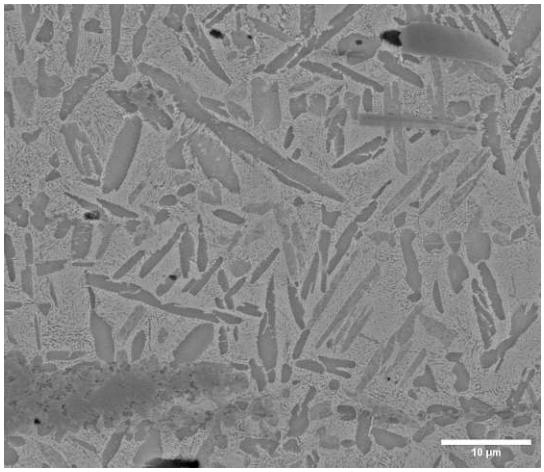

(d) Ti-6.4Ni-2Cr+3vol% B_4C longitudinal

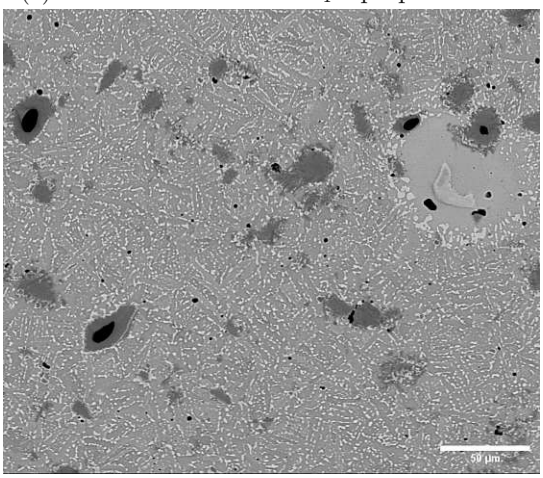

(e) Ti-6.4Ni-2Cr+3vol% B_4C 1000 °C/90h perpendicular

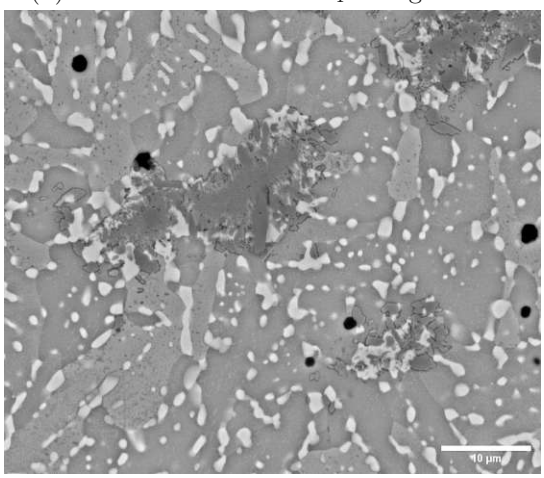

(f) Ti-6.4Ni-2Cr+3vol% B_4C 1000 °C/90h perpendicular

Figure 46: SEM images of the etched Ti-6.4Ni-2Cr+3vol% B_4C as-extruded samples (a-b), and the heat-treated samples (c-d)

4.1.6 Ti-8Al-1Mo-1V systems

The Ti-8Al-1Mo-1V or Ti811 alloy is classified as a near-α alloy. It consists of a high proportion of α-stabilising Al and small amounts of β-stabilising Mo and V. This results in a majority of α-phase and Ti_3Al, an ordered structure ($D0_{19}$-type superlattice) and small amounts of β-phase. It has the highest Young's modulus of all commercial titanium alloys (120 GPa) [32]. Figures 47 a-d and 48 e-f show the as-extruded Ti-8Al-1Mo-1V sample. As the powder mixture consists of several types of powder, namely Ti, Ti64, Al and Mo, a heterogeneous structure can be seen. While undissolved Mo-particles (SEM: light phase) and Al-rich titanium residues (SEM: dark phase) are present, a lamellar α/β microstructure lies in between these distributions. However, the heat-treated sample shows a homogeneous microstructure with no detectable undissolved residuals (Figure 47 c-d and 48 e-f). The heat treatment results in a bimodal two-phase material, consisting of α-grains and macrograins divided into a lamellar α/β-substructure combined with a grain coarsening. The as-extruded TiC-reinforced Ti-8Al-1Mo-1V sample is shown in Figures 49 a-b and 50 a-b. Again the same inhomogeneities are visible, as well as a texture in the longitudinal direction. The heat treatment leads to the same structure and grain coarsening (Figure 49 c-d and 50 c-d). However, the coarsening is not as pronounced as in the unreinforced alloy, due to the TiC-particles. In addition, the TiC did not react with the metallic matrix and remained the same. The addition of B_4C results in the same structural features in the as-extruded state (Figure 51 a-b and 52 a-b). Unlike the previous samples, the heat treatment does not result in a bimodal microstructure, but in equiaxed α grains with almost no grain boundary β-Ti and areas of α/β-structure. The B_4C particles have reacted to form TiC and acicular titanium borides.

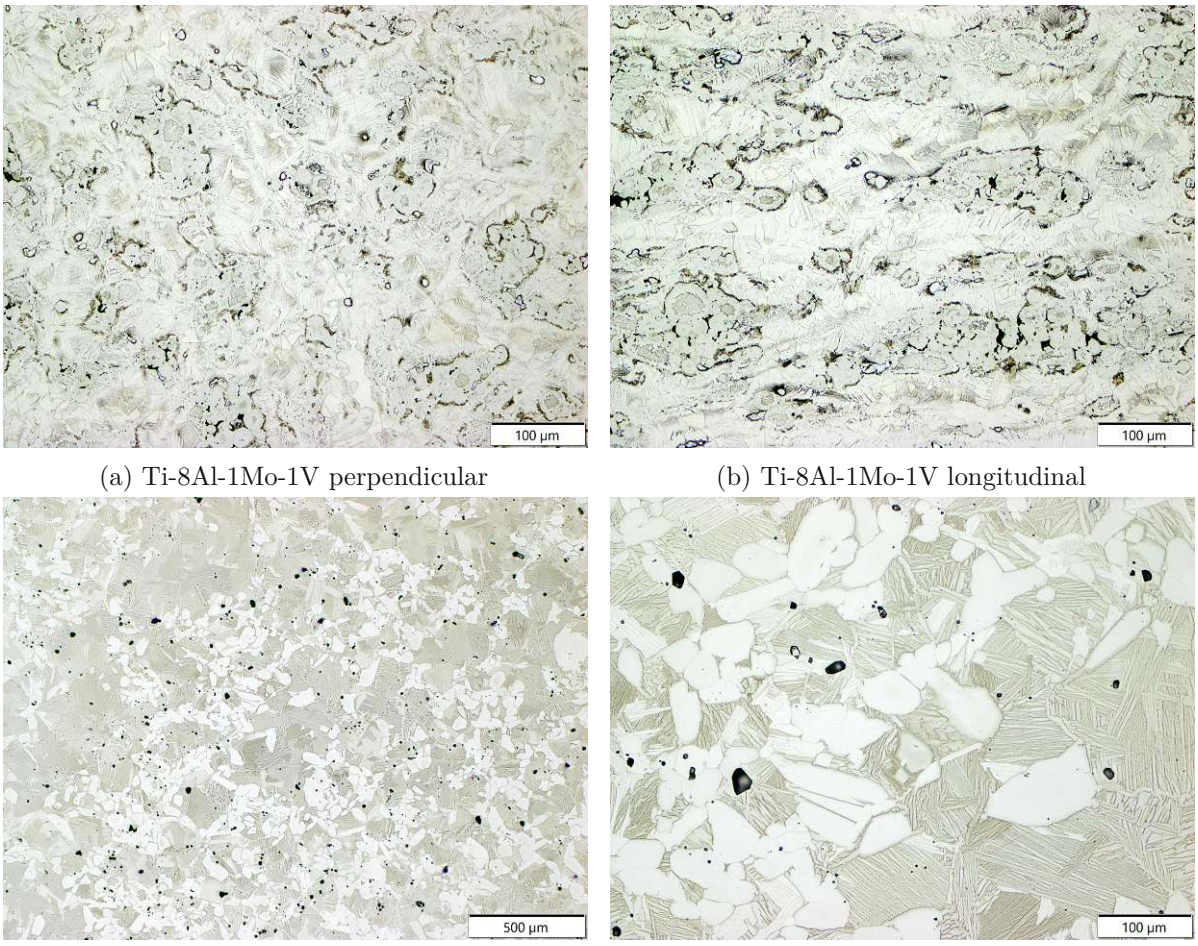

(a) Ti-8Al-1Mo-1V perpendicular

(b) Ti-8Al-1Mo-1V longitudinal

(c) Ti-8Al-1Mo-1V 1000 °C/90 h perpendicular

(d) Ti-8Al-1Mo-1V 1000 °C/90h perpendicular

Figure 47: Optical microscopy of the etched Ti-8Al-1Mo-1V as-extruded samples (a-b) and the heat-treated samples (c-d)

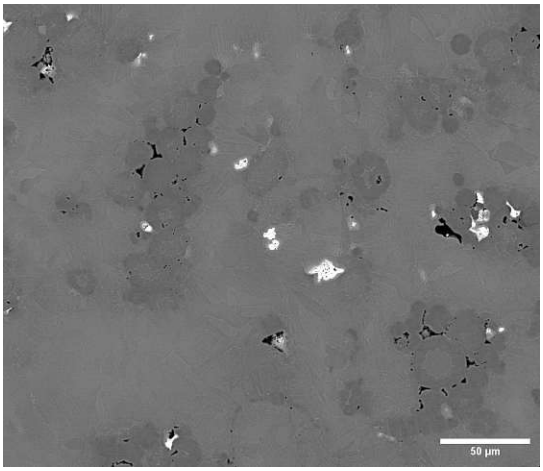

(a) Ti-8Al-1Mo-1V perpendicular

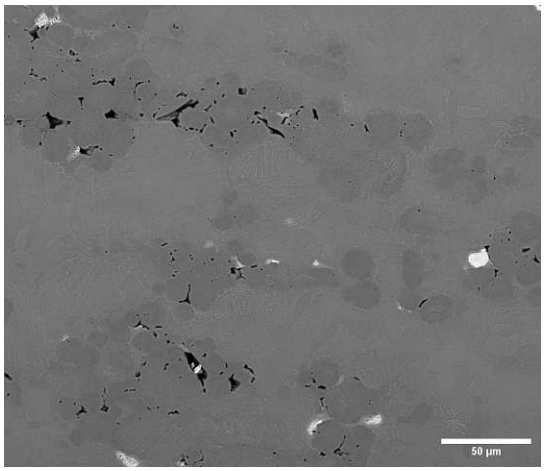

(b) Ti-8Al-1Mo-1V longitudinal

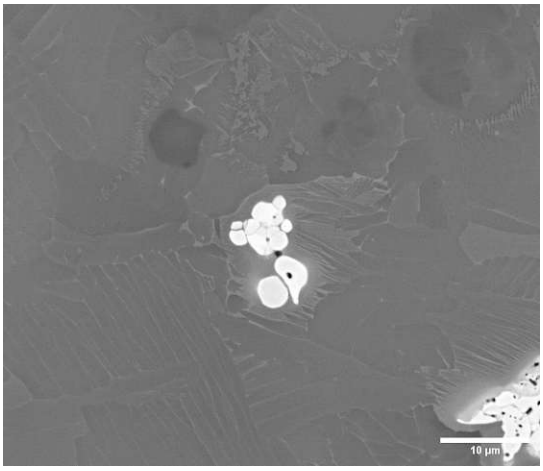

(c) Ti-8Al-1Mo-1V perpendicular

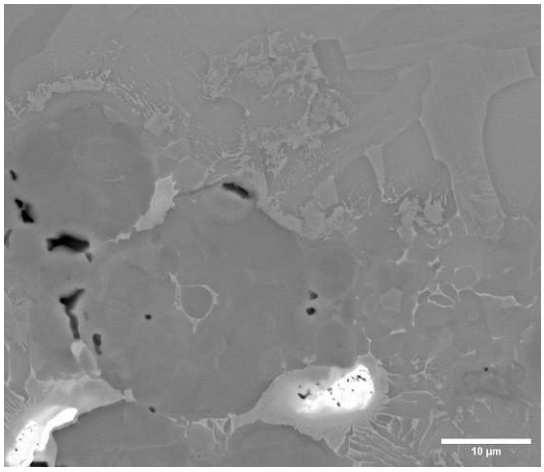

(d) Ti-8Al-1Mo-1V longitudinal

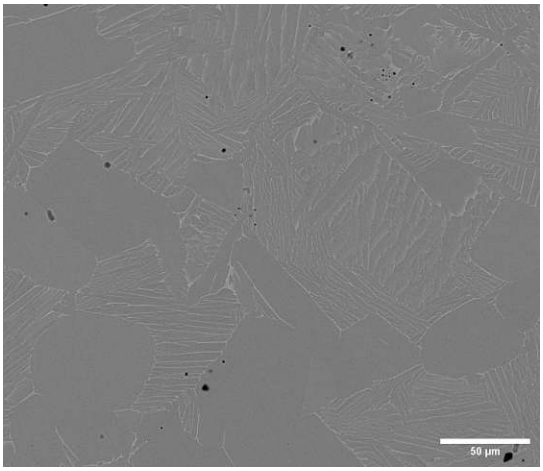

(e) Ti-8Al-1Mo-1V 1000 °C/90h perpendicular

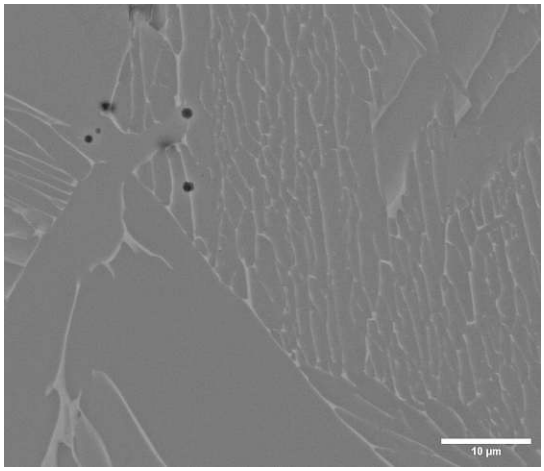

(f) Ti-8Al-1Mo-1V 1000 °C/90h perpendicular

Figure 48: SEM images of the etched Ti-8Al-1Mo-1V as-extruded samples (a-d), and the heat-treated samples (e-f)

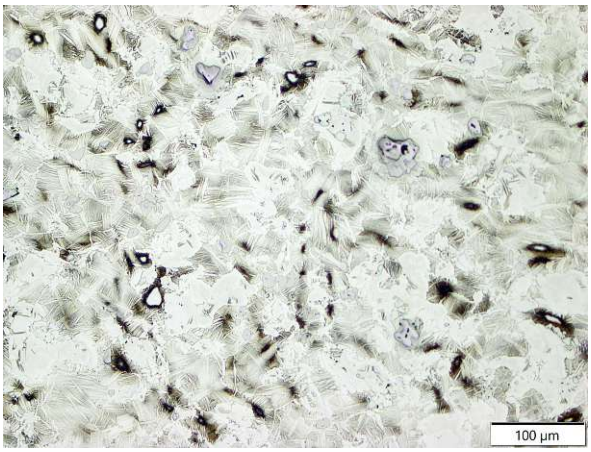

(a) Ti-8Al-1Mo-1V+3vol% TiC perpendicular

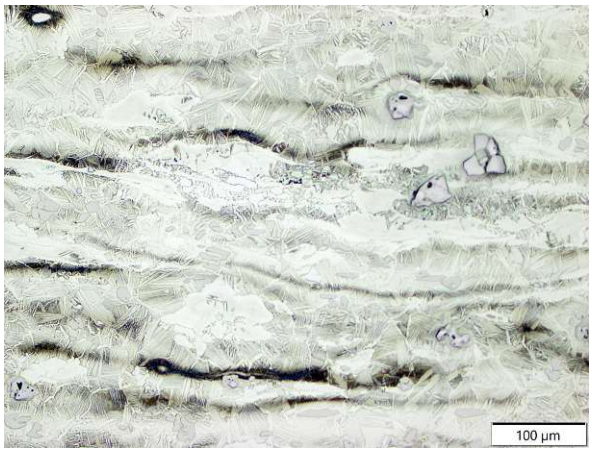

(b) Ti-8Al-1Mo-1V+3vol% TiC longitudinal

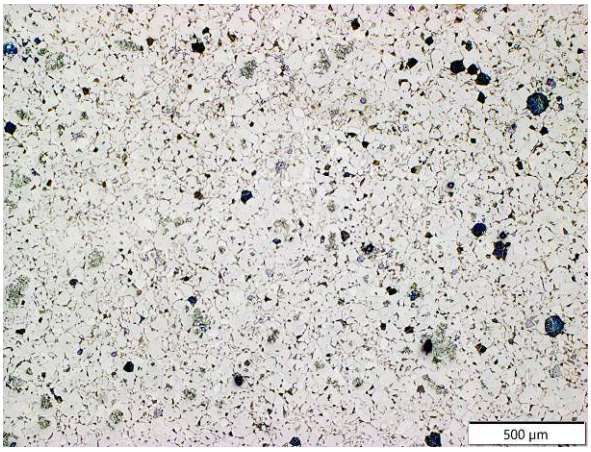

(c) Ti-8Al-1Mo-1V+3vol% TiC 1000 °C/90h perpendicular

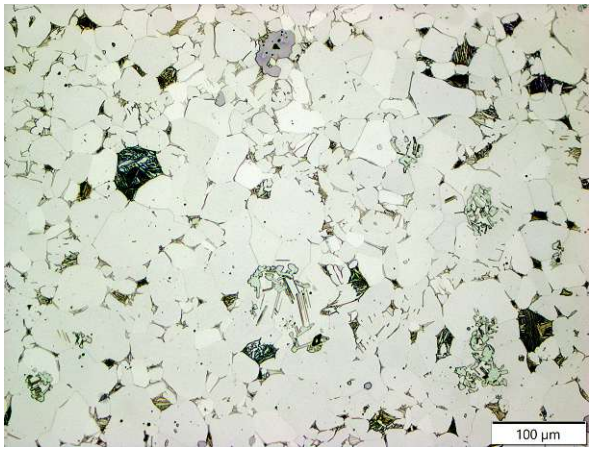

(d) Ti-8Al-1Mo-1V+3vol% TiC 1000 °C/90h perpendicular

Figure 49: Optical microscopy of the etched Ti-8Al-1Mo-1V as-extruded samples (a-b) and the heat-treated samples (c-d)

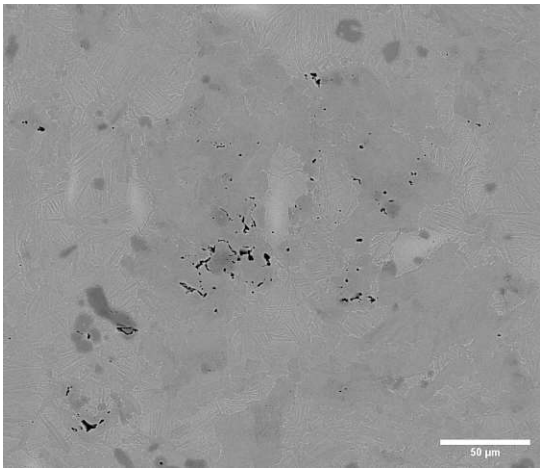

(a) Ti-8Al-1Mo-1V+3vol% TiC perpendicular

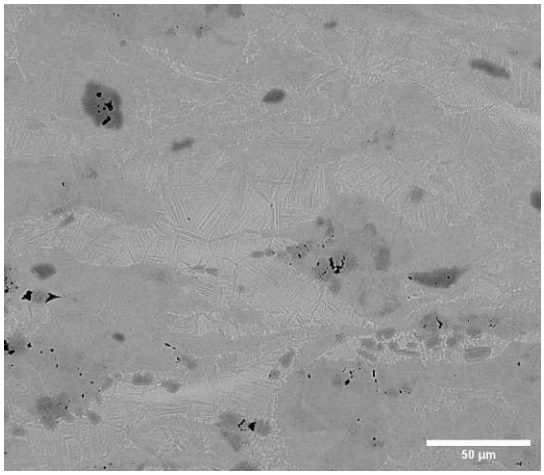

(b) Ti-8Al-1Mo-1V+3vol% TiC longitudinal

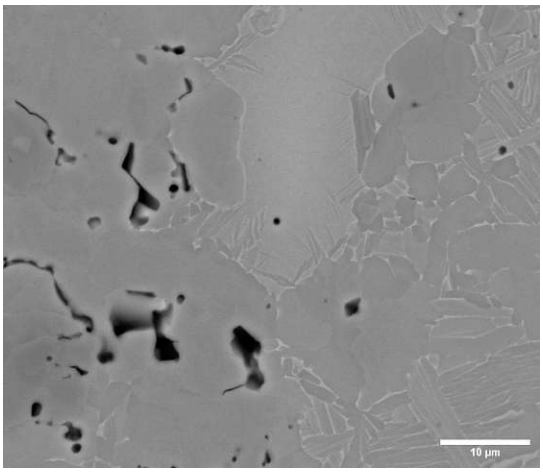

(c) Ti-8Al-1Mo-1V+3vol% TiC perpendicular

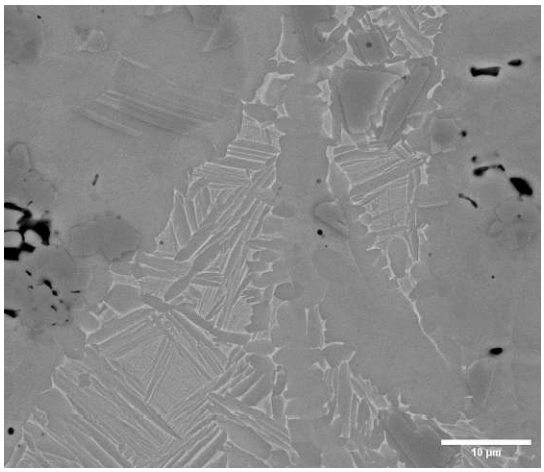

(d) Ti-8Al-1Mo-1V+3vol% TiC longitudinal

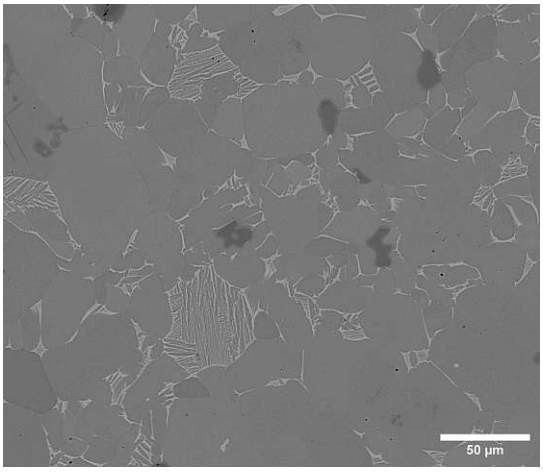

(e) Ti-8Al-1Mo-1V+3vol% TiC 1000 °C/90h perpendicular

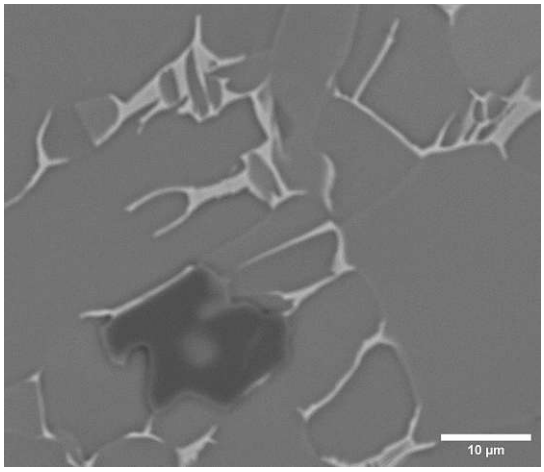

(f) Ti-8Al-1Mo-1V+3vol% TiC 1000 °C/90h perpendicular

Figure 50: SEM images of the etched Ti-8Al-1Mo-1V+3vol% TiC as-extruded samples (a-b), and the heat-treated samples (c-d)

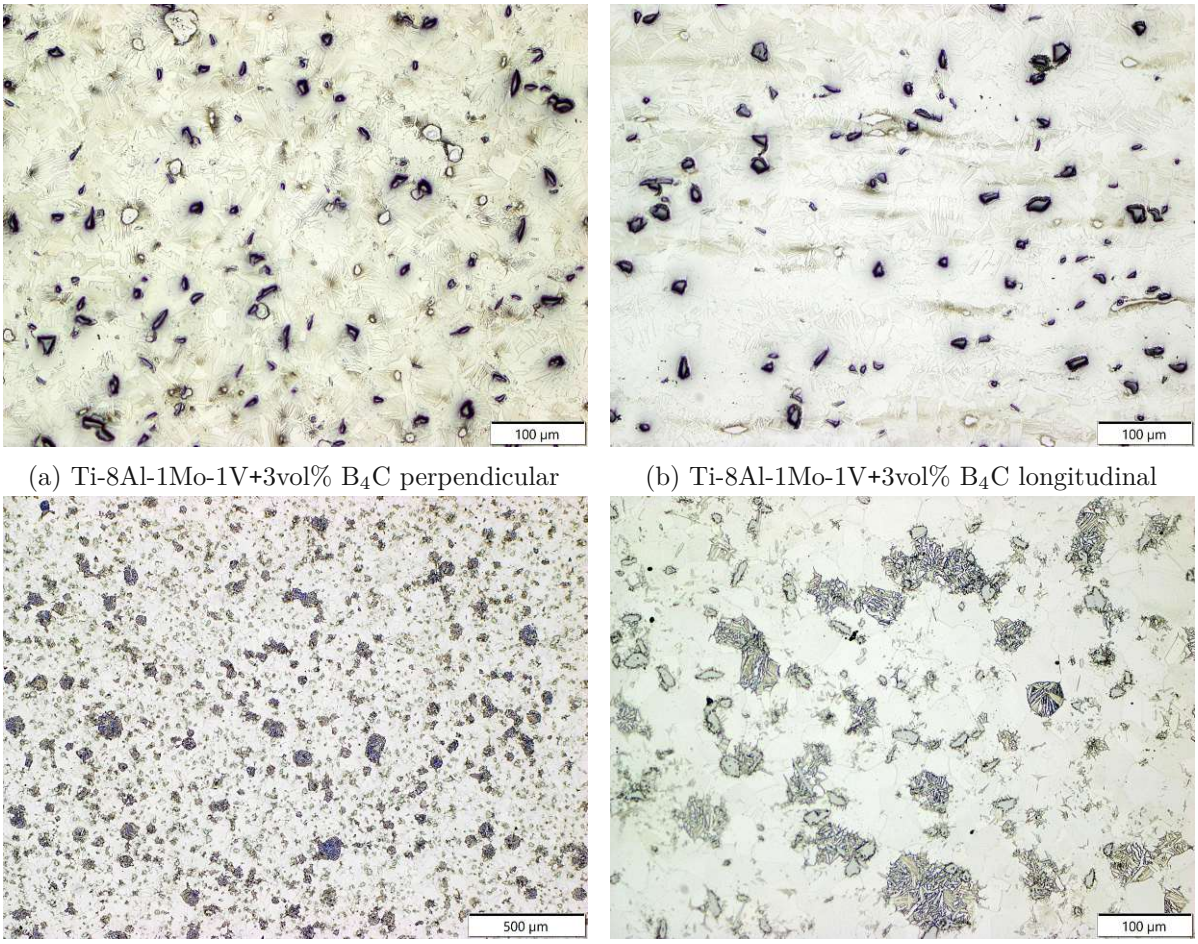

(a) Ti-8Al-1Mo-1V+3vol% B_4C perpendicular

(b) Ti-8Al-1Mo-1V+3vol% B_4C longitudinal

(c) Ti-8Al-1Mo-1V+3vol% B_4C 1000 °C/90h perpendicular

(d) Ti-8Al-1Mo-1V+3vol% B_4C 1000 °C/90h perpendicular

Figure 51: Optical microscopy of the etched Ti-8Al-1Mo-1V as-extruded samples (a-b) and the heat-treated samples (c-d)

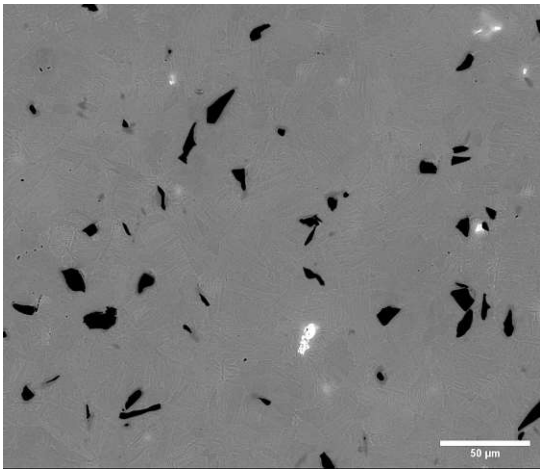

(a) Ti-8Al-1Mo-1V+3vol% B_4C perpendicular

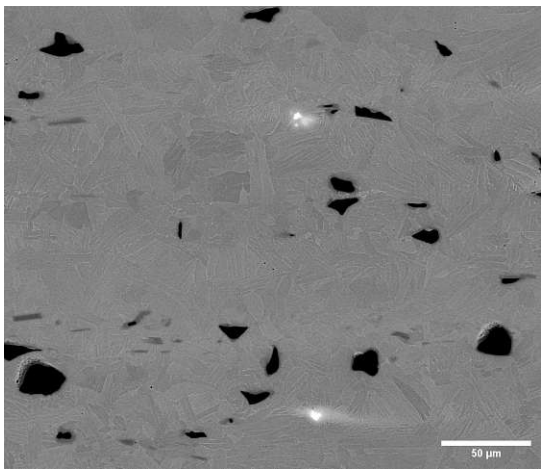

(b) Ti-8Al-1Mo-1V+3vol% B_4C longitudinal

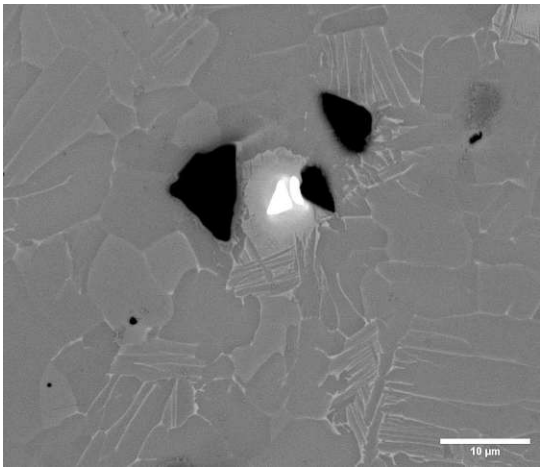

(c) Ti-8Al-1Mo-1V+3vol% B_4C perpendicular

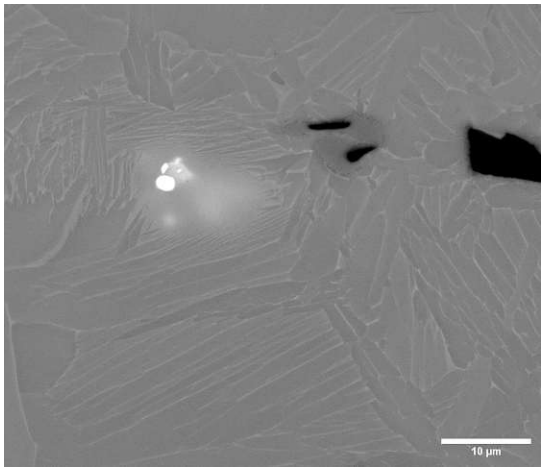

(d) Ti-8Al-1Mo-1V+3vol% B_4C longitudinal

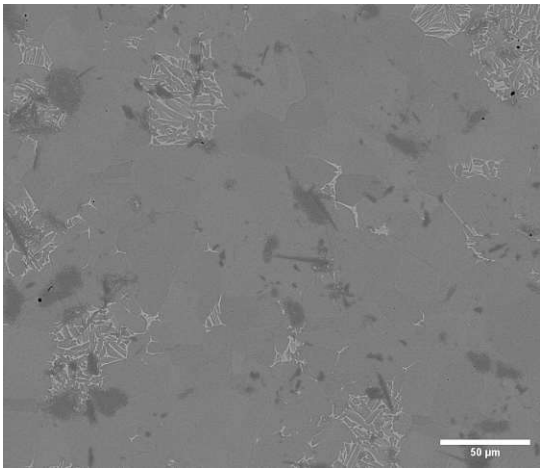

(e) Ti-8Al-1Mo-1V+3vol% B_4C 1000 °C/90h perpendicular

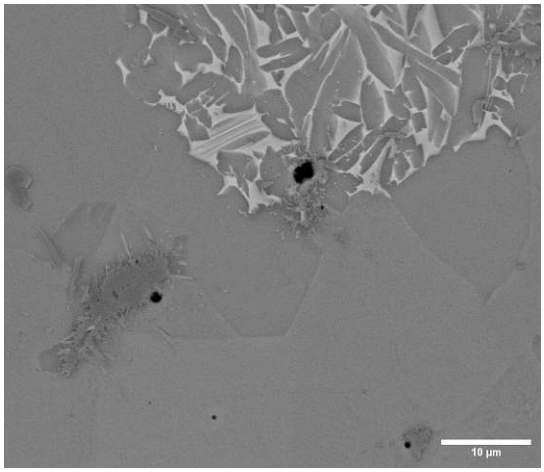

(f) Ti-8Al-1Mo-1V+3vol% B_4C 1000 °C/90h perpendicular

Figure 52: SEM images of the etched Ti-8Al-1Mo-1V+3vol%B_4C as-extruded samples (a-d), and the heat-treated samples (e-f)

4.1.7 Ti-5.7Al-5Co-3.8V systems

It has been found that the addition of 5 wt% Co to the Ti-6Al-4V alloy results in an increase in strength and promotes the formation of an equiaxed microstructure [29, 41]. This system is therefore an interesting candidate for extrusion experiments. Figures 53 a-b and 56 a-d show the microstructure of the as-extruded Ti-5.7Al-5Co-3.8V sample. The Co is completely dissolved during the extrusion process and an optically dense homogeneous two-phase structure is obtained. There is no structural difference between the perpendicular and longitudinal directions. It consists of equiaxed macrograins separated by α-Ti. The macrograins themselves have a woven α/β-substructure. The dark phase (SEM) represents the α-Ti with solid solutes of Al, the light phase (SEM) is β-Ti containing Co and V. The heat-treated sample is shown in figures 53 c-d and 54 e-f. The heat treatment causes further accumulation of α-Ti at the grain boundaries, resulting in a coarsening of the grain boundaries. The addition of TiC results in a fining of the microstructure (Figures 55 a-b and 56 a-d). Residues of the Co powder can be seen in the longitudinal direction. The heat treatment leads to an accumulation of α-Ti at the grain boundaries (Figures 55 c-d and 56 e-f). The addition of B_4C seems to inhibit the formation of α-Ti grain boundaries, resulting in very fine α acicular grains with interspersed β-Ti (Figures 57 a-b and 58 a-d). A longitudinal smear can be seen. The heat treatment results in grain coarsening and spattering of the B_4C, but no characteristic accicular titanium borides are detected.

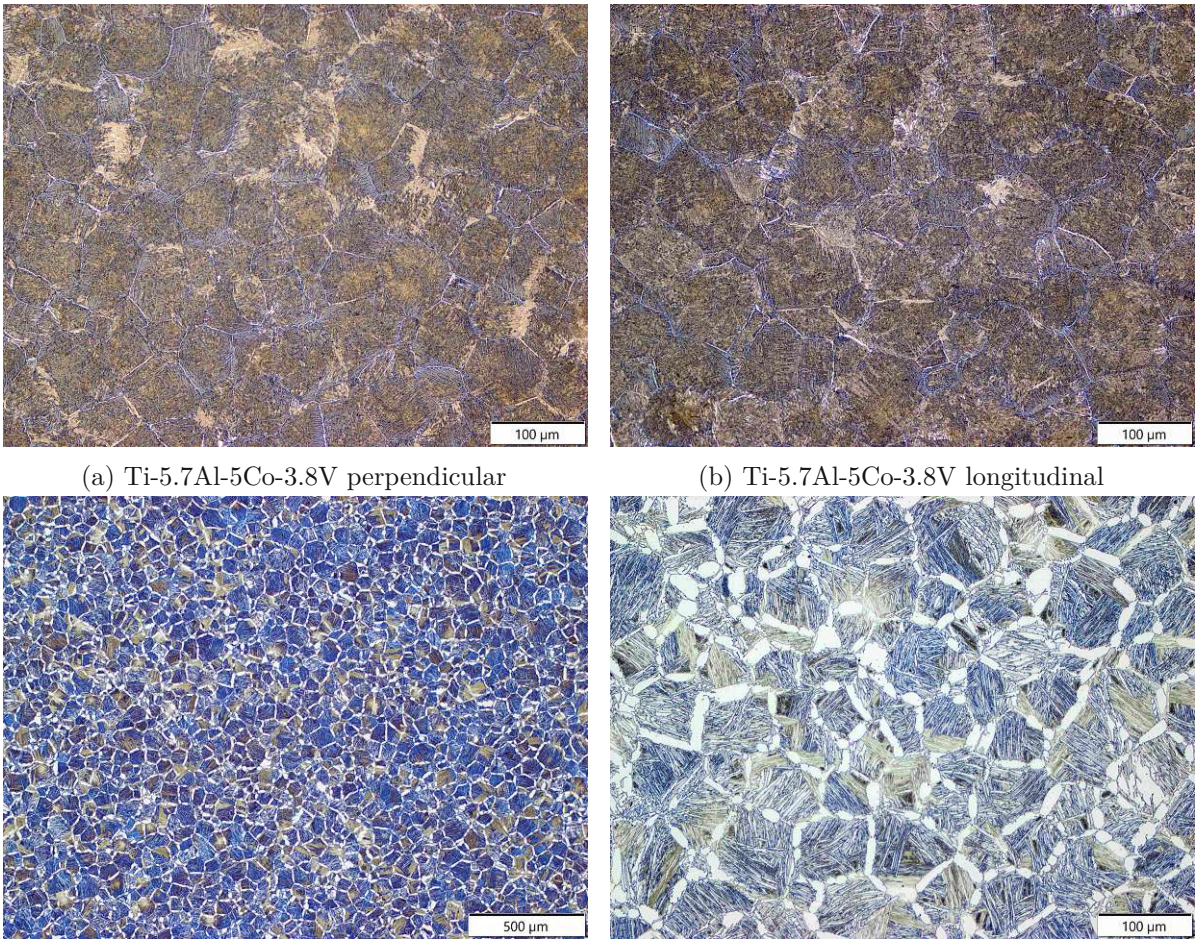

(a) Ti-5.7Al-5Co-3.8V perpendicular

(b) Ti-5.7Al-5Co-3.8V longitudinal

(c) Ti-5.7Al-5Co-3.8V 1000 °C/90h perpendicular

(d) Ti-5.7Al-5Co-3.8V 1000 °C/90h perpendicular

Figure 53: Optical microscopy of the etched Ti-5.7Al-5Co-3.8V as-extruded samples (a-b) and the heat-treated samples (c-d)

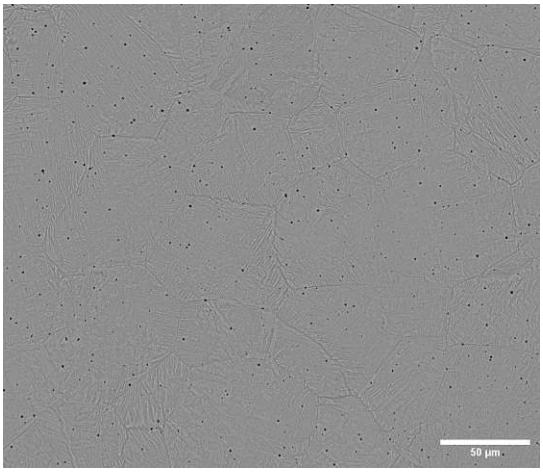

(a) Ti-5.7Al-5Co-3.8V perpendicular

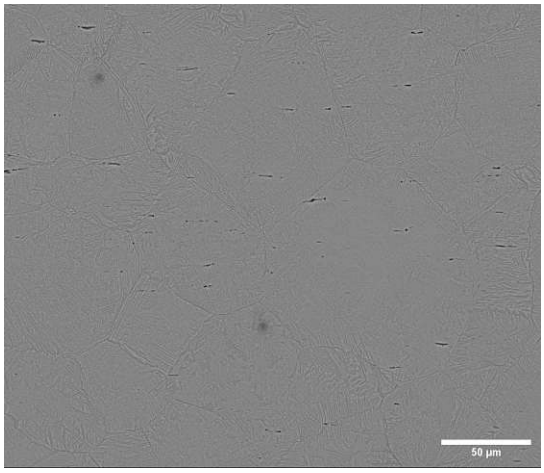

(b) Ti-5.7Al-5Co-3.8V longitudinal

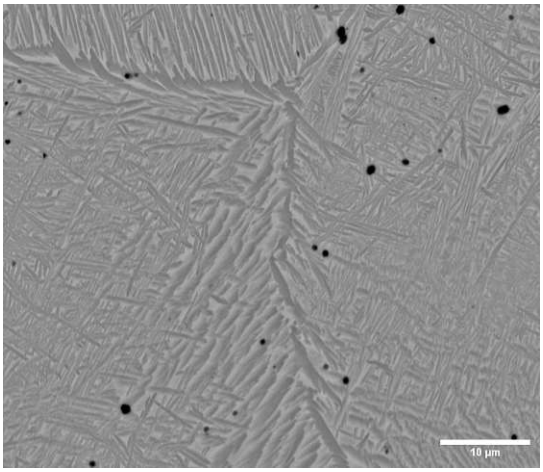

(c) Ti-5.7Al-5Co-3.8V perpendicular

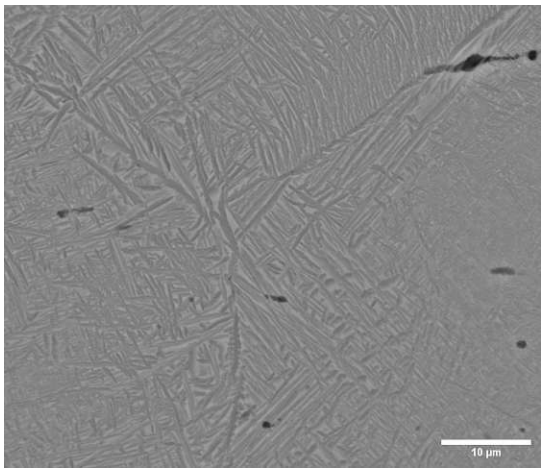

(d) Ti-5.7Al-5Co-3.8V longitudinal

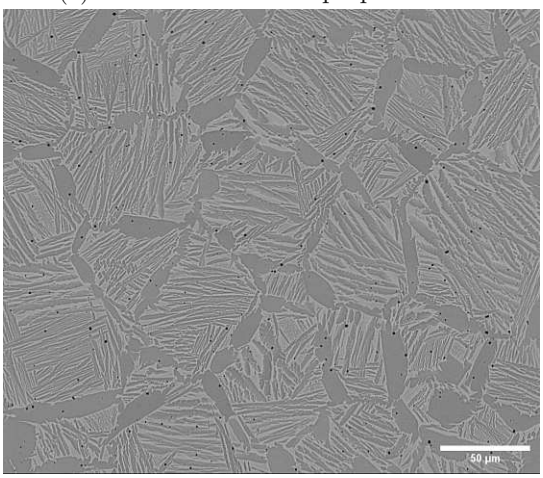

(e) Ti-5.7Al-5Co-3.8V 1000 °C/90h perpendicular

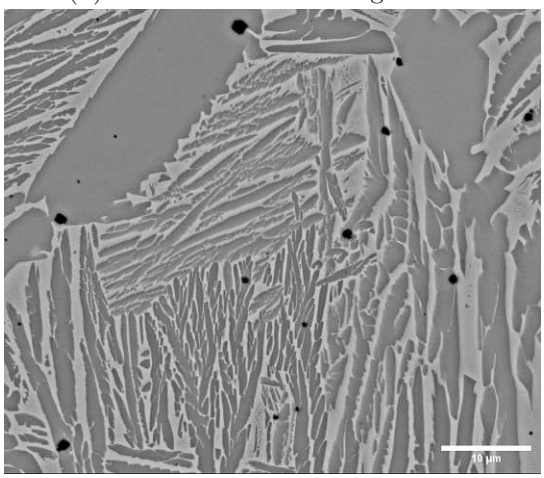

(f) Ti-5.7Al-5Co-3.8V 1000 °C/90h perpendicular

Figure 54: SEM images of the etched Ti-5.7Al-5Co-3.8V as-extruded samples (a-d), and the heat-treated samples (e-f)

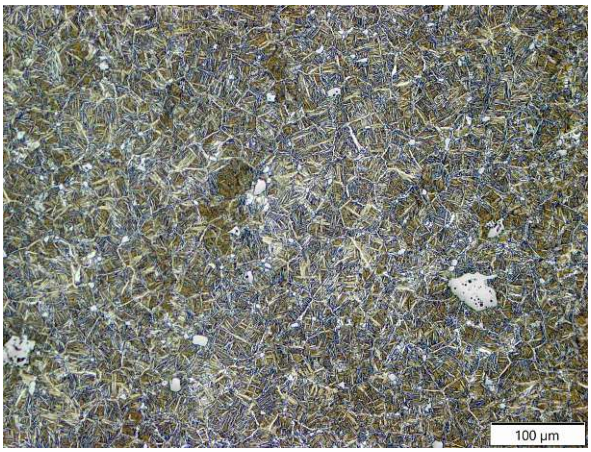

(a) Ti-5.7Al-5Co-3.8V+3vol% TiC perpendicular

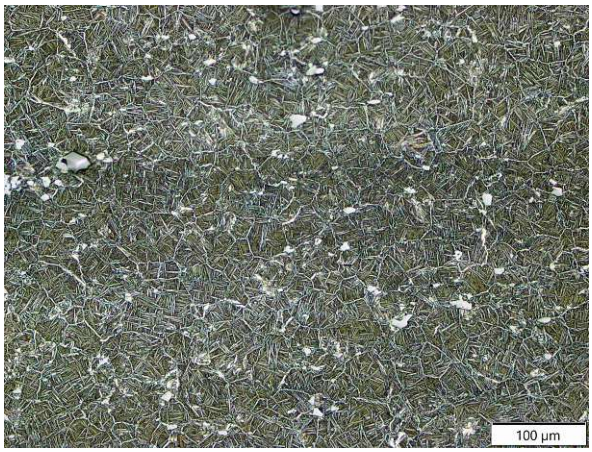

(b) Ti-5.7Al-5Co-3.8V+3vol% TiC longitudinal

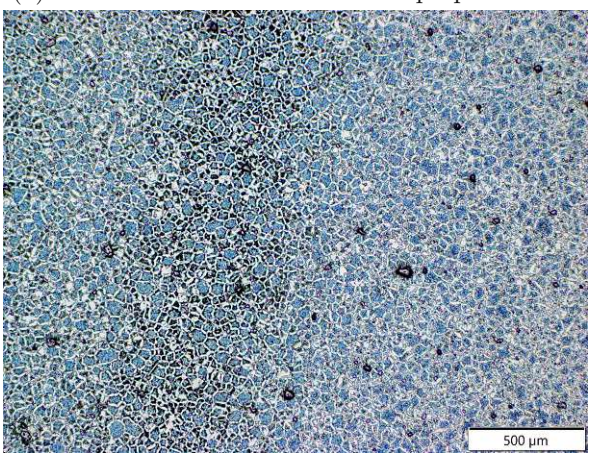

(c) Ti-5.7Al-5Co-3.8V+3vol% TiC 1000 °C/90h perpendicular

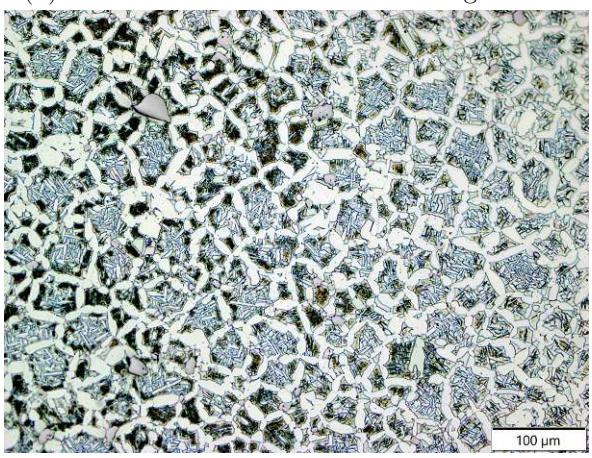

(d) Ti-5.7Al-5Co-3.8V+3vol% TiC 1000 °C/90h perpendicular

Figure 55: Optical microscopy of the etched Ti-5.7Al-5Co-3.8V+3vol% TiC as-extruded samples (a-b) and the heat-treated samples (c-d)

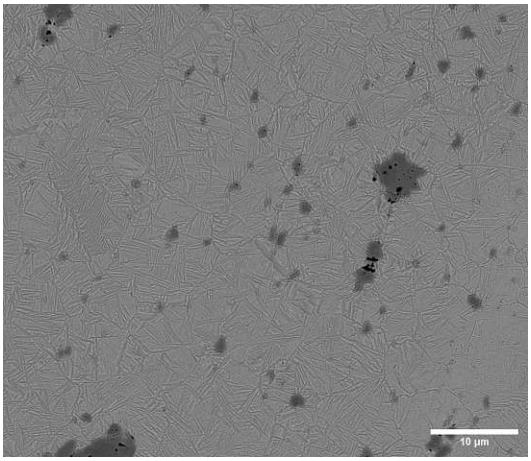

(a) Ti-5.7Al-5Co-3.8V+3vol% TiC perpendicular

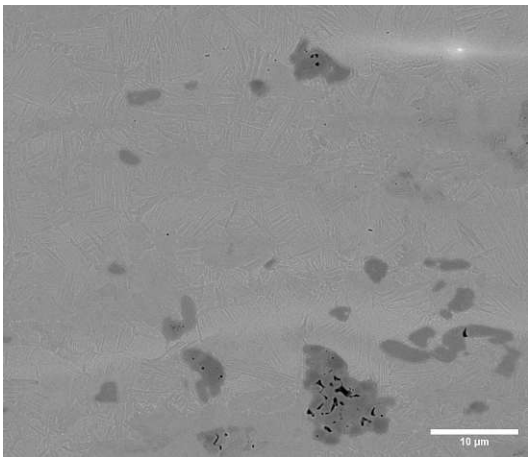

(b) Ti-5.7Al-5Co-3.8V+3vol% TiC longitudinal

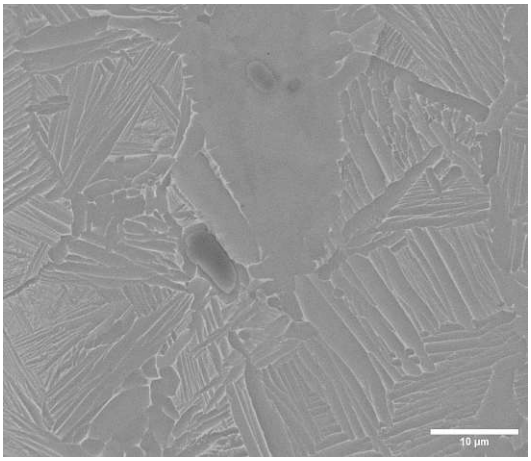

(c) Ti-5.7Al-5Co-3.8V+3vol% TiC perpendicular

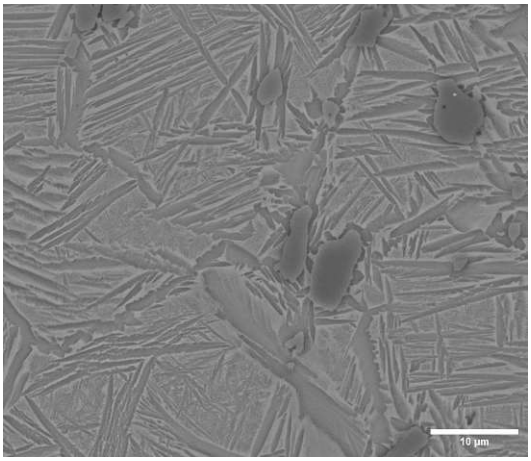

(d) Ti-5.7Al-5Co-3.8V+3vol% TiC longitudinal

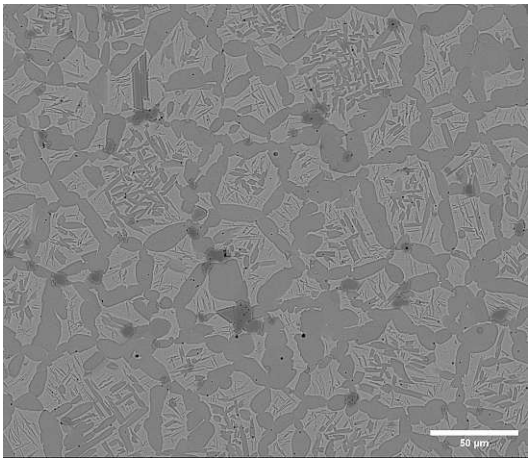

(e) Ti-5.7Al-5Co-3.8V+3vol% TiC 1000 °C/90h perpendicular

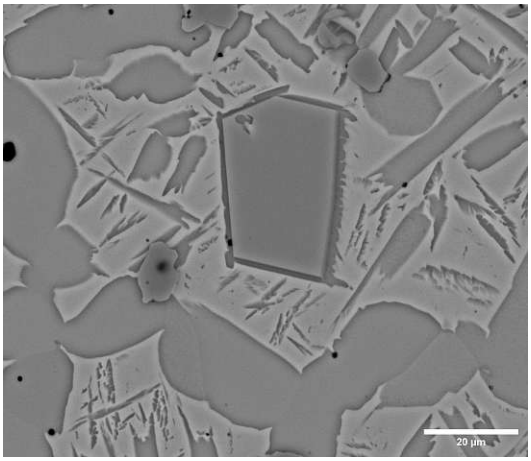

(f) Ti-5.7Al-5Co-3.8V+3vol% TiC 1000 °C/90h perpendicular

Figure 56: SEM images of the etched Ti-5.7Al-5Co-3.8V+3vol% TiC as-extruded samples (a-d), and the heat-treated samples (e-f)

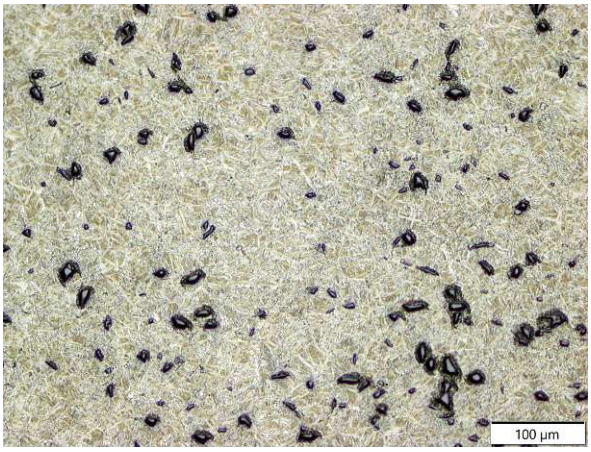

(a) Ti-5.7Al-5Co-3.8V+3vol% B_4C perpendicular

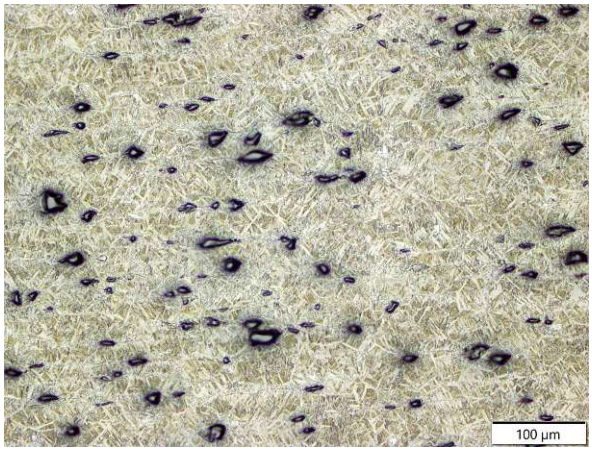

(b) Ti-5.7Al-5Co-3.8V+3vol% B_4C longitudinal

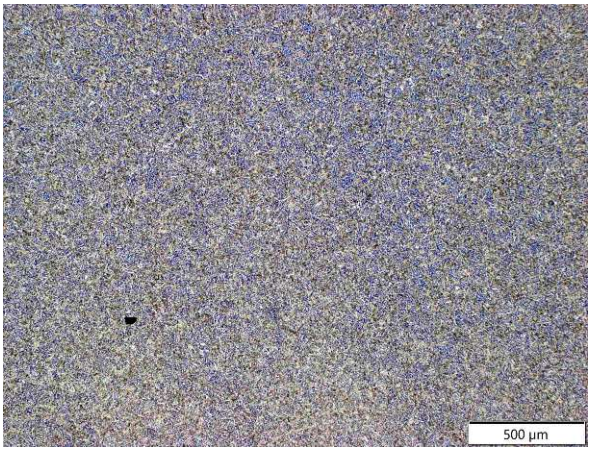

(c) Ti-5.7Al-5Co-3.8V+3vol% B_4C 1000 °C/90h perpendicular

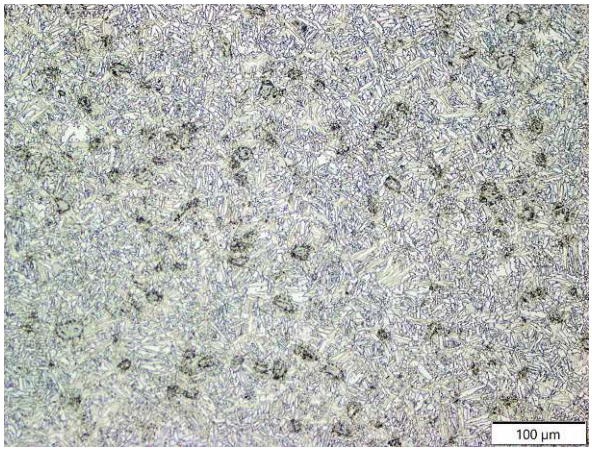

(d) Ti-5.7Al-5Co-3.8V+3vol% B_4C 1000 °C/90h perpendicular

Figure 57: Optical microscopy of the etched Ti-5.7Al-5Co-3.8V+3vol% B_4C as-extruded samples (a-b) and the heat-treated samples (c-d)

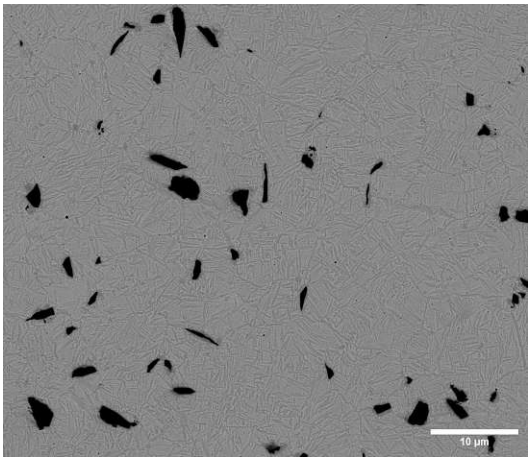

(a) Ti-5.7Al-5Co-3.8V+3vol% B_4C perpendicular

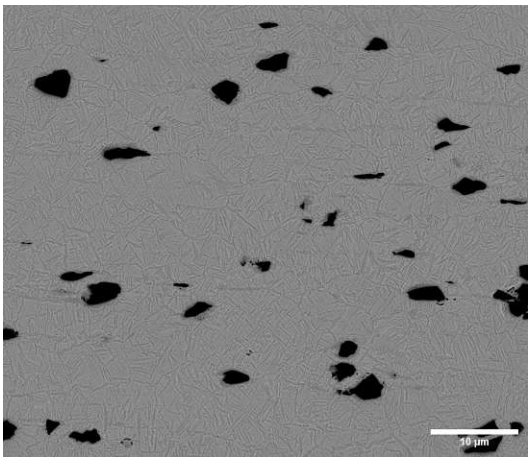

(b) Ti-5.7Al-5Co-3.8V+3vol% B_4C longitudinal

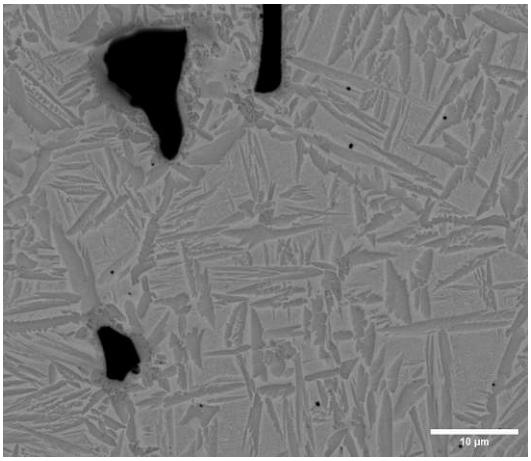

(c) Ti-5.7Al-5Co-3.8V+3vol% B_4C perpendicular

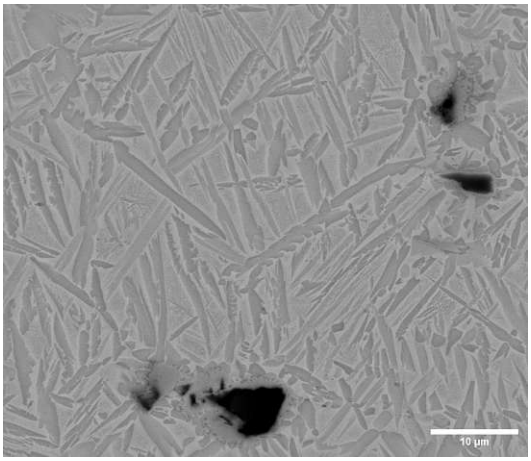

(d) Ti-5.7Al-5Co-3.8V+3vol% B_4C longitudinal

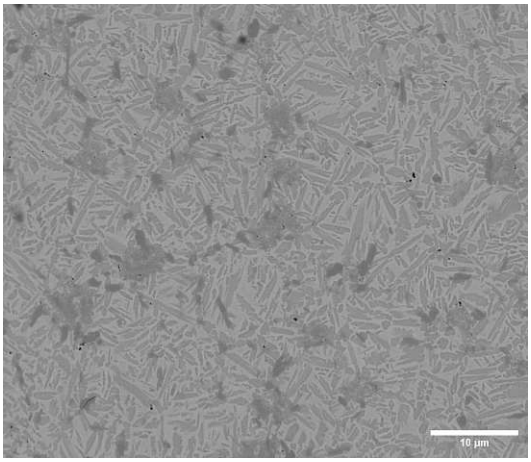

(e) Ti-5.7Al-5Co-3.8V+3vol% B_4C 1000 °C/90h perpendicular

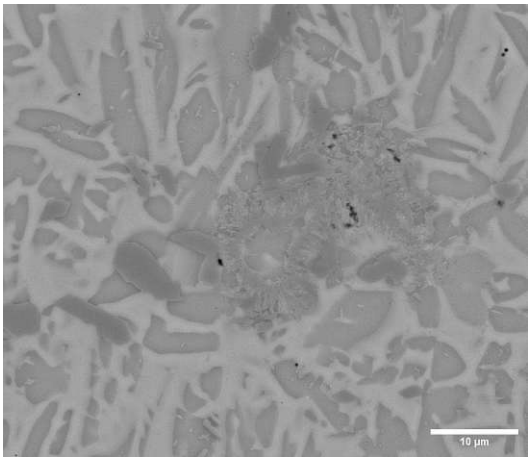

(f) Ti-5.7Al-5Co-3.8V+3vol% B_4C 1000 °C/90h perpendicular

Figure 58: SEM images of the etched Ti-5.7Al-5Co-3.8V+3vol% B_4C as-extruded samples (a-d), and the heat-treated samples (e-f)

4.1.8 Ti-4Al-3Cu-2Fe systems

The Ti-4Al-3Cu-2Fe promises significantly high strength [46]. However, to improve the stiffness, particles are considered. Figures 59 a-b and 60 a-d show the as-extruded Ti-4Al-3Cu-2Fe alloy. In addition to a lamellar microstructure, undissolved Fe-residues elongated in the extrusion direction can be seen. The copper is completely dissolved. Two phases can be distinguished in the SEM images, a dark phase containing aluminium and a light phase rich in copper and iron. The heat-treated sample (Figures 63 c-d and 64 e-f) shows no residual iron. Significant grain growth is also observed. The Ti-4Al-3Cu-2Fe with 3 vol% TiC is shown in figures 61 a-b and 62 a-d. As seen in the previous samples, the addition of particles leads to grain refinement. Again some Fe particles remain undissolved and are smeared. Heat treatment results in a coarsening of the microstructure, with the TiC particles remaining (Figure 61 c-d and 62 e-f). The addition of 3vol% B_4C leads to a significant refinement (Figures 63 a-b and 64 a-d). However, undissolved iron can still be detected. The heat treatment leads to a coarsening and transformation of the grains into a more equiaxed shape (Figures 63 c-d and 64 e-f). The B_4C is converted into borides and TiC.

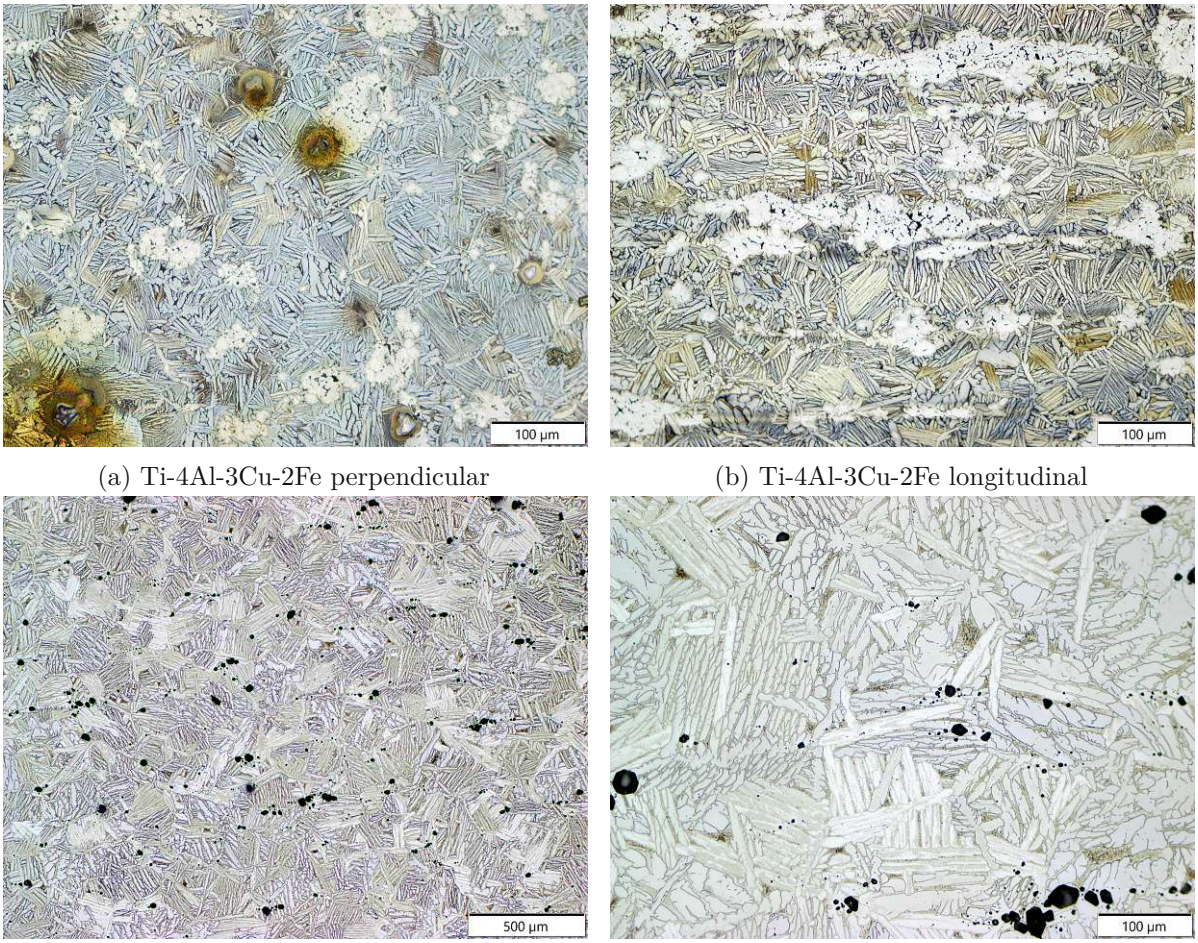

(a) Ti-4Al-3Cu-2Fe perpendicular

(b) Ti-4Al-3Cu-2Fe longitudinal

(c) Ti-4Al-3Cu-2Fe 1000 °C/90h perpendicular

(d) Ti-4Al-3Cu-2Fe 1000 °C/90h perpendicular

Figure 59: Optical microscopy of the etched Ti-4Al-3Cu-2Fe as-extruded samples (a-b) and the heat-treated samples (c-d)

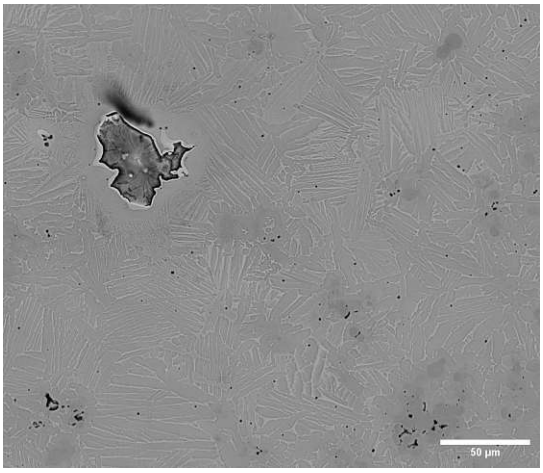

(a) Ti-4Al-3Cu-2Fe perpendicular

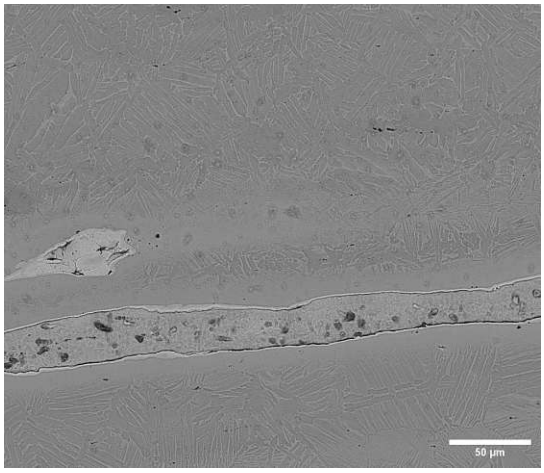

(b) Ti-4Al-3Cu-2Fe longitudinal

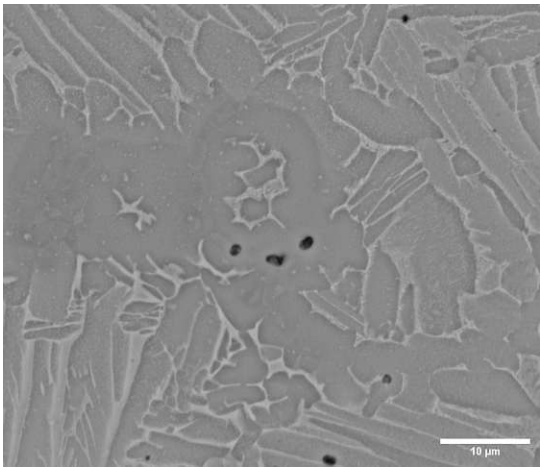

(c) Ti-4Al-3Cu-2Fe perpendicular

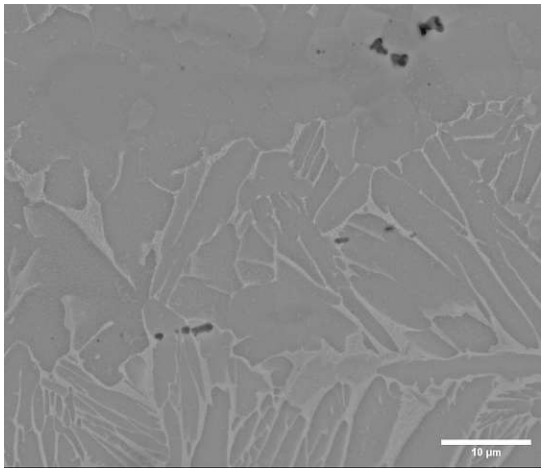

(d) Ti-4Al-3Cu-2Fe longitudinal

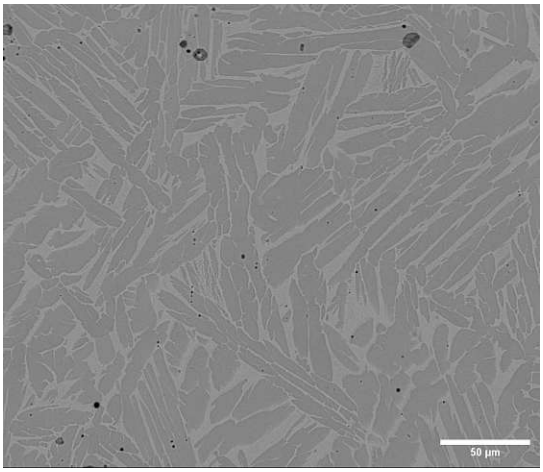

(e) Ti-4Al-3Cu-2Fe 1000 °C/90h perpendicular

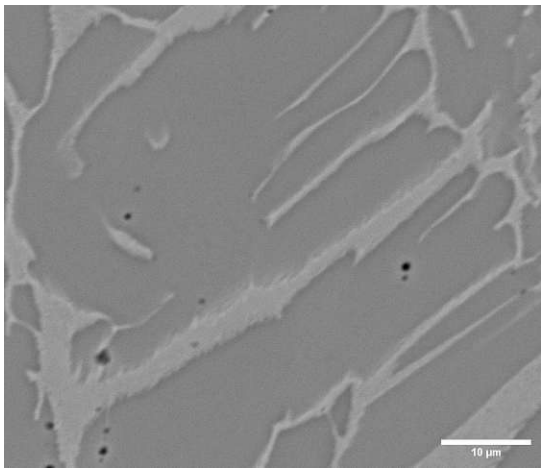

(f) Ti-4Al-3Cu-2Fe 1000 °C/90h perpendicular

Figure 60: SEM images of the etched Ti-4Al-3Cu-2Fe as-extruded samples (a-b), and the heat-treated samples (c-d)

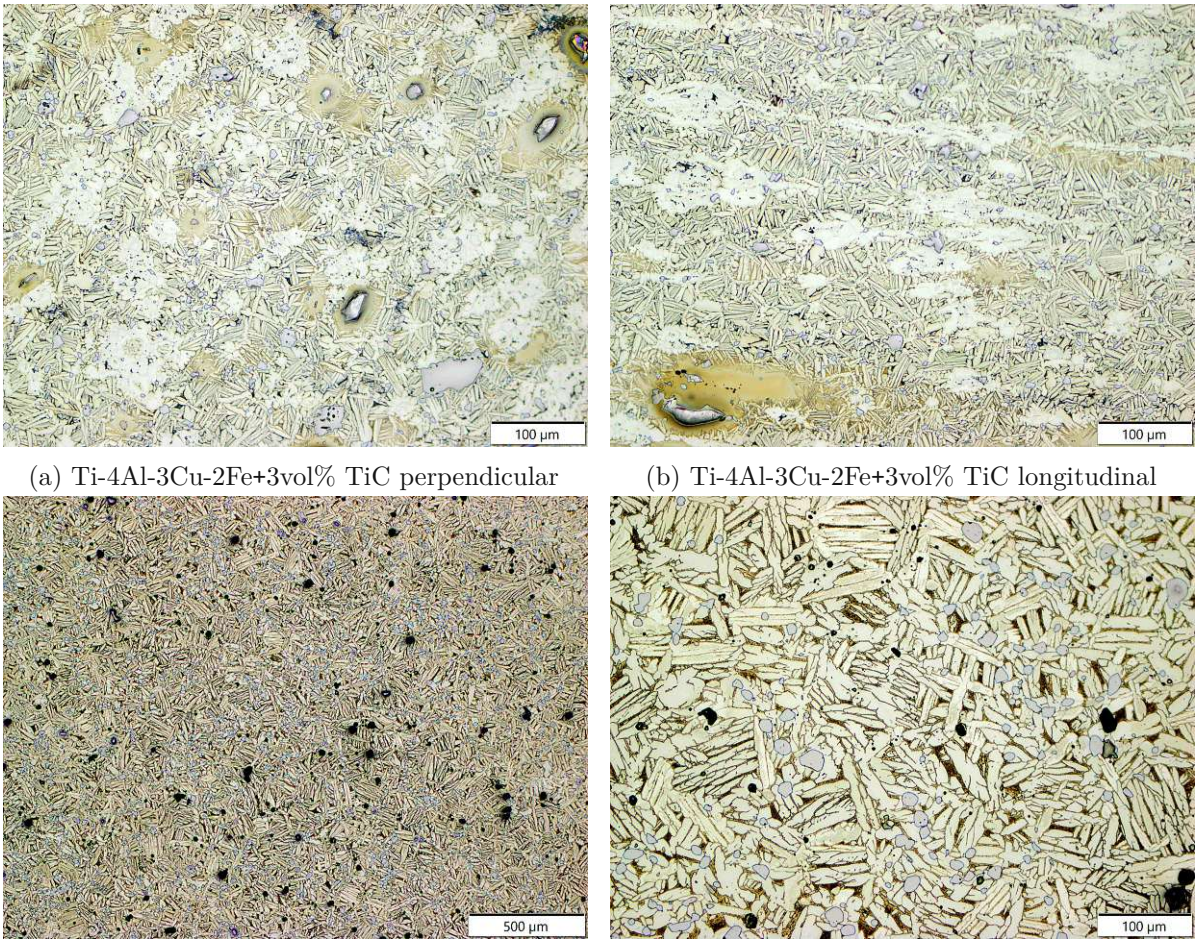

(a) Ti-4Al-3Cu-2Fe+3vol% TiC perpendicular

(b) Ti-4Al-3Cu-2Fe+3vol% TiC longitudinal

(c) Ti-4Al-3Cu-2Fe+3vol% TiC 1000 °C/90h perpendicular

(d) Ti-4Al-3Cu-2Fe+3vol% TiC 1000 °C/90h perpendicular

Figure 61: Optical microscopy of the etched Ti-4Al-3Cu-2Fe+3vol% TiC as-extruded samples (a-b) and the heat-treated samples (c-d)

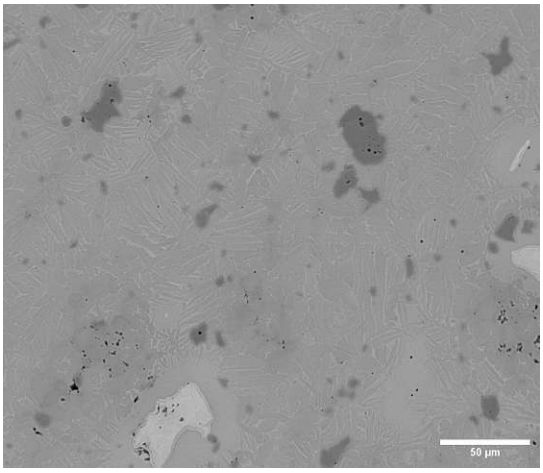

(a) Ti-4Al-3Cu-2Fe+3vol% TiC perpendicular

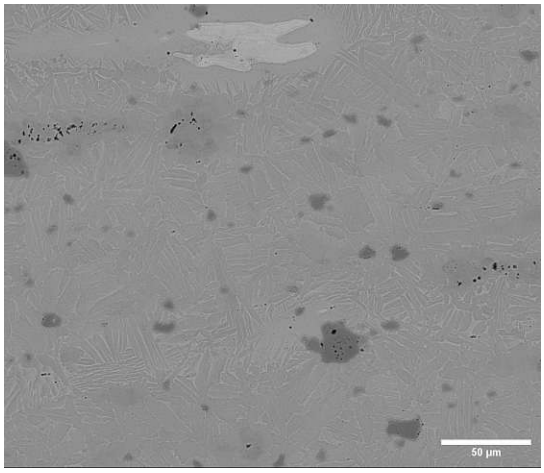

(b) Ti-4Al-3Cu-2Fe+3vol% TiC longitudinal

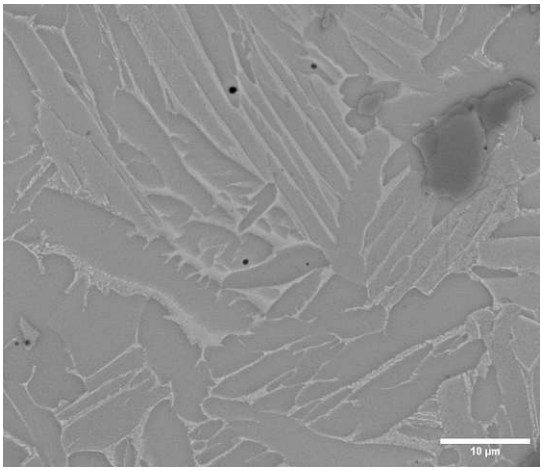

(c) Ti-4Al-3Cu-2Fe+3vol% TiC perpendicular

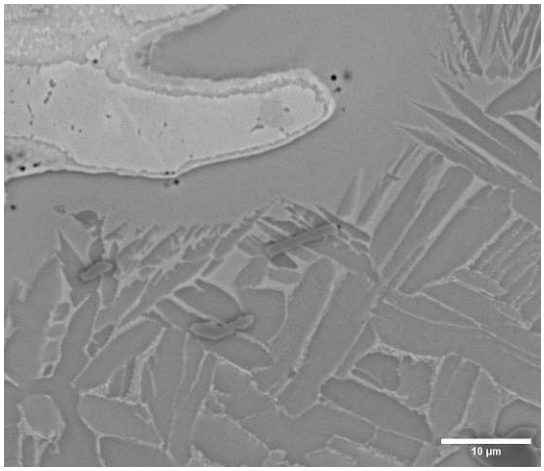

(d) Ti-4Al-3Cu-2Fe+3vol% TiC longitudinal

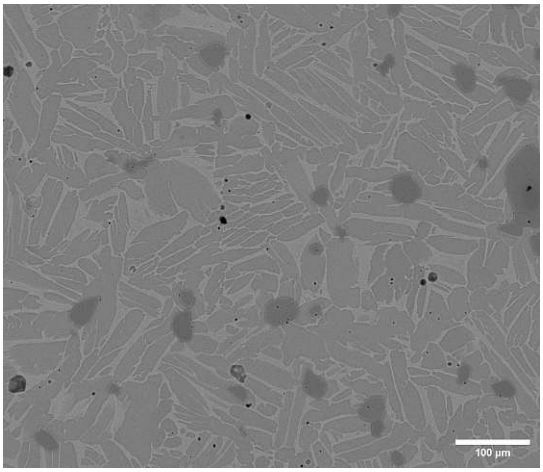

(e) Ti-4Al-3Cu-2Fe+3vol% TiC 1000 °C/90h perpendicular

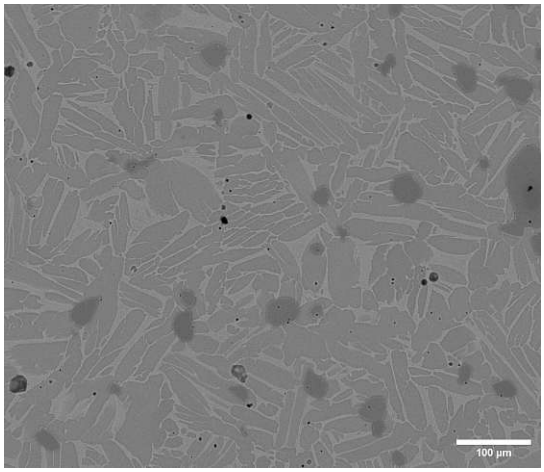

(f) Ti-4Al-3Cu-2Fe+3vol% TiC 1000 °C/90h perpendicular

Figure 62: SEM images of the etched Ti-4Al-3Cu-2Fe+3vol% TiC as-extruded samples (a-b), and the heat-treated samples (c-d)

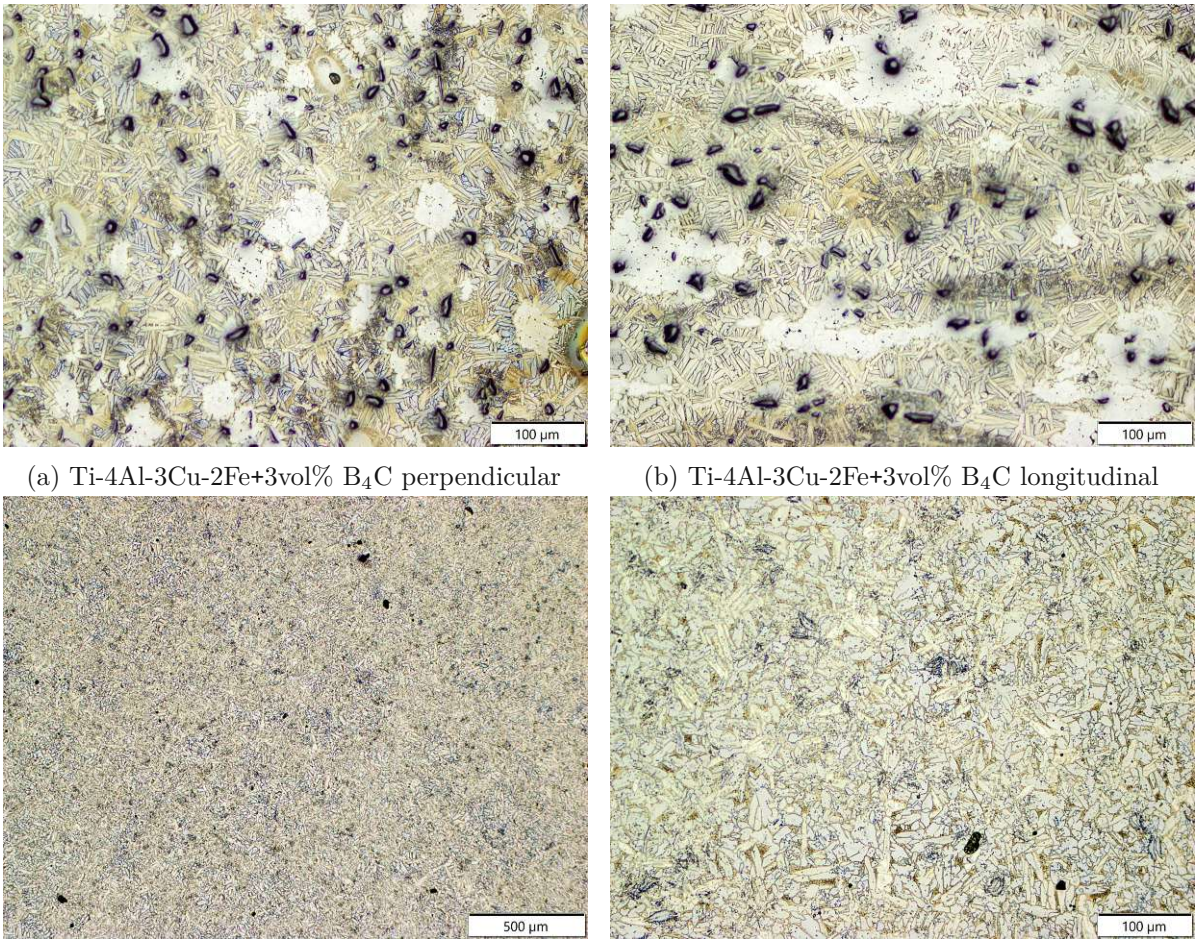

(a) Ti-4Al-3Cu-2Fe+3vol% B_4C perpendicular

(b) Ti-4Al-3Cu-2Fe+3vol% B_4C longitudinal

(c) Ti-4Al-3Cu-2Fe+3vol% B_4C 1000 °C/90h perpendicular

(d) Ti-4Al-3Cu-2Fe+3vol% B_4C 1000 °C/90h perpendicular

Figure 63: Optical microscopy of the etched Ti-4Al-3Cu-2Fe+3vol% B_4C as-extruded samples (a-b) and the heat-treated samples (c-d)

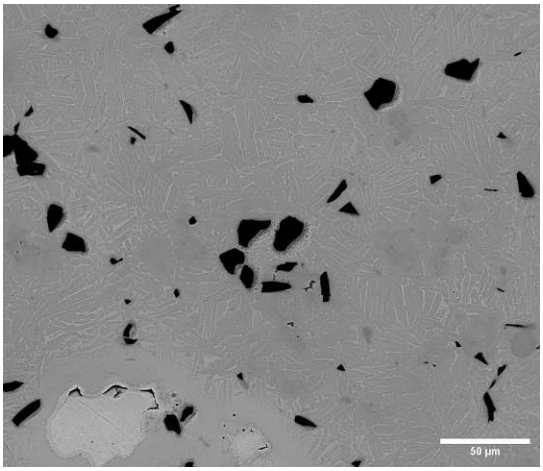

(a) Ti-4Al-3Cu-2Fe+3vol% B_4C perpendicular

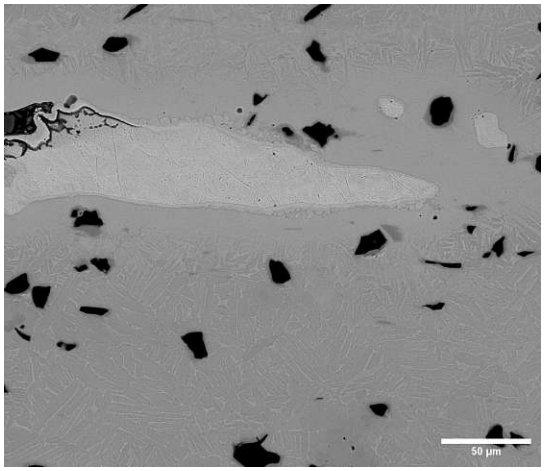

(b) Ti-4Al-3Cu-2Fe+3vol% B_4C longitudinal

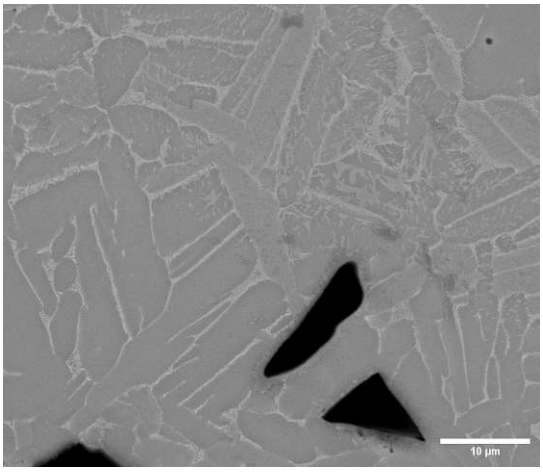

(c) Ti-4Al-3Cu-2Fe+3vol% B_4C perpendicular

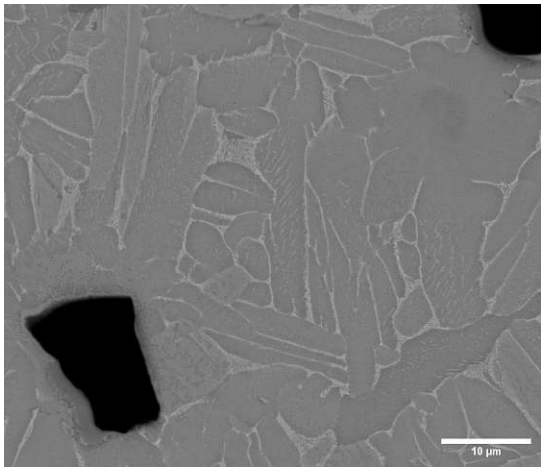

(d) Ti-4Al-3Cu-2Fe+3vol% B_4C longitudinal

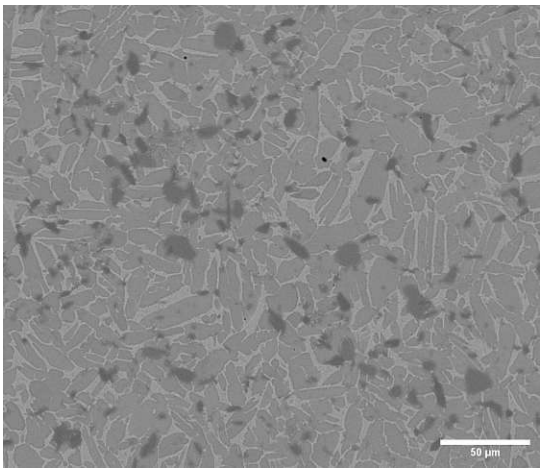

(e) Ti-4Al-3Cu-2Fe+3vol% B_4C 1000 °C/90h perpendicular

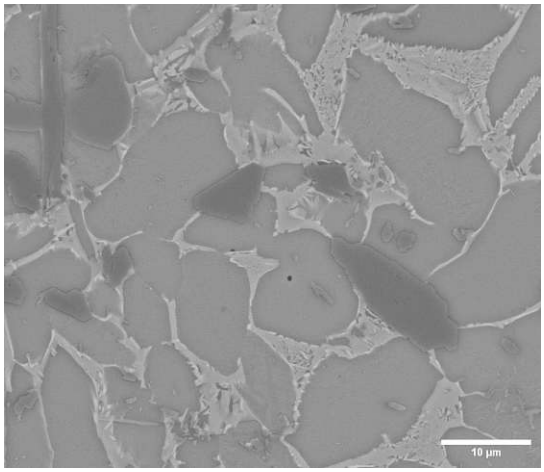

(f) Ti-4Al-3Cu-2Fe+3vol% B_4C 1000 °C/90h perpendicular

Figure 64: SEM images of the etched Ti-4Al-3Cu-2Fe+3vol% B_4C as-extruded samples (a-d), and the heat-treated samples (e-f)

4.1.9 Ti-10Al-1.4Nb-0.8Cr systems

The Ti-10Al-1.4Nb-0.8Cr alloy is based on a mixture of pre-alloyed Ti-34.5Al-4.8Nb-2.6Cr and titanium grade 2 powder. A pure elemental powder approach is to be discarded because of safety risks (Al-Fe). Hence, a pre-alloyed powder approach is performed. Theoretical CALPHAD calculations (FactStage) suggest the presence of Ti_3Al, which is expected to increase stiffness due to the higher intrinsic modulus. With up to 10 wt% a significant amount of Ti_3Al should be present. Figures 65 a-b and 66 a-d show the as-extruded sample. A two-phase lamellar α/β structure can be seen. In addition a texture is detected in the longitudinal direction. The heat treatment does not cause any significant difference, not even a coarsening (Figures 65 c-d and 66 e-f). No Ti_3Al can be seen in the optical and scanning electron microscope.

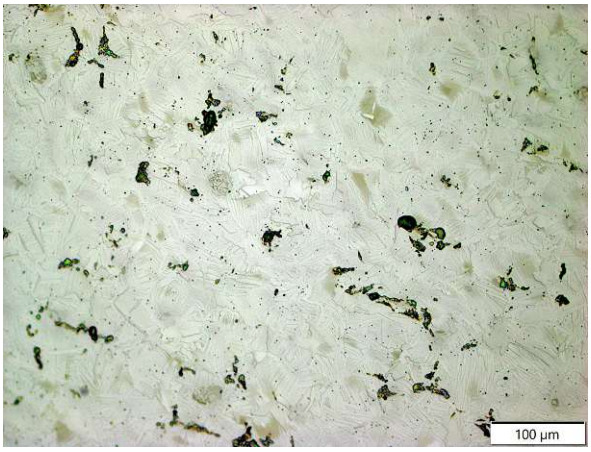

(a) Ti-10Al-1.4Nb-0.8Cr perpendicular

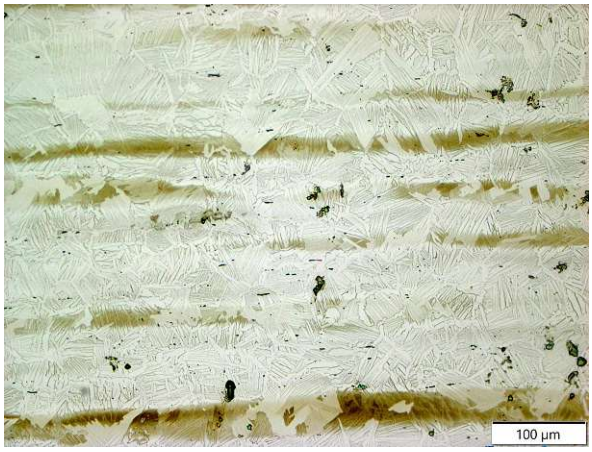

(b) Ti-10Al-1.4Nb-0.8Cr longitudinal

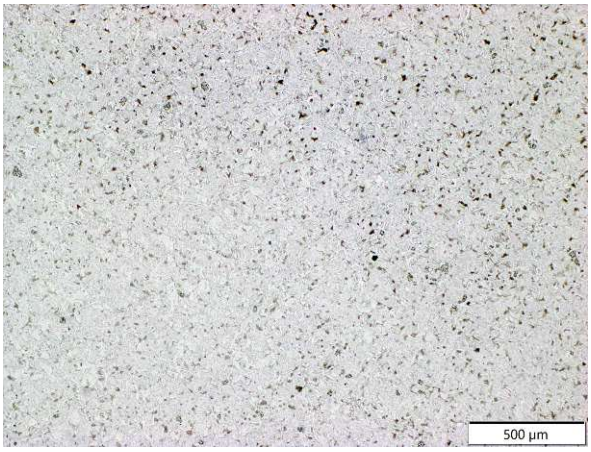

(c) Ti-10Al-1.4Nb-0.8Cr 1000 °C/90h perpendicular

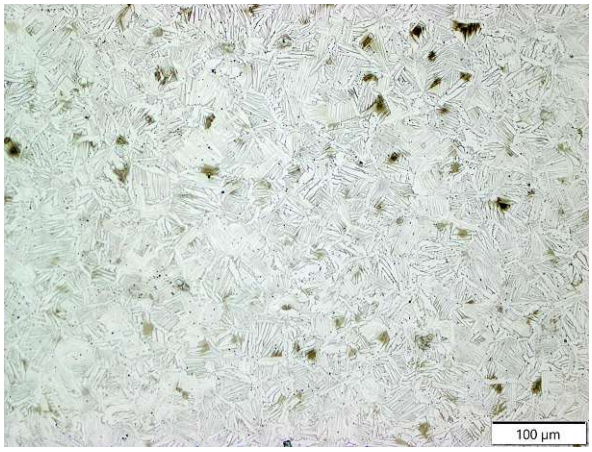

(d) Ti-10Al-1.4Nb-0.8Cr 1000 °C/90h perpendicular

Figure 65: Optical microscopy of the etched Ti-10Al-1.4Nb-0.8Cr as-extruded samples (a-b) and the heat-treated samples (c-d)

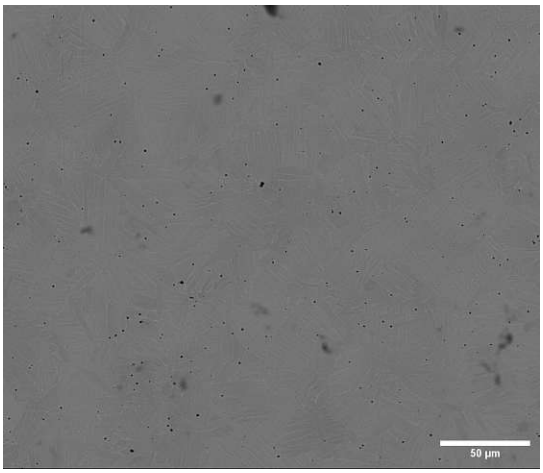

(a) Ti-10Al-1.4Nb-0.8Cr perpendicular

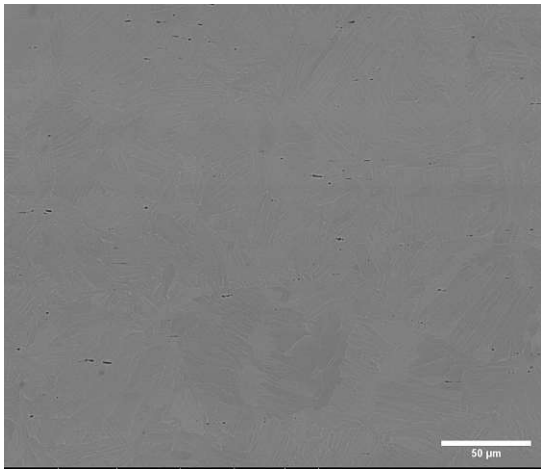

(b) Ti-10Al-1.4Nb-0.8Cr longitudinal

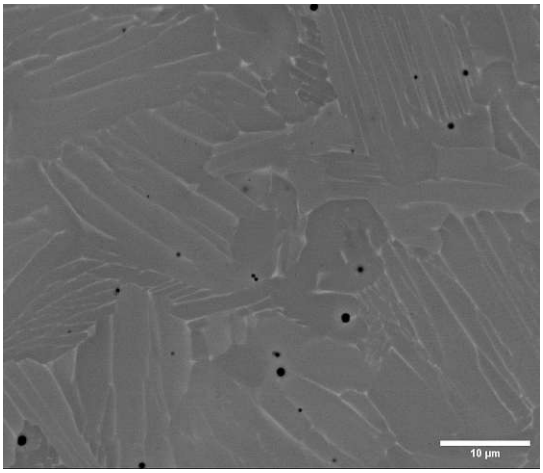

(c) Ti-10Al-1.4Nb-0.8Cr perpendicular

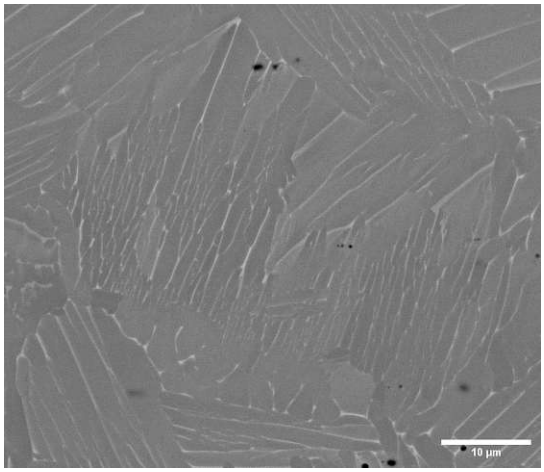

(d) Ti-10Al-1.4Nb-0.8Cr longitudinal

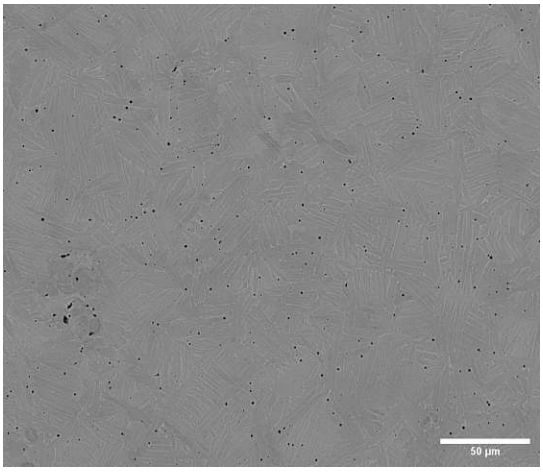

(e) Ti-10Al-1.4Nb-0.8Cr 1000 °C/90h perpendicular

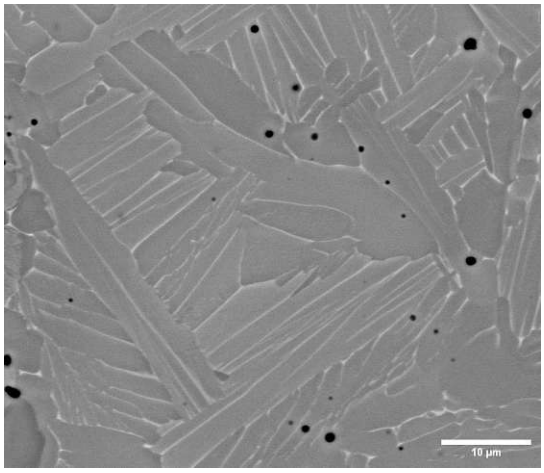

(f) Ti-10Al-1.4Nb-0.8Cr 1000 °C/90h perpendicular

Figure 66: SEM images of the etched Ti-10Al-1.4Nb-0.8Cr as-extruded samples (a-d), and the heat-treated samples (e-f)

4.2 Transmission Electron Microscopy

The goal of the electron diffractometry was to identify the formation of the ordered Ti_3Al phase after the heat treatment, as it cannot be analysed trough XRD (same crystal structure) and in the SEM. Figure 67 shows the diffraction pattern of Ti-8Al-1Mo-1V and Ti-10Al-1.4Nb-0.8Cr in the heat-treated state. Next to the main diffraction spots, satellite spots are visible , which confirm the presence of Ti_3Al as the satellites are in good agreement with the lattice constants.

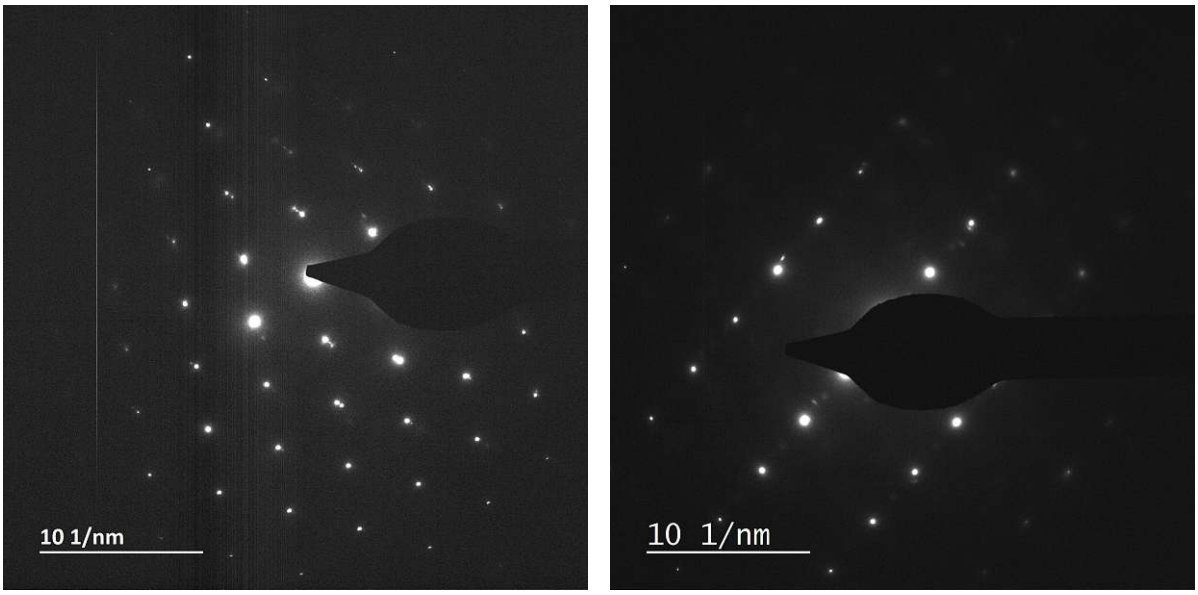

(a) Ti-8Al-1Mo-1V 1000 °C/90h (b) Ti-10Al-1.4Nb-0.8Cr 1000 °C/90h

Figure 67: Electron diffraction pattern of the heat-treated Ti-8Al-1Mo-1V and Ti-10Al-1.4Nb-0.8Cr sample

4.3 Hardness measurements

Table 8 shows the Vickers hardness (HV10) of all extruded systems. To evaluate any anisotropic effects, the hardness of the extruded bars is compared in both the vertical (p) and longitudinal (l) directions. In addition, the mean value in both directions is compared with the measurements of the heat-treated samples. For the pure Ti systems, no significant difference in hardness can be seen with respect to their orientation. The addition of ceramic particles leads to an increase in hardness as expected. A clear difference can be seen when finer boron carbide is added. As predicted by theory, the addition of more particles results in an even higher hardness. Unsurprisingly, the pure Ti sample shows no difference in hardness after heat treatment. However, all the particle reinforcements show a higher hardness after heat treatment. The case for boron carbide is clear as it transforms into titanium carbide and titanium boride, which have a similar hardness to titanium carbide but are precipitated in a very fine way.

The hardness of the Ti-6Al-4V alloys is in good agreement with hardness values around 320 HV10 reported in literature [47]. Adding ceramic particles leads to an increase in hardness. However, a difference in the orientation can be seen, particularly with the addition of boron carbide, which has a higher hardness in the perpendicular direction. Heat treatment has no effect on the pure alloy. However, both the addition of titanium carbide and boron carbide addition show a significant increase in hardness.

For the Ti-6.5Cu systems no anisotropy can be detected. Only the addition of boron carbide increases the hardness, while titanium carbide has no effect. Heat treatment results in a decrease for the alloy itself and with titanium carbide. This can be explained by the apparent coarsening of the grains. The boron carbide sample shows a slight increase in hardness which overcomes the effect of the coarser grains.

In the Ti-6.4Ni-2Fe system no hardness difference can be observed, except for the boron carbide sample, where again the perpendicular direction shows higher values. In the as-extruded state, both the powder-based alloy and the presintered alloy have the same hardness. This changes significantly after heat treatment. While there is an increase in hardness for the powder based alloy, there is a dramatic decrease for the pre-sintered alloy. The reason for this could be the different microstructure observed. Surprisingly, particle reinforcement does not lead to an increase in hardness. In fact, the hardness of the Ti-6.4Ni-2Fe+3vol% B_4C actually decreases significantly. Comparing the heat-treated microstructure of Ti-6.4Ni-2Fe and Ti-6.4Ni-2Fe+3vol% B_4C, a lack of α-phase can be seen in Ti-6.4Ni-2Fe+3vol% B_4C.

With the exception of isotropic hardness, a similar pattern can be seen for the Ti-6.4Ni-2Cr system. While there is an increase for the pure alloy, there is almost no change observed for the titanium carbide addition and a decrease in hardness for the boron carbide addition after the heat treatment. Again, the comparison of the microstructure shows a significant difference between the heat-treated Ti-6.4Ni-2Cr and Ti-6.4Ni-2Cr+3vol% B_4C.

The Ti-8Al-1Mo-1V system shows no anisotropic effects in the as-extruded state. Heat treatment results in an increase in hardness due to solid solubility of the residual molybdenum and

homogenisation. The addition of ceramic particles leads to an almost equal increase in hardness in both cases, as-extruded and annealed.

Of all the systems, Ti-5.7Al-5Co-3.8V has the highest hardness. The addition of particles has no influence on the hardness. After annealing, the pure alloy shows a significant increase in hardness due to the formation of α grain boundaries. A decrease is observed for the titanium carbide addition, which is surprising as they have a very similar microstructure. No change is observed for the boron carbide addition after annealing.

In the Ti-4Al-3Cu-2Fe system a slight anistropy can be seen for the as-extruded reinforced systems. Annealing leads to an increase in hardness due to solid solubility of the residual iron. While a decrease is observed for the titanium carbide addition, a significant increase is observed for the boron carbide addition.

The Ti-10Al-1.4Nb-0.8Cr alloy shows no anisotropy in the as-extruded state. The annealing results in an increase in hardness, as residual aluminium is solidly dissolved.

The observation, that especially the addition of titanium carbide leads to no hardness increase in some cases is surprising. One explanation might lay within the fact, that a relatively low indentation force was used, resulting in a area too small to actually represent the overall enhancement effect coming from the hard particles.

A graphically overview comparing the hardness regarding the direction is shown in Figure 69 as well as a comparison between the as-extruded and annealed state, which is shown in Figure 70.

In addition, the hardness measurements are used for the determination of the optimal annealing time. Two different heat treatments are carried out to ensure homogeneity and the effect on hardness. For both the holding temperature is 1000 °C but the holding time varies with 30 hours and 90 hours. Only selected samples are chosen for comparison. Figure 68 shows the measured hardness for different heat-treated conditions. An increase in hardness, respectively strength, can be seen with longer holding times. The heat treatment chosen for all systems is 1000 °C for 90 hours.

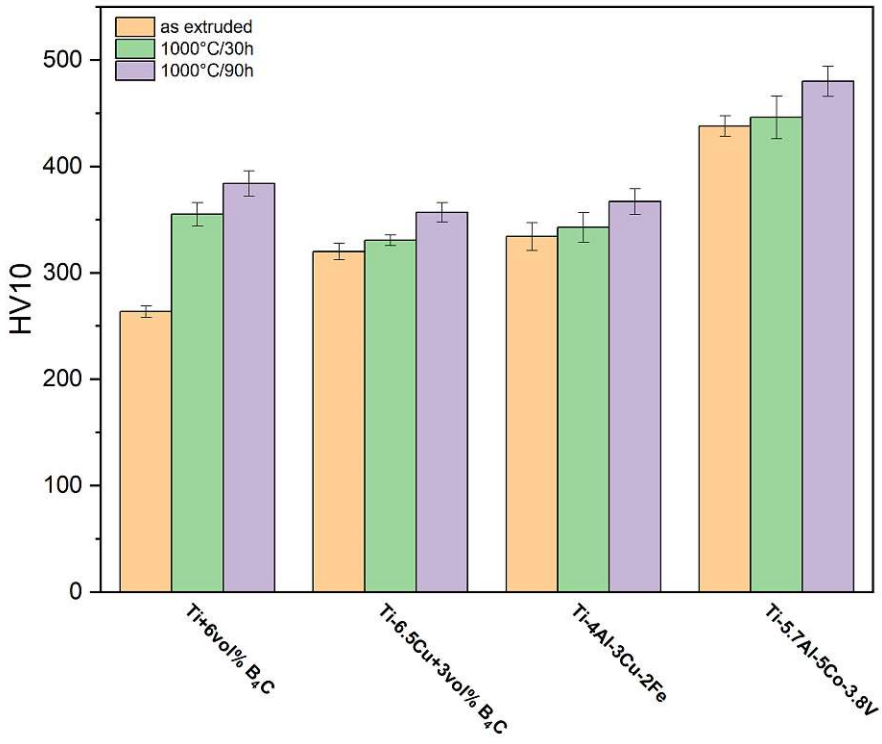

Figure 68: Comparision of the hardness with different time of annealing

Table 8: Vickers hardness measurements (HV10) of the as extruded samples in both, perpendicular (p) and longitudinal (l) direction and the heat-treated samples.

Matrix	Particles	Direction	HV10					
			as-extruded				1000 °C/90 h	
			Mean p/l	SD p/l	Mean	SD	Mean	SD
Ti	-	p	191	6	191	5	202	12
		l	192	4				
Ti	3vol% TiC	p	227	3	225	3	262	5
		l	223	2				
Ti	3vol% B_4C F2000	p	287	2	284	4	330	3
		l	280	2				
Ti	3vol%B_4C F500	p	215	3	217	7	294	4
		l	220	8				
Ti	6vol% B_4C F500	p	262	2	264	5	384	12
		l	265	7				
Ti-6Al-4V	-	p	310	5	313	6	320	5
		l	317	5				
Ti-6Al-4V	3vol% TiC	p	327	9	335	10	356	2
		l	342	4				
Ti-6Al-4V	3vol% B_4C	p	381	18	354	25	429	3
		l	336	2				
Ti-6.5Cu	-	p	307	8	299	12	268	8
		l	290	8				
Ti-6.5Cu	3vol% TiC	p	291	3	293	3	267	3
		l	295	2				
Ti-6.5Cu	3vol% B_4C	p	318	8	320	8	357	9
		l	322	7				
Ti-6.4Ni-2Fe	-	p	302	4	306	4	358	7
		l	309	2				
Ti-6.4Ni-2Fe	presintered	p	297	6	307	8	218	8
		l	303	9				
Ti-6.4Ni-2Fe	3vol% TiC	p	310	6	311	6	316	6
		l	311	7				
Ti-6.4Ni-2Fe	3vol% B_4C	p	326	10	328	10	274	6
		l	301	5				
Ti-6.4Ni-2Cr	-	p	291	5	295	6	358	10
		l	298	4				
Ti-6.4Ni-2Cr	3vol% TiC	p	295	4	296	4	317	10
		l	298	3				
Ti-6.4Ni-2Cr	3vol% B_4C	p	306	8	303	7	270	12
		l	301	5				
Ti-8Al-1Mo-1V	-	p	281	10	284	9	303	5
		l	287	6				
Ti-8Al-1Mo-1V	3vol% TiC	p	375	5	377	8	394	10
		l	280	10				
Ti-8Al-1Mo-1V	3vol% B_4C	p	369	7	367	9	394	10
		l	366	11				
Ti-5.7Al-5Co-3.8V	-	p	442	10	438	10	480	14
		l	434	8				
Ti-5.7Al-5Co-3.8V	3vol% TiC	p	429	3	441	16	401	13
		l	453	14				
Ti-5.7Al-5Co-3.8V	3vol% B_4C	p	436	3	442	7	446	13
		l	444	7				
Ti-4Al-3Cu-2Fe	-	p	343	10	334	13	367	12
		l	326	10				
Ti-4Al-3Cu-2Fe	3vol% TiC	p	329	6	339	16	327	6
		l	349	17				
Ti-4Al-3Cu-2Fe	3vol% B_4C	p	336	11	346	12	400	4
		l	355	2				
Ti-10Al-1.4Nb-0.8Cr	-	p	347	7	347	7	361	7
		l	346	7				

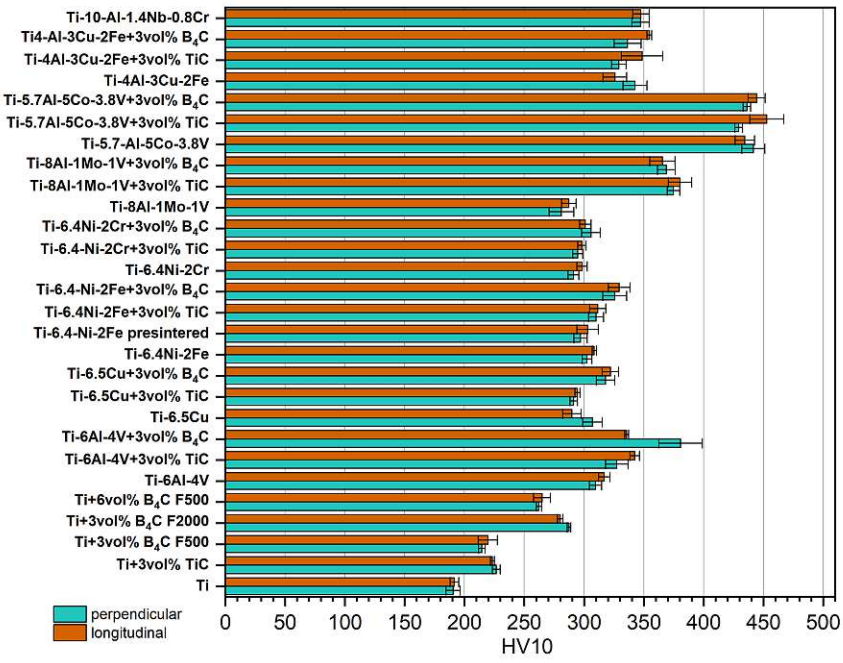

Figure 69: Vickers hardness of the as-extruded systems regarding their direction

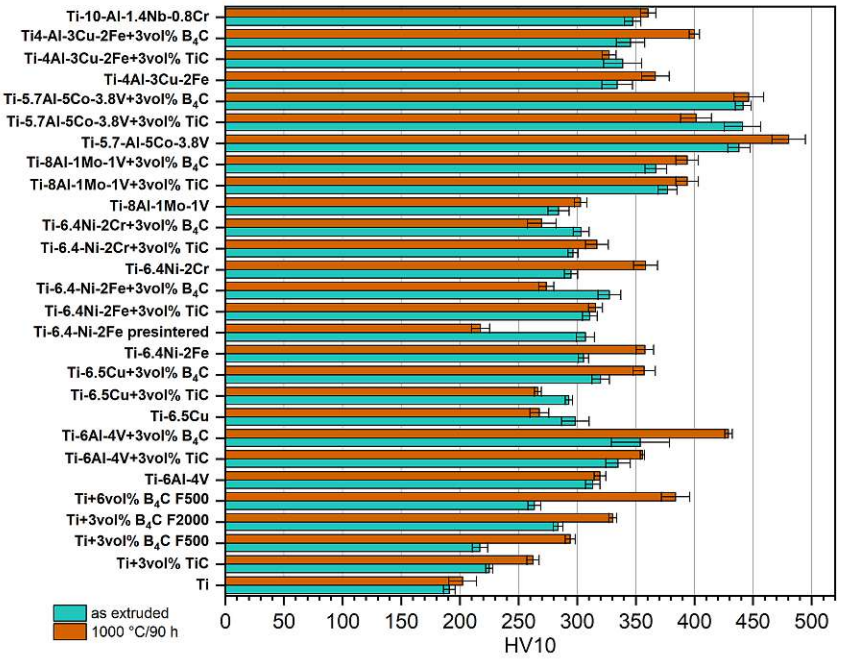

Figure 70: Vickers hardness of the as-extruded and heat-treated systems

4.4 Strength estimation

As a main objective is to find materials with a higher specific tensile strength than Ti-6Al-4V, the hardness is converted. The calculated tensile strengths are given in Table 9, and the densities from Table 10 are used to obtain the specific tensile strength. As hardness and strength are correlated, the discussion of hardness also applies to this section. The conversion is simply to compare the calculated strength with literature. Unsurprisingly, the as-extruded Ti systems are all below this specific value. As threshold the Ti-6Al-4V is choosen. Powder metallurgical production routes result in an strength regime of 900 to 1000 MPa which is in good agreement with both, the as-extruded and heat-treated Ti-6Al-4V alloy [48]. The addition of 3vol% B_4C F2000 and 6vol% B_4C F500 exceed the strength of the pure alloy. Except for the annealed Ti-6.5Cu+3vol% B_4C, no Ti-6.5Cu system reaches the specific strength of Ti-6Al-4V. The opposite is true for the Ti-6.4Ni systems, where only the annealed pure powder-extruded alloys exceed the value. For the Ti-8Al-1Mo-1V samples, only the reinforced ones show a higher specific strength. All the Ti-5.7Al-5Co-3.8V and Ti-4Al-3Cu-2Fe systems and the Ti-10Al-1.4Nb-0.8Cr alloy have a significantly higher specific strength. Figure 71 shows the calculated strength of all samples.

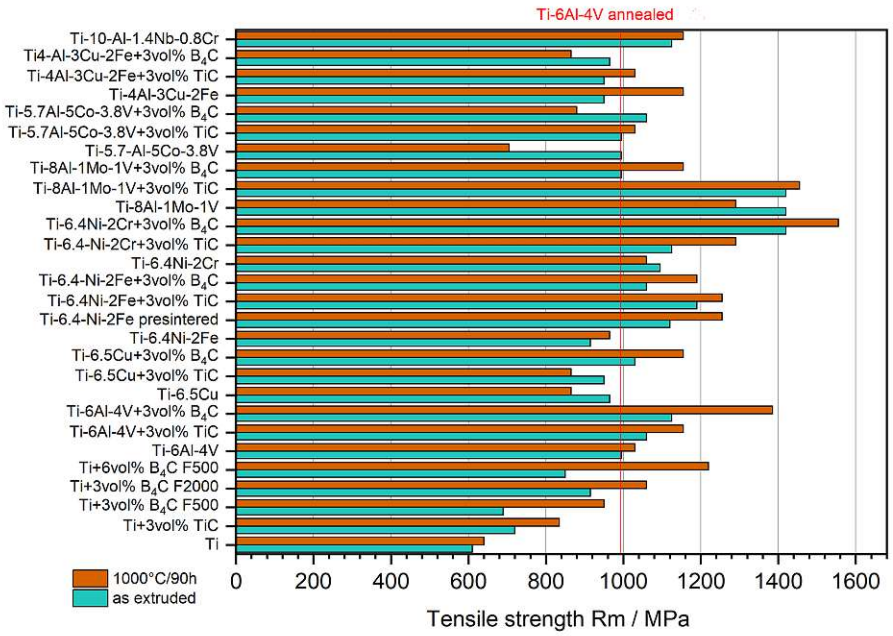

Figure 71: Calculated strength of all observed samples in the as-extruded and heat-treated state

Table 9: Calculated strength and specific strength of all observed samples in the as-extruded and heat-treated state

	strength / MPa		sp. strength / MPa/(g cm^3)	
	as-extruded	1000 °C/90 h	as-extruded	1000 °C/90 h
Ti	610	640	136	143
Ti+3vol% TiC	720	835	159	185
Ti+3vol% B_4C F500	690	950	155	210
Ti+3vol% B_4C F2000	915	1060	202	235
Ti+6vol%B_4C F500	850	1220	192	270
Ti-6Al-4V	995	1030	224	232
Ti-6Al-4V+3vol% TiC	1060	1155	242	263
Ti-6Al-4V+3vol% B_4C	1125	1385	257	314
Ti-6.5Cu	965	865	206	186
Ti-6.5Cu+3vol% TiC	950	865	204	186
Ti-6.5Cu+3vol% B_4C	1030	1155	223	249
Ti-8Al-1Mo-1V	915	965	210	222
Ti-8Al-1Mo-1V+3vol%TiC	1120	1255	255	287
Ti-8Al-1Mo-1V+3vol% B_4C	1190	1255	274	286
Ti-4Al-3Cu-2Fe	1060	1190	233	267
Ti-4Al-3Cu-2Fe+3vol%TiC	1095	1060	241	236
Ti-4Al-3Cu-2Fe+3vol% B_4C	1125	1290	251	285
Ti-5.7Al-5Co-3.8V	1420	1555	311	341
Ti-5.7Al-5Co-3.8V+3vol%TiC	1420	1290	310	282
Ti-5.7Al-5Co-3.8V+3vol% B_4C	1420	1455	315	318
Ti-6.4Ni-2Fe	995	1155	211	247
Ti-6.4Ni-2Fe presintered	995	705	212	150
Ti6.4Ni2Fe+3vol%TiC	995	1030	212	219
Ti-6.4Ni-2Fe+3vol% B_4C	1060	880	225	189
Ti-6.4Ni-2Cr	950	1155	202	245
Ti-6.4Ni-2Cr+3vol%TiC	950	1030	202	220
Ti-6.4Ni-2Cr+3vol% B_4C	965	865	207	185
Ti-10Al-1.4Nb-0.8Cr	1125	1155	258	268

4.5 Density

Looking at Table 10 one can see that the extrusion of alloys, even with particle additions, leads to dense materials. For all systems the density in regard of their theoretical density is higher than 99 %. For almost all samples with boron carbide addition the density increases after the annealing. This might be a result of the in-situ formed products titanium carbide and titanium boride, which have a higher density than the original boron carbide.

Table 10: Archimedes densities of all observed samples in the as-extruded and heat-treated state. Additionally, the obtained density is compared with the theoretical density.

Matrix	Particles	as-extruded			1000 °C/90 h			
		Density g cm^{-3}		% theoretical density	Density g cm^{-3}		% theoretical density	th. density
		Mean	SD		Mean	SD		
Ti	-	4.488	0.009	0.996	4.517	0.007	1.002	4.507
Ti	3vol% TiC	4.526	0.003	1.003	4.509	0.001	0.999	4.513
Ti	3vol% B_4C F2000	4.534	0.027	1.007	4.517	0.005	1.016	4.447
Ti	3vol% B_4C F500	4.445	0.013	1.000	4.518	0.002	1.016	4.447
Ti	6vol% B_4C F500	4.422	0.006	1.009	4.522	0.002	1.032	4.381
Ti-6Al-4V	-	4.432	0.002	1.003	4.442	0.014	1.005	4.420
Ti-6Al-4V	3vol% TiC	4.648	0.325	1.048	4.418	0.003	0.996	4.435
Ti-6Al-4V	B_4C F500	4.383	0.001	1.005	4.424	0.006	1.014	4.363
Ti-6.5Cu	-	4.683	0.004	1.007	4.667	0.009	1.004	4.650
Ti-6.5Cu	3vol% TiC	4.656	0.002	1.000	4.662	0.001	1.001	4.658
Ti-6.5Cu	3vol% B_4C F500	4.615	0.013	1.006	4.641	0.012	1.012	4.586
Ti-6.4Ni-2Fe	-	4.726	0.002	1.008	4.683	0.025	0.999	4.689
Ti-6.4Ni-2Fe	presintered	4.731	0.006	1.002	4.734	0.002	1.010	4.689
Ti-6.4Ni-2Fe	3vol% TiC	5.240	0.251	1.116	4.696	0.080	1.000	4.696
Ti-6.4Ni-2Fe	3vol% B_4C F500	4.713	0.005	1.019	4.698	0.001	1.016	4.696
Ti-6.4Ni-2Cr	-	4.689	0.015	1.001	4.707	0.197	1.006	4.683
Ti-6.4Ni-2Cr	3vol% TiC	4.691	0.015	1.000	4.656	0.019	0.993	4.690
Ti-6.4Ni-2Cr	3vol% B_4C F500	4.666	0.045	1.010	4.668	0.009	1.011	4.618
Ti-8Al-1Mo-1V	-	4.367	0.001	0.999	4.345	0.013	0.994	4.370
Ti-8Al-1Mo-1V	3vol% TiC	4.387	0.001	1.000	4.378	0.004	0.998	4.387
Ti-8Al-1Mo-1V	3vol% B_4C F500	4.336	0.002	1.005	4.385	0.001	1.016	4.314
Ti-5.7Al-5Co-3.8V	-	4.568	0.003	1.007	5.563	0.001	1.006	4.534
Ti-5.7Al-5Co-3.8V	3vol% TiC	4.575	0.005	1.006	4.570	0.003	1.005	4.546
Ti-5.7Al-5Co-3.8V	3vol% B_4C F500	4.508	0.003	1.008	4.571	0.001	1.022	4.473
Ti-4Al-3Cu-2Fe	-	4.540	0.003	1.011	4.458	0.003	0.993	4.449
Ti-4Al-3Cu-2Fe	3vol% TiC	4.514	0.004	1.003	4.497	0.003	1.000	4.499
Ti-4Al-3Cu-2Fe	3vol% B_4C F500	4.488	0.001	1.014	4.528	0.008	1.023	4.426
Ti-10Al-1.4Nb-0.8Cr	-	4.393	0.078	1.034	4.354	0.009	1.024	4.250

4.6 Young's Modulus

Table 11 shows the specific Young's modulus of all samples in the as-extruded and annealed state. Starting with the Ti systems, an increase in Young's modulus can only be seen for the boron carbide addition in the as-extruded state. Annealing does not lead to any significant change for the pure Ti sample, but a slight increase is observed for the titanium carbide addition. A strong increase is observed for all boron carbide additions, all of which have a specific modulus higher than 30 GPa/(g cm^{-3}). This is due to the formation of titanium boride, which has a higher Young's modulus.

In the Ti-6Al-4V system there is an increase with particle reinforcement. In addition, boron carbide has a greater effect than titanium carbide. After annealing, the alloy itself and the titanium carbide addition show no change as expected. However, the boron carbide addition results in a significantly higher stiffness up to 34.6 GPa/(g cm^{-3}). The same trends are visible for the Ti-6.5Cu systems where the boron carbide heat-treated sample reaches a stiffness of 33.2 GPa/(g cm^{-3}).

In the Ti-6.4Ni-2Fe system a difference between the powder route and the pre-sintered alloy can be seen. While the pre-sintered one has an initially higher stiffness, this changes with the annealing. The addition of particles results in a similar increase in the as-extruded state, whereas a pronounced enhancement can be seen for the boron carbide addition after annealing. The same result can be observed for the Ti-6.4Ni-2Cr system.

The pure Ti-8Al-1Mo-1V alloy shows one of the highest specific stiffness throughout all alloys. The as-extruded one has a specific stiffness of 28.1 GPa/(g cm^{-3}), which is increased after the heat treatment to 30.7 GPa/(g cm^{-3}). Particle reinforcement leads to a higher specific stiffness for both, titanium carbide and boron carbide. A significant increase can be observed for the titanium carbide addition resulting in a specific stiffness of 32.5 GPa/(g cm^{-3})

For the Ti-5.7Al-5Co-3.8V system, the addition of particles again leads to a higher stiffness, with the titanium carbide having a greater influence. Heat treatment gives a slight increase for the titanium carbide sample and a marked increase for the boron carbide sample, approaching the desired 30 GPa/(g cm^{-3}).

The Ti-4Al-3Cu-2Fe system also shows the highest stiffness with the titanium carbide addition reaching 30.2 GPa/(g cm^{-3}) in the as-extruded state. Annealing results in a slight increase for the titanium carbide sample and a higher increase for the boron carbide sample with 30.1 GPa/(g cm^{-3}).

Looking at the Ti-10Al-1.4Nb-0.8Cr alloy, there is no change at all. However, the specific stiffness is approximately the desired 30 GPa/(g cm^{-3}). Nevertheless, an increase in stiffness can be expected, taking into account possible particle reinforcement.

When comparing the pure alloys, one must take into consideration that the specific stiffness is dependent on the density. All alloys have an rather similar Young's modulus in the range of 115 to 125 GPa. By looking at the specific stiffness and considering density, differentiation is possible. For example Ti-6.5Cu and Ti-5.7Al-5Co-3.8V have a higher absolute stiffness than pure titanium but also a higher density resulting in no improvement in the specific stiffness. Ti-8Al-1Mo-1V has a higher absolute stiffness and a lower density than pure titanium, resulting in an overall higher specific stiffness. The heat treatment seems to have no impact on the stiffness except for the Ti-8Al-1Mo-1V alloy. Here an increase is observable, most likely due to the formation of Ti_3Al.

A consistent link between stiffness and hardness is not detectable. While an increase in the stiffness is observed for all particle reinforcements, this is not the case for the hardness. It is also not possible to identify whether a specific particle addition shows a negative, neutral or positive effect on the hardness as the values vary randomly. This may again be a result of a too small indentation area during the hardness measurement.

A graphical representation of the specific stiffness is shown in Figure 72.

Table 11: Specific Young's Modulus of all observed samples in the as-extruded and heat-treated state.

Matrix	Particles	sp. Young's modulus / GPa/(g cm^{-3})			
		as-extruded		1000 °C/90 h	
		Mean	SD	Mean	SD
Ti	-	26.0	0.1	25.6	1.1
Ti	3vol% TiC	26.0	0.1	26.5	0.0
Ti	3vol% B_4C F2000	29.7	0.0	32.9	0.2
Ti	3vol% B_4C F500	27.4	0.1	32.4	0.0
Ti	6vol% B_4C F500	29.3	0.2	33.8	0.2
Ti-6Al-4V	-	26.6	0.1	26.8	0.1
Ti-6Al-4V	3vol% TiC	27.6	0.1	27.7	0.8
Ti-6Al-4V	B_4C F500	28.3	0.2	34.6	0.8
Ti-6.5Cu	-	25.3	0.1	25.5	0.0
Ti-6.5Cu	3vol% TiC	26.1	0.2	26.3	0.2
Ti-6.5Cu	3vol% B_4C F500	27.0	0.1	33.2	1.1
Ti-6.4Ni-2Fe	-	24.2	0.1	26.9	0.3
Ti-6.4Ni-2Fe	presintered	25.4	0.5	25.4	0.3
Ti-6.4Ni-2Fe	3vol% TiC	26.6	0.7	26.3	0.3
Ti-6.4Ni-2Fe	3vol% B_4C F500	26.7	0.2	28.3	0.3
Ti-6.4Ni-2Cr	-	24.8	0.1	25.2	0.2
Ti-6.4Ni-2Cr	3vol% TiC	25.4	0.3	25.5	0.2
Ti-6.4Ni-2Cr	3vol% B_4C F500	27.1	0.5	28.1	0.8
Ti-8Al-1Mo-1V	-	28.1	0.3	30.7	0.2
Ti-8Al-1Mo-1V	3vol% TiC	32.5	0.4	33.0	0.4
Ti-8Al-1Mo-1V	3vol% B_4C F500	30.4	0.3	32.3	0.2
Ti-5.7Al-5Co-3.8V	-	25.4	0.0	25.9	0.3
Ti-5.7Al-5Co-3.8V	3vol% TiC	28.6	0.2	29.5	0.6
Ti-5.7Al-5Co-3.8V	3vol% B_4C F500	26.5	0.3	29.8	0.3
Ti-4Al-3Cu-2Fe	-	26.4	0.1	26.0	0.1
Ti-4Al-3Cu-2Fe	3vol% TiC	30.2	0.1	30.6	0.3
Ti-4Al-3Cu-2Fe	3vol% B_4C F500	28.4	0.2	30.1	0.0
Ti-10Al-1.4Nb-0.8Cr	-	30.3	0.5	29.7	0.4

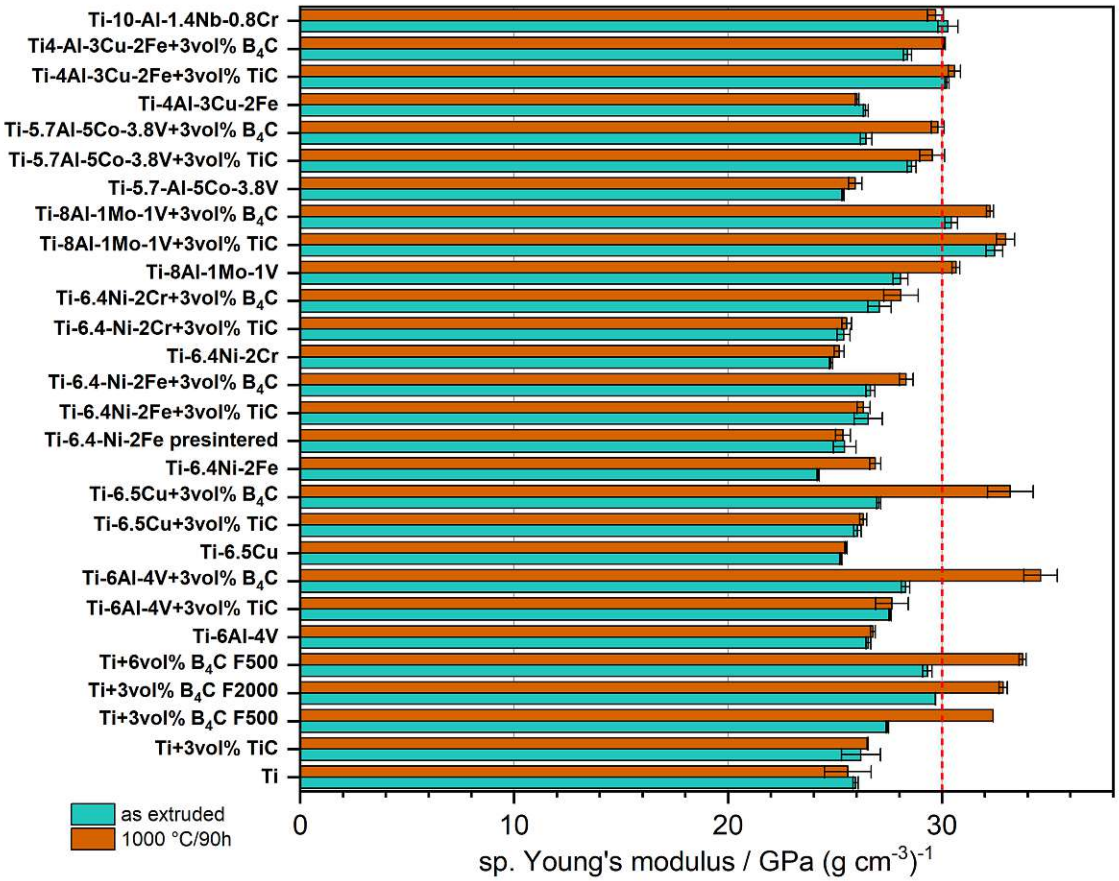

Figure 72: Specific Young's modulus

4.7 X-ray diffractometry

Figure 73 shows the diffraction pattern of the Ti systems in the as-extruded and heat-treated states. As expected, annealing results in no change for the Ti and Ti+3vol% TiC samples. However, for boron carbide a change can be seen due to the heat treatment. For better visualisation the region from 25 to 50° is shown in figure 74 with logarithmic intensity. For the Ti+3vol% B_4C F500 sample a disappearance of the shoulder around 38° can be seen after annealing. This means that the boron carbide reacts with the titanium matrix. This was observed in all samples with boron carbide addition. The boron carbide reacts to titanium carbide and titanium boride, which is detected through the appearance of new peaks at 29, 36, 41, 42, 46 and 48°. The finer boron carbide F2000 appears to react during the extrusion. The diffraction pattern of the Ti-6Al-4V system shown in figure 75 consists of a α-Ti and β-Ti peaks. The presence of titanium carbide is confirmed. Although boron carbide could not be clearly identified, due to the overlap with the α-Ti reflex, the pattern of titanium carbide and titanium boride are a certain indicator of its presence. The diffraction patterns of the Ti-6.5Cu systems in Figure 76 show a two phased metallic matrix consisting of α-Ti an Ti_2Cu. Again the ceramic particles are confirmed as well as the reaction of boron carbide. Looking at the patterns of the Ti-6.4Ni systems in Figure 77 and 78 one can see the presence of two metallic phases, α-Ti an Ti_2Ni. Next the diffractogram of the Ti-8Al-1Mo-1V system is shown in Figure 79. All of them display reflexes of α-Ti and β-Ti. In addition weak peaks that indicate the precence of Ti_3Al can be seen. In Figure 80 the pattern of the Ti-5.7Al-5Co-3.8V system are depicted. They show α/β-Ti peaks. The diffractograms of the Ti-4Al-3Cu-2Fe system is shown in Figure 81. Although three phases were predicted only two, namely α-Ti an Ti_2Cu and can be identified. The third, TiFe-phase may be to finely dispersed and to low in quantity to be detected. Last, the Ti-10Al-1.4Nb-0.8Cr alloy is shown in Figure 82. Here reflexes of α/β-Ti can be seen. In the as-extruded sample aluminium was detected, which disappeared after the annealing.

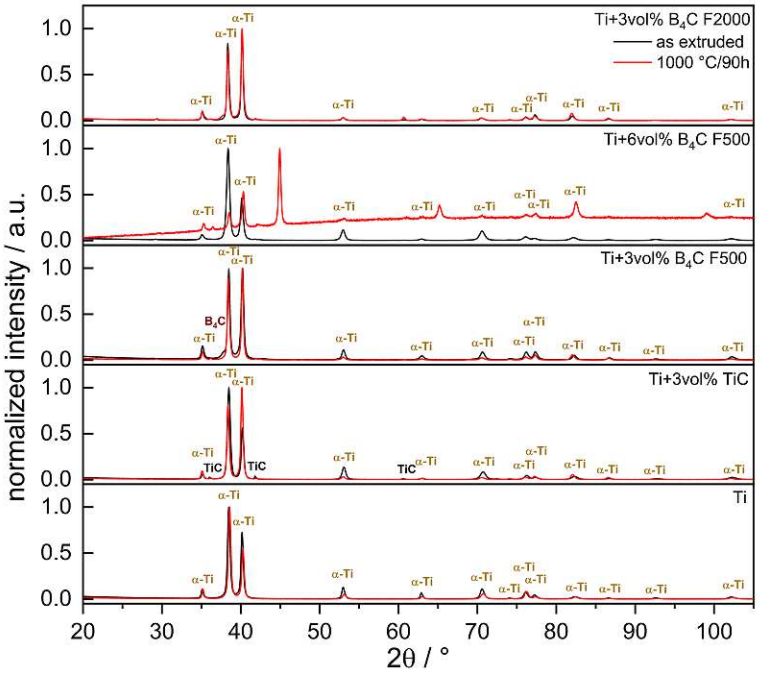

Figure 73: XRD measurement of the Ti-system

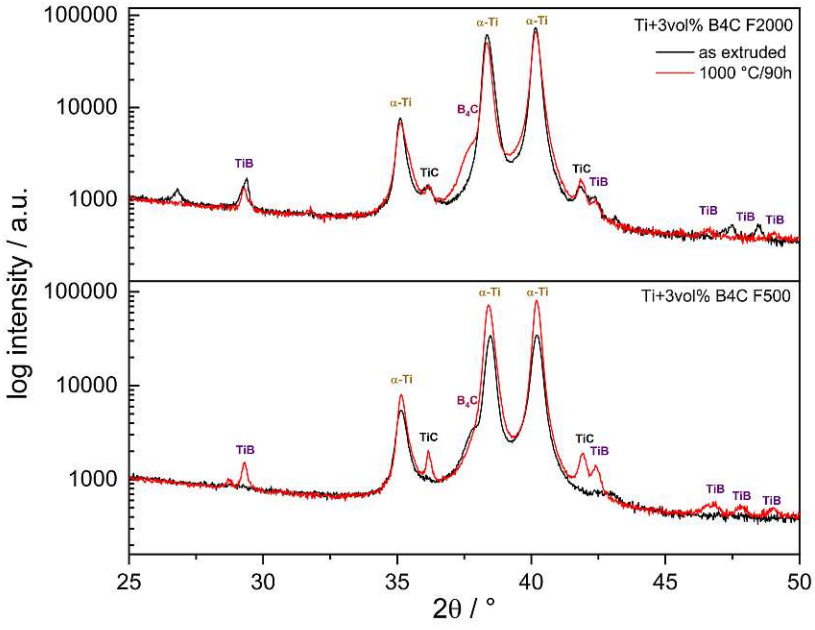

Figure 74: Logarithmic diffraction pattern of Ti+3vol% B_4C F500 and Ti+3vol% B_4C F2000

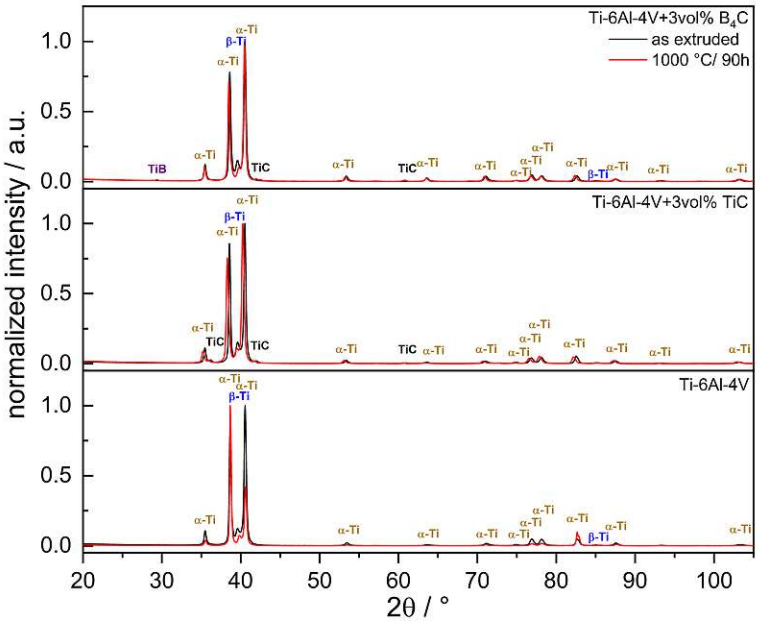

Figure 75: XRD measurement of the Ti-6Al-4V-system

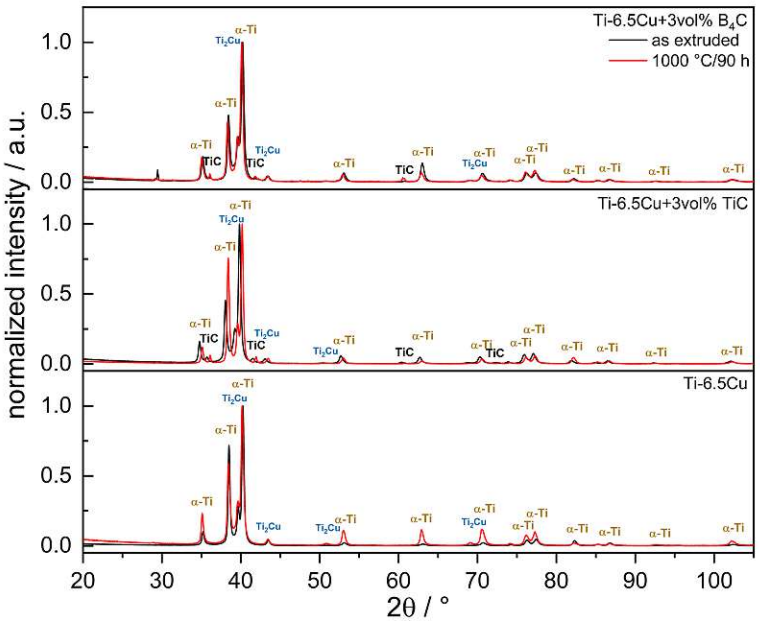

Figure 76: XRD measurement of the Ti-6.5Cu-system

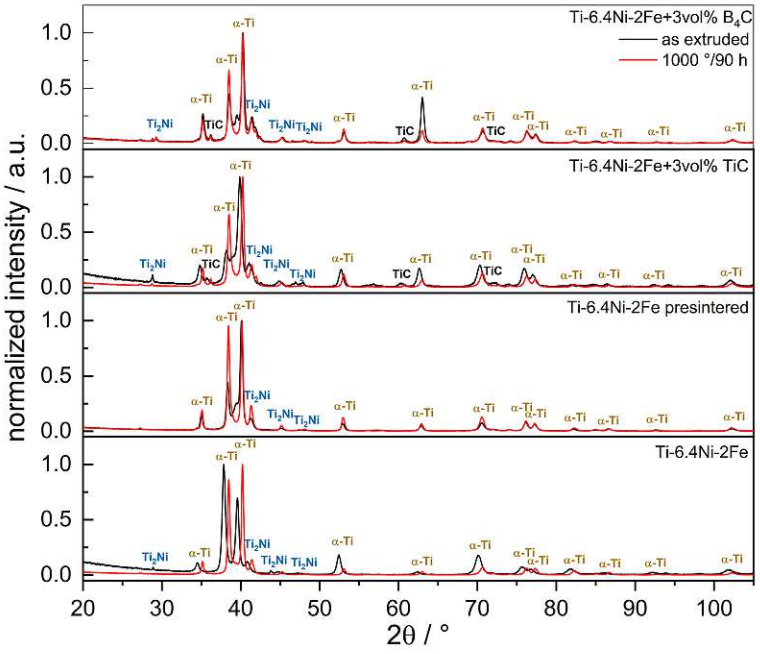

Figure 77: XRD measurement of the Ti-6.4Ni-2Fe-system

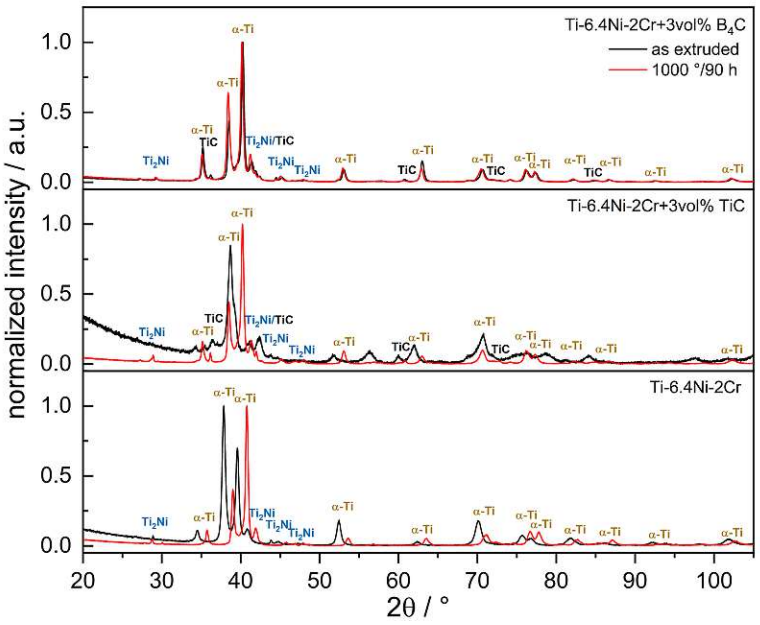

Figure 78: XRD measurement of the Ti-6.4Ni-2Cr-system

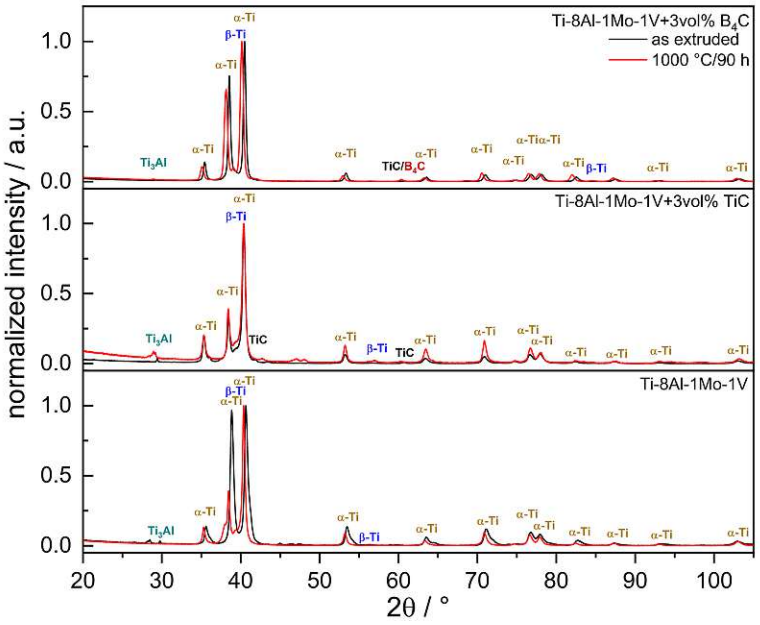

Figure 79: XRD measurement of the Ti-8Al-1Mo-1V-system

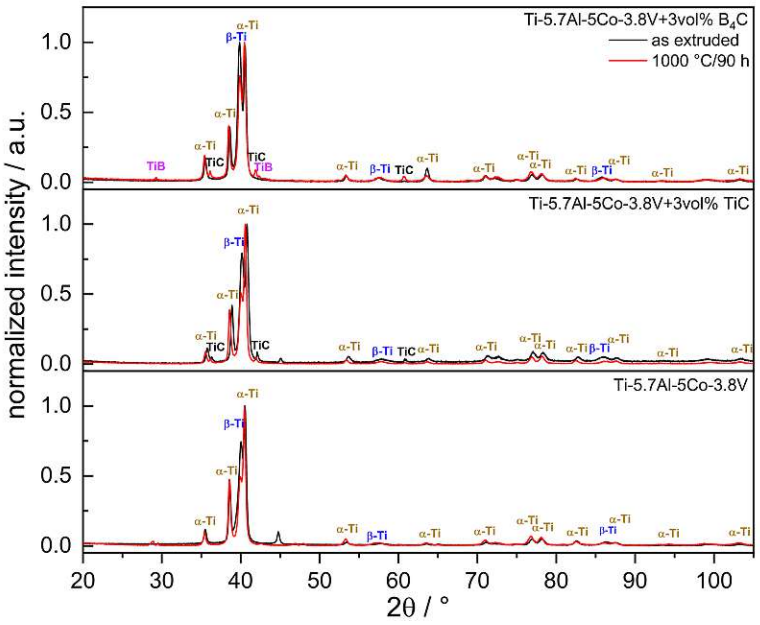

Figure 80: XRD measurement of the Ti-5.7Al-5Co-3.8V-system

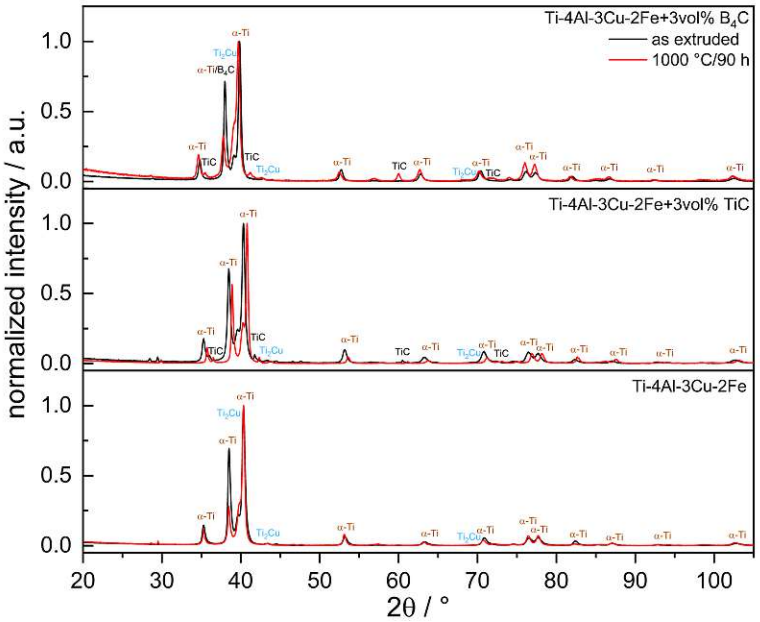

Figure 81: XRD measurement of the Ti-4Al-3Cu-2Fe-system

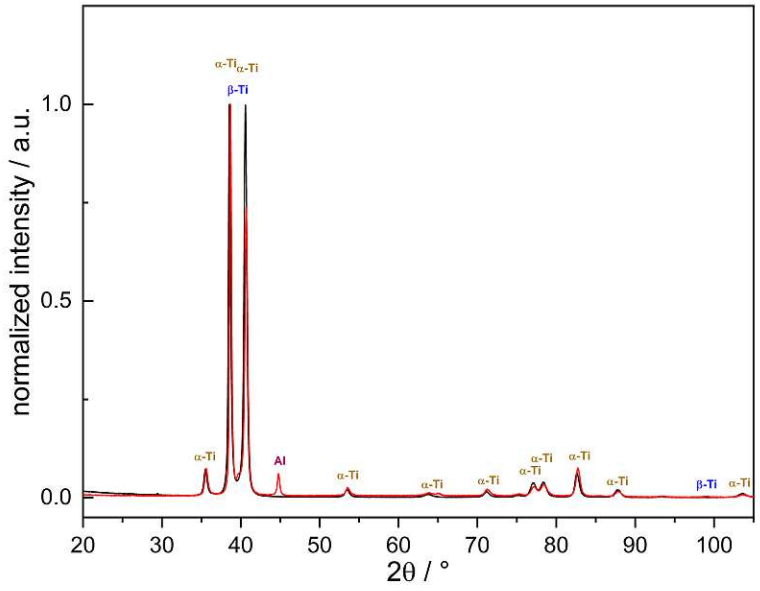

Figure 82: XRD measurement of the Ti-10Al-1.4Nb-0.8Cr-system

5 Conclusion

The experiments have shown that it is possible to produce alloys and MMCs by a pure powder based hot extrusion route. All extruded materials were dense, showed no pores in their microstructure and reached a limit of 99 % of the theoretical density. In terms of alloying, it has been demonstrated that not only pre-alloyed powders but also elementary powders can be used, offering a wide range of possibilities for future research. However, complex powder blends containing elements such as iron, chromium or molybdenum require subsequent heat treatment as the extruded material is inhomogeneous and these elements remain undissolved.

The characterisation of the materials was in agreement with theory in almost all systems. Not surprisingly, the Ti system is classified as pure α-alloy. As near α-alloys with the presence of Ti_3Al, an ordered structure ($D0_{19}$ type), the Ti-8Al-1Mo-1V and Ti-10Al-1.4Nb-0.8Cr systems can be classified. The Ti-6Al-4V and Ti-5.7Al-5Co-3.8V systems are binary α/β-alloys. Finally, the eutectic systems Ti-6.5Cu, Ti-4Al-3Cu-2Fe, Ti-6.4Ni-2Fe and Ti-6.4Ni-2Cr have been shown to have coexisting α and Ti_2Cu or Ti_2Ni phases. However, for the eutectic systems with iron, no TiFe phase was found by either SEM or XRD.

In general, it is shown that the addition of ceramic particles has a beneficial effect on the mechanical properties, increasing stiffness, strength and hardness. Furthermore, it is observed that the particles lead to a finer microstructure, which again benefits the mechanical properties. The exact mechanism behind the grain refining effect needs further investigations. However, in some systems, e.g. Ti-6.4Ni-2Fe and Ti-6.4Ni-2Cr, the addition of boron carbide combined with heat treatment results in a change in microstructure which significantly reduces hardness. In most cases there was no hardness anisotropy with respect to the extrusion direction. Although, in some cases the addition of particles results in a slightly higher hardness in the longitudinal direction. This is the case for Ti-6.5Cu+3vol% TiC, Ti-5.7Al-5Co-3.8V+3vol% TiC and Ti-4Al-3Cu-2Fe+3vol% B_4C. With regard to the reactivity of the ceramic particles, it can be seen that titanium carbide does not react with the matrix either during extrusion or after heat treatment. This is not the case for boron carbide. The finer boron carbide F2000 reacts during extrusion while the coarser F500 remains. Yet, after heat treatment, F500 also reacts to titanium carbide and titanium boride, as demonstrated by SEM and XRD.

Looking at the stiffness of the alloys, it can be seen that Ti-8Al-1Mo-1V and Ti-10Al-1.4Nb-0.8Cr have a higher specific stiffness than Ti-6Al-4V. For the Ti-8Al-1Mo-1V alloy a significant increase up to 30.7 $\mathrm{GPa/(g\,cm^{-3})}$ can be observed after heat treatment. This is explained by the formation of the Ti_3Al phase. No significant change is observed for the other alloys. The annealing of systems with titanium carbide addition does not lead to a change in stiffness, which is also consistent with the low reactivity of titanium carbide. On the other hand, annealed boron carbide shows a significant increase in stiffness due to the reaction of

these particles. The desired specific Young's modulus of 30 GPa/(g cm^{-3}) is achieved for the following systems:

- Ti+3vol% B_4C F2000 annealed 1000 °C
- Ti+3vol% B_4C F500 annealed 1000 °C
- Ti+6vol% B_4C F500 annealed 1000 °C
- Ti-6Al-4V+3vol% B_4C F500 annealed 1000 °C
- Ti-6.5Cu+3vol% B_4C F500 annealed 1000 °C
- Ti-8Al-1Mo-1V annealed 1000 °C
- Ti-8Al-1Mo-1V+3vol% TiC as-extruded and annealed 1000 °C
- Ti-8Al-1Mo-1V+3vol% B_4C F500 as-extruded and annealed 1000 °C
- Ti-4Al-3Cu-2Fe+3vol% TiC as-extruded and annealed 1000 °C
- Ti-4Al-3Cu-2Fe+3vol% B_4C annealed 1000 °C

Regarding the specific strength all Ti-5.7Al-5Co-3.8V, Ti-4Al-3Cu-2Fe and Ti-10Al-1.4Nb-0.8Cr systems exhibit a higher specific strength than Ti-6Al-4V. In the Ti-8Al-1Mo-1V system only the particle reinforced ones and annealed Ti-6.5Cu+3vol% B_4C reaches the requirement.

Taking this a step further, the ductility of a material must also be taken into account. Although a material may achieve certain properties, be it stiffness or strength, ductility is still required for processing into wire. In addition, the wire drawing machines would have to face excessive wear due to high stiffness and strength. These are major disadvantages for particle reinforced materials. Nevertheless, the unreinforced near α-alloys (Ti-8Al-1Mo-1V and Ti-10Al-1.4Nb-0.8Cr) show a great potential for this application. Of course, the Ti_3Al phase makes the alloys quite brittle, but controlled heat treatment followed by quenching will retain the ductile β-phase and suppress Ti_3Al formation. This more ductile alloy can then be used to make wire for additive manufacturing, which will then lead to a structural component. After annealing, this component may eventually achieve the desired properties. Overall, further research is needed to reach this point. In particular, in terms of mechanical properties, tensile tests and stiffness measurements are required, with a focus on anisotropy.

6 Appendix

Table 12: Conversion of hardness scales into tensile strength [40]

Strength / MPa	HV10	Strength / MPa	HV10
270	85	915	285
285	90	930	290
305	95	950	295
320	100	965	300
335	105	995	310
350	110	1030	320
370	115	1060	330
385	120	1095	340
400	125	1125	350
415	130	1155	360
430	135	1190	370
450	140	1220	380
465	145	1255	390
480	150	1290	400
495	155	1320	410
510	160	1350	420
530	165	1385	430
545	170	1420	440
560	175	1455	450
575	180	1485	460
595	185	1520	470
610	190	1555	480
625	195	1595	490
640	200	1630	500
660	205	1665	510
675	210	1700	520
690	215	1740	530
705	220	1775	540
720	225	1810	550
740	230	1845	560
755	235	1880	570
770	240	1920	580
785	245	1955	590
800	250	1995	600
820	255	2030	610
835	260	2070	620
850	265	2105	630
865	270	2145	640
880	275	2180	650
900	280		

Bibliography

[1] C. Leyens and M. Peters, *Titanium and Titanium Alloys*. WILEY-VCH Verlag GmbH and Co. KGaA, 2003.

[2] M. Mohammed, Z. Khan, and A. Siddiquee, "Beta titanium alloys: The lowest elastic modulus for biomedical applications: A review," *International Journal of Chemical, Nuclear, Metallurgical and Materials Engineering*, vol. 8, pp. 726–731, 2014.

[3] W. D. Brewer, R. Bird, and T. A. Wallace, "Titanium alloys and processing for high speed aircraft," *Materials Science and Engineering: A*, vol. 243, no. 1, pp. 299–304, 1998.

[4] S. Rawal, J. Brantley, and N. Karabudak, "Additive manufacturing of Ti-6Al-4V alloy components for spacecraft applications," *RAST 2013 - Proceedings of 6th International Conference on Recent Advances in Space Technologies*, pp. 5–11, 2013.

[5] A. Ho, H. Zhao, J. W. Fellowes, F. Martina, A. E. Davis, and P. B. Prangnell, "On the origin of microstructural banding in Ti-6Al-4V wire-arc based high deposition rate additive manufacturing," *Acta Materialia*, vol. 166, pp. 306–323, 2019.

[6] M. Peters, J. Kumpfert, C. H. Ward, and C. Leyens, "Titanium alloys for aerospace applications," *Advanced Engineering Materials*, vol. 5, pp. 419–427, 2003.

[7] T. M. T. Gofrey, P. S. Goodwin, and C. M. Ward-Close, "Titanium Particulate Metal Matrix Composites - Reinforcement, Production Methods, and Mechanical Properties," *Advanced Engineering Materials*, vol. 2, no. 3, pp. 85–91, 2000.

[8] H. S. Kim, S. I. Hong, and S. J. Kim, "On the rule of mixtures for predicting the mechanical properties of composites with homogeneously distributed soft and hard particles," *Journal of Materials Processing Technology*, vol. 112, pp. 109–113, 2001.

[9] R. F. S. Bernhard Ilschner, *Werkstoffwissenschaften und Fertigungstechnik*, 6th. Springer Vieweg Berlin, Heidelberg, 2016.

[10] H. Lu and D. Li, "Correlation between the electron work function of metals and their bulk moduli, thermal expansion and heat capacity via the Lennard-Jones potential," *Physica Status Solidi (b)*, vol. 251, 2014.

[11] K.-D. Arndt, H. Brüggemann, and J. Ihme, *Festigkeitslehre für Wirtschaftsingenieure : Kompaktwissen für den Bachelor*. Wiesbaden: Vieweg+Teubner Verlag / Springer Fachmedien Wiesbaden GmbH, Wiesbaden, 2011.

[12] W. Weißbach, *Werkstoffkunde : Strukturen, Eigenschaften, Prüfung*, 18. überarbeitete Auflage. Wiesbaden: Vieweg+Teubner Verlag, 2012.

[13] E. Doege and B.-A. Behrens, *Handbuch Umformtechnik : Grundlagen, Technologien, Maschinen* (VDI-Buch). Berlin, Heidelberg: Springer-Verlag Berlin Heidelberg, 2010.

[14] G. Gottstein, *Materialwissenschaft und Werkstofftechnik*, 4th ed. Springer Vieweg Berlin, 2014.

[15] E. Hornbogen and H. Warlimont, *Metalle: Struktur und Eigenschaften der Metalle und Legierungen*, 5. neu bearbeitete Auflage. Berlin, Heidelberg: Springer-Verlag Berlin Heidelberg, 2006.

[16] J. Rösler, M. Bäker, and H. Harders, *Mechanisches Verhalten der Werkstoffe*. Wiesbaden: B. G. Teubner Verlag / GWV Fachverlage GmbH, Wiesbaden, 2006, vol. 2.

[17] J. Dietrich, "Strangpressen," in *Praxis der Umformtechnik: Umform- und Zerteilverfahren, Werkzeuge, Maschinen*. Wiesbaden: Springer Fachmedien Wiesbaden, 2018, pp. 124–137.

[18] B. Liu *et al.*, "Microstructure and mechanical properties of equimolar FeCoCrNi high entropy alloy prepared via powder extrusion," *Intermetallics*, vol. 75, pp. 25–30, 2016.

[19] M. D. Hayat, H. Singh, Z. He, and P. Cao, "Titanium metal matrix composites: An overview," *Composites Part A: Applied Science and Manufacturing*, vol. 121, pp. 418–438, 2019.

[20] H. Tsang, C. Chao, and C. Ma, "Effects of volume fraction of reinforcement on tensile and creep properties of in-situ TiBTi MMC," *Scripta Materialia*, vol. 37, no. 9, pp. 1359–1365, 1997.

[21] Z. Xinghong, X. Qiang, H. Jiecai, and V. Kvanin, "Self-propagating high temperature combustion synthesis of TiB/Ti composites," *Materials Science and Engineering: A*, vol. 348, no. 1, pp. 41–46, 2003.

[22] S. Gorsse and D. Miracle, "Mechanical properties of Ti-6Al-4V/TiB composites with randomly oriented and aligned TiB reinforcements," *Acta Materialia*, vol. 51, no. 9, pp. 2427–2442, 2003.

[23] M. Lagos, I. Agote, G. Atxaga, O. Adarraga, and L. Pambaguian, "Fabrication and characterisation of titanium matrix composites obtained using a combination of self propagating high temperature synthesis and spark plasma sintering," *Materials Science and Engineering: A*, vol. 655, pp. 44–49, 2016.

[24] Y. Zhang, Z. Wei, L. Shi, and M. Xi, "Characterization of laser powder deposited Ti–TiC composites and functional gradient materials," *Journal of Materials Processing Technology*, vol. 206, no. 1, pp. 438–444, 2008.

[25] V. Anil Kumar, R. K. Gupta, M. J. N. V. Prasad, and S. V. S. Narayana Murty, "Recent advances in processing of titanium alloys and titanium aluminides for space applications: A review," *Journal of Materials Research*, vol. 36, no. 3, pp. 689–716, 2021.

[26] C. Liu, H. Wang, X. Tian, H. Tang, and D. Liu, "Microstructure and tensile properties of laser melting deposited Ti-5Al-5Mo-5V-1Cr-1Fe near beta titanium alloy," *Materials Science and Engineering: A*, vol. 586, pp. 323–329, 2013.

[27] H. Lee, G. Spanos, G. Shiflet, and H. Aaronson, "Mechanisms of the bainite (non-lamellar eutectoid) reaction and a fundamental distinction between the bainite and pearlite (lamellar eutectoid) reactions," *Acta Metallurgica*, vol. 36, no. 4, pp. 1129–1140, 1988.

[28] P. Narayana *et al.*, "Novel eutectoid Ti-5Ni alloy fabricated via direct energy deposition," *Scripta Materialia*, vol. 200, pp. 113–918, 2021.

[29] G. Choi, W. S. Choi, J. Han, and P.-P. Choi, "Additive manufacturing of titanium-base alloys with equiaxed microstructures using powder blends," *Additive Manufacturing*, vol. 36, 2020.

[30] P. Maria, Q. Dong, E. Mark, B. Simon, L. Qianchu, and D. Raj, "Additively manufactured pearlitic titanium-copper alloys: The effect of copper concentration on the microstructure and hardness," *20 th Australian International Aerospace Congress*, 2023.

[31] D. Ni, L. Geng, J. Zhang, and Z. Zheng, "Effect of B4C particle size on microstructure of in situ titanium matrix composites prepared by reactive processing of Ti–B4C system," *Scripta Materialia*, vol. 55, no. 5, pp. 429–432, 2006.

[32] R. Boyer, G. Welsch, and E. Collings, *Materials properties handbook: titanium alloys*. ASM International, 1994, vol. 1.

[33] F. Wu *et al.*, "Investigation on the electronic structures, elastic and thermodynamic properties of TiNi, Ti2Ni and TiNi3 intermetallic compound," *Materials Today Communications*, vol. 34, pp. 105–273, 2023.

[34] Y. Zhu, M. Yan, Y. Zhang, and C. Zhang, "First-principles investigation of structural, mechanical and electronic properties for Cu-Ti intermetallics," *Computational Materials Science*, vol. 123, pp. 70–78, 2016.

[35] A. Schlieter *et al.*, "Anisotropic mechanical behavior of ultrafine eutectic TiFe cast under non-equilibrium conditions," *Intermetallics*, vol. 19, no. 3, pp. 327–335, 2011.

[36] H. Liu, K. Tong, X. Feng, and B. Wen, "Temperature-dependent elastic and plastic properties of alpha2–Ti3Al," *Intermetallics*, vol. 139, pp. 107–368, 2021.

[37] G. W. Hollenberg and G. Walther, "The elastic modulus and fracture of boron carbide," *Journal of the American Ceramic Society*, vol. 63, no. 11-12, pp. 610–613, 1980.

[38] *Metallische Werkstoffe - Umwertung von Härtewerten (ISO 18265:2013)*, Norm, Nov. 2010.

[39] C. F. Hickey, "Tensile strength-hardness correlation for titanium alloys," Watertown Arsenal Laboratories, Tech. Rep. Wal Tr 405.22/1, Apr. 1961.

[40] SCHÜTZ & LICHT Prüftechnik GmbH, *Härtewerte und Zugfestigkeit - Umwertung von Härte–Skalen*, [Accessed on 25th of May 2023], 2023. [Online]. Available: `https://www.schuetz-licht.de/wissen-normen-seminare/umwertung-haerte-zugfestigkeit`.

[41] A. Zunghammer, *Entwicklung und Charakterisierung einer Ti-Legierung mit hoher spezfischer Steifigkeit und geringer Gefüge-Anisotropie*. Wien, 2022.

[42] M. Selvakumar, P. Chandrasekar, M. Mohanraj, B. Ravisankar, and J. Balaraju, "Role of powder metallurgical processing and TiB reinforcement on mechanical response of Ti-TiB composites," *Materials Letters*, vol. 144, pp. 58–61, 2015.

[43] C. Galli *et al.*, "Viability of Titanium-Titanium Boride composite as a biomaterial," *ISRN Biomaterials*, vol. 2013, 2013.

[44] K. Morsi and V. V. Patel, "Processing and properties of titanium-titanium boride (TiBw) matrix composites–a review," *Journal of Materials Science*, no. 6, pp. 2037–2047, 2007.

[45] T. Klein, M. J. Paul, C. Simson, J. Niedermayer, and B. Gludovatz, "Phase decomposition upon heat-treatment of a eutectoid Ti-Fe alloy processed by dual-wire-arc additive manufacturing," *Materials Letters*, vol. 319, pp. 132–305, 2022.

[46] M. Najafizadeh, D. Zhang, A. Maldar, M. Bozorg, and J. Liang, "Microstructure and mechanical properties of a high-strength Ti-4Al-2Fe-3Cu alloy fabricated by sintering and hot extrusion," *Metallurgical and Materials Transactions A*, vol. 53, pp. 1955–1968, 2022.

[47] P. Pinke, L. Caplovic, and T. Kovacs, "The influence of heat treatment on the microstructure of the casted Ti6Al4V titanium alloy," *Slovak University of Technology Bratislava. Web*, vol. 11, 2011.

[48] P. Kumar and K. R. Chandran, "Strength–ductility property maps of powder metallurgy (PM) Ti-6Al-4V alloy: A critical review of processing-structure-property relationships," *Metallurgical and Materials Transactions A*, vol. 48, pp. 2301–2319, 2017.

List of Figures

List of Tables

Eidesstattliche Erklärung

Hiermit erkläre ich, dass die vorliegende Arbeit gemäß dem Code of Conduct Regeln zur Sicherung guter wissenschaftlicher Praxis (in der aktuellen Fassung des jeweiligen Mitteilungsblattes der TU Wien), insbesondere ohne unzulässige Hilfe Dritter und ohne Benutzung anderer als der angegebenen Hilfsmittel, angefertigt wurde. Die aus anderen Quellen direkt oder indirekt übernommenen Daten und Konzepte sind unter Angabe der Quelle gekennzeichnet. Die Arbeit wurde bisher weder im In- noch im Ausland in gleicher oder in ähnlicher Form in anderen Prüfungsverfahren vorgelegt.

Vienna, 2023

Nico Moser